Numerical Investigation of Endwall/Casing Treatment Flow Phenomena

by

Andrew James Crook

B.S. Aerospace Engineering
University of Michigan (1987)

Submitted to the Department of Aeronautics and Astronautics in Partial Fulfillment of the
Requirements for the Degree of

Master of Science in Aeronautics and Astronautics

at the

Massachusetts Institute of Technology
August 1989

Signature of Author____________________________________
Department of Aeronautics and Astronautics
August 21, 1989

Certified by____________________________________
Professor E. M. Greitzer
Professor of Aeronautics and Astronautics
Thesis Supervisor

Approved by____________________________________
Professor Harold Y. Wachman
Chairman, Department Graduate Committee

Numerical Investigation of Endwall/Casing Treatment Flow Phenomena

by

Andrew James Crook

Submitted to the Department of Aeronautics and Astronautics
on August 21, 1989 in partial fulfillment of the
requirements or the Degree of Master of Science in
Aeronautics and Astronautics

Abstract

A detailed examination was carried out of the endwall flowfield of an isolated stator blade row using a computational fluid dynamics code. The goal of the investigation was to identify important endwall flow structures, determine the role these structure have in creating endwall stalling conditions, and to identify the effects hub treatment have in suppressing these near-stall conditions.

The three dimensional, viscous, turbulent, Reynolds averaged equations of motion were used to generate the flowfield for: 1) a blade row with clearance and a smooth moving hub, 2) a blade row with no clearance and a moving hub, and 3) a blade row with no clearance and a stationary hub. An inviscid form of the code was used to model a hub treatment configuration. The numerical solutions were compared to experimental data where possible, but the purpose was primarily to use the CFD as a tool for examining endwall and casing treatment fluid mechanics, rather than to validate extensively the code itself.

A corner stall occurred in the solution with no clearance and a stationary hub. Wall motion had little effect on the endwall flow and on the corner stall. The clearance flow and resulting vortex did remove the corner stall, but low momentum fluid was generated and collected into the vortex region. Much of the low total pressure fluid associated with the clearance vortex came from the blade tip and suction surface. It is suggested that the large blockage that results in endwall stall stems from this low total pressure region associated with the vortex.

Hub treatment was shown to replace the low total pressure region of the clearance/smooth wall solution with high total pressure fluid. Loss fluid in the blade tip region is either mixed with the high pressure jet, or drawn into the treatment. In addition, the streamwise circulation generated by the treatment jet acts to entrain high momentum fluid and bring it near the endwall region.

Thesis Supervisor: Dr. E. M. Greitzer
Title: Professor of Aeronautics and Astronautics

Acknowledgements

I wish to first express my thanks to Professor E. M. Greitzer. His insight, patience, and encouragement are greatly appreciated. Dr. C. S. Tan also deserves special thanks for his many contributions. His openness and commitment to instruction are very much admired.

I am grateful to G. T. Chen for the time he took to help me begin to understand the endwall flowfield. Gratitude is extended to Norman Lee for his insights into hub treatment phenomena. His heroic efforts in retrieving essential experimental data will not be forgotten. The help of Professor M. Giles and Mr. R. Haimes in some computational aspects of the project is also appreciated. Thanks are also extended to Arif Khalid for his work in helping complete this program.

This research would not be possible without the help of many people at the NASA Lewis Research Center. I am indebted to Dr. John Adamczyk whose energy and enthusiasm for problem solving was infectious. I would also like to thank Mark Celestina and Kevin Kirtley for their time spent in instructing me in the use of the computational code. I am grateful to Rick Mulac and Tim Beach for their aid in generating computational grids.

This work was supported by Allison Gas Turbine. Project monitor Dr. R. A. Delaney's suggestions and encouragement are appreciated.

Finally, I would like to express gratitude to my wife, Kathy, for her personal and prayerful support of me during this program. Without her sacrifice this work would not have been accomplished.

Table of Contents

Chapter 1 Introduction

Chapter 2 Computational Procedure

Chapter 3 Comparison of Numerical Solutions to Experiments

Chapter 4 Analysis of Numerical Solutions

Chapter 5 Summary, Conclusions and Recommendations

Nomenclature

a	Speed of sound
A	Cell face area
C	Axial chord length
CX	Average inlet axial velocity
C^-	Interior Riemann invariant
C^+	Exterior Riemann invariant
D	Artificial dissipation operator
e	Total energy
H	Total enthalpy
i	Axial cell index
j	Radial cell index
k	Tangential cell index
M	Meridional Mach number
p	Static pressure
P	Total pressure
Q	Dynamic pressure ($\rho\|\vec{u}\|^2/2$)
r	Radius (radial direction)
t	Time
u	Axial velocity
$\mathbf{U}$	State variable vector
$\vec{u}$	Velocity vector
v	Radial velocity
V	Cell volume
w	Tangential velocity
z	Axial direction
α	Runge-Kutta integration constant
β	Flow angle leaving treatment grooves
γ	Ratio of specific heats
ε	Artificial dissipation coefficient
κ	Artificial dissipation constant
μ	Viscosity
ν	Pressure gradient operator
ω	Vorticity
Ω	Machine rotational speed
ρ	Density
θ	Tangential direction
τ	Shear stress

Subscripts

h	Hub
in	Average at inlet
l	Molecular
m	Average at midspan
o	Reference ambient
s	Streamwise
t	Turbulent
T	Total
v	Viscous

Superscripts

n	Time step
(2)	Second difference
(4)	Fourth difference

Chapter 1
Introduction

1.1 Introduction

It has been known for some time that casing "treatment" (grooves or slots) applied over rotor blade tips can improve surge margin in axial compressors. Many configurations of treatment have been developed [1-3], most of which have associated with them an efficiency penalty. While the potential for performance improvement of casing treatment is well known, a complete explanation of the stall suppressing mechanism of the treatment has not yet been established.

The fluid mechanics of casing treatment is actually only one of the interesting and yet unresolved problems associated with endwall flow. For example, it has been shown that casing treatment works only when the turbomachine performance limiter is stall associated with the endwall region. However endwall stall, even for the smooth wall situation, still can not be predicted. Therefore to understand the mechanism of casing treatment, one must also understand the more general endwall flow problem.

For unshrouded rotors or cantilevered stators, the clearance flow and its effects dominate much of the endwall region. Part of this investigation therefore, centers on a study of clearance flow effects.

Over the last twenty years, a large amount of research on turbomachinery casing treatment and endwall flows has been published. To give some of the observations and conclusions of the present study proper perspective, a brief review will be presented. The review is made up of two sections. The larger one covering casing treatment research and the other (much shorter section) introduces some aspects of clearance flow research relevant to this study. Finally, the approach and objectives of this study are presented.

The approach taken is to examine endwall flows and casing treatment operation with a computational fluid mechanics (CFD) code. An outline of the numerical procedure used is the subject of Chapter two. The solutions are compared to existing experimental data to determine, at least on an overall basis, how well the numerical procedure models the flow. This comparison is the subject of Chapter three. Finally, the computational solutions are investigated in detail in Chapter four. Chapter five highlights the conclusions of the investigation and gives recommendations as to future work on the subject.

1.2 Casing Treatment Research

The earliest studies involving casing treatment were on fans operating in the transonic flow regime. In this work, which had the goal of obtaining improved stall margin, a number of the casing treatment configurations were generated [1-2]. Since then more fundamental research has been carried out to try to understand mechanisms by which the treatments prevent rotating stall. While this review is not intended to be exhaustive, it gives a framework of some pertinent discoveries and analyses.

Prince, Wisler, and Hilvers [1] studied several configurations of casing treatment upon a low speed rotor. Circumferential grooves, axial skewed slots, and blade angle slots all demonstrated stall margin improvement. Data taken at the rotor exit showed higher relative total pressure at locations near the casing with the tip treatments installed. Both analytical models and yarn tuft observations in the treatment grooves showed radial movement of fluid. Of particular note was the radial movement out of the upstream region of the treatment area.

Takata and Tsukuda [2] studied various casing treatments upon a low speed rotor as well. Velocity and pressure measurements were taken in the treatment slots and at the exit plane of the rotor. They also found a strong radial flow or jet coming out of the upstream sections of the treatment area. An experiment was run with hub treatment applied under a stator to examine the effect of the jet on the passage fluid. The conclusion inferred from the experiment is that the total amount of tangential momentum introduced by the jet is quite important to casing treatment effectiveness.

Greitzer et. al. [3] conducted an experimental study on the effectiveness of casing treatment upon stalling rotor passages. Two rotor configurations were tested. One configuration exhibited stall originating on the blade surface while the other configuration stalled in the endwall. The casing treatment improved the stall margin for the rotor with end wall stall, while no significant improvement was found for the rotor with blade surface stall. It was thus concluded that casing treatment effectiveness was linked to endwall stall suppression. Further, experimental evidence to support this was seen in data showing that casing treatment removed an area of low relative total pressure near the endwall of the rotor configuration that displayed end wall stall.

Smith [4] conducted an experimental study in which detailed data was taken in the passage, the treatment grooves, and the exit plane of a rotor with axially skewed groove casing treatment. He also found that a region of high blockage/low relative total pressure fluid in the endwall of the smooth wall configuration (prior to stall) was removed when casing treatment was in effect. From the passage and treatment groove velocity data, Smith described two fluid mechanical effects of the treatment. High loss fluid in the endwall near the trailing edge was being drawn into the casing treatment, and high relative total pressure fluid was introduced into the passage from the treatment near the leading edge of the blades. The unsteady effects of the treatment were small so it was concluded that the unsteadiness was of minor importance to the treatment operation.

1.2.1 Previous Gas Turbine Lab Casing Treatment Research

Since the present work is an extension of the casing/hub treatment research that has been going on at the Gas Turbine Lab (GTL) at M.I.T., it is useful to separate that previous work from the general review.

Cheng, Prell et. al. [5] conducted a set of experiments to study the effect of hub treatment applied underneath a stator blade row using a single stage compressor. A schematic of the research rig is shown in Figure 1.1, and Figure 1.2 shows some detail of the hub treatment. Table 1.1 displays pertinent data on the flow path and the blade geometry. Two blade configurations were tested, one with low stagger and one with higher stagger to change the stall mode from blade stall to wall stall. The treatment improved the static pressure rise performance of the wall stalling configuration and Table 1.1 outlines this configuration. From the data, it was seen that the effect of the hub treatment was to remove a region of high loss fluid near the hub. Total pressures at the exit of the stator were higher than those at the exit with a smooth wall at the hub.

Johnson [6] carried out detailed velocity measurements in the end wall region for both the smooth wall and hub treatment configurations. The velocity data indicated a region of blockage in the rear of the passage near the hub which was removed by the casing treatment. From the data it was inferred that the flow removal in the rear of the passage was the key feature of the treatment in removing blockage and suppressing end wall stall. The jet in the front part of the passage was thought to be of little importance in relieving end wall blockage, but was the major source of efficiency penalty.

Lee [7] undertook the task of isolating the two fluid mechanical effects of the hub treatment (i.e., the fluid removal and the fluid jet) in a diagnostic manner. He generated several hub treatment configurations shown in Figure 1.3, which were open at the bottom to a plenum below the hub. A specified amount of flow could be removed or injected through these hub configurations. Flow could thus be removed or injected at various locations along the hub to see what the effect of jet or suction by itself had on the blade row performance. It was found that both injection and removal increased the stall margin of the blade row, but neither was as effective as the full hub treatment. In addition a strong correlation was found between blade row performance increase and streamwise momentum injected into the flow.

1.3 Clearance Flow Research

It is well known that tip clearance degrades compressor performance and the endwall region is generally critical in predicting compression system performance limits (see [8]). It is also clear that the endwall flowfield is not well understood.

There has been a large amount of research published in the last 30 years on tip clearance flows. Much of the analyses can be lumped into two main types. The first type might be called tip leakage models. In these models, the clearance flow is thought of as a jet driven by the local static pressure difference across the blade. The loss associated with the clearance flow is regarded as the complete loss of kinetic energy in the jet [9-10]. Another line of analyses is based on a lifting line approach to calculate the secondary flow losses and the induced drag associated with the clearance vortex [11].

There are several reviews of clearance flow research, for example [12-13], and that task will not be undertaken here. Research pertinent to the present endwall study (e.g., [14-15]) will be mentioned as it related to the analysis in later chapters.

1.4 Present Approach and Objectives

From Lee's results, it is clear that there is no single aspect of casing treatment which is "the key" to its stall suppressing capabilities. However, certain aspects of treatment properties (e.g., streamwise momentum) were identified as important. To determine the role of momentum injection and other critical properties of tip treatment in suppressing endwall stall, a greater understanding of the endwall flowfield is needed. Computational fluid dynamics is seen as a tool to aid in understanding this region.

Computational fluid dynamics codes are now capable of capturing much of the physics of complex, three dimensional flows [16-18]. With a reliable numerical solution, one can thus carry out a "numerical experiment" in which the flowfield can be examined in detail. Geometry and boundary conditions can be changed and controlled easily to aid in seeing parametric trends. Through an investigation of the numerical solutions, which resolve the flowfield in great detail, a better understanding of the flow features can be found.

The objectives of the investigation are listed below. They are:

1) To identify the major flow features of the end wall region.
2) To determine the effects of clearance flow on the endwall flowfield structure.
3) To identify possible stalling conditions in the endwall region and their causes.
4) To isolate the important flow structures of hub treatment.
5) To identify the stall inhibiting features of hub treatment.

In addition, a prerequisite for accomplishing these objectives is the evaluation of the reliability of the numerical solutions.

Chapter 2
Computational Procedure

2.1 Introduction

The computational codes (both viscous and inviscid) used in the endwall and hub treatment flow investigation were developed by J. Adamczyk and associates at the NASA Lewis Research Center. The scheme is based upon a finite volume-time marching procedure originally developed by Jameson [19]. An outline of the procedure follows this introduction.

The inviscid procedure [20] was found to be reliable and robust. The code was also easily adaptable to the various inlet and boundary conditions required. To model the hub treatment, a special boundary condition was needed. This adaptation of the inviscid code is outlined in section 2.3.

A code that solves the Reynolds averaged Navier Stokes equations has also been developed. The numerical scheme is a modification of the original inviscid procedure and is covered in some detail in [21]. The endwall flowfield without hub treatment is studied primarily in solutions using this "viscous" code. An outline of the modification of the code for viscous effects is the subject of section 2.4. In the last sections of this chapter, the computational grids and the convergence histories of the solutions are presented.

2.2 Inviscid Flow Solution Scheme

Governing Equations/Discretization

The basic equations used are those that govern the steady inviscid fluid flow in three dimensions. These equations, representing the Euler equations in cylindrical coordinates, are shown in conservative form in equation (3) below. Expressions (1) and (2) show the velocity and the state variable vectors, respectively.

$$\vec{u} = u\,\hat{e}_z + v\,\hat{e}_r + w\,\hat{e}_\theta \tag{1}$$

$$\mathbf{U} = (\,\rho,\ \rho u,\ \rho v,\ \rho w,\ \rho e\,) \tag{2}$$

$$\frac{\partial}{\partial t}\int_V \mathbf{U}\ dV + L(\mathbf{U}) = 0 \tag{3}$$

For purposes of brevity, exposition of the terms of the L operator are deferred to Appendix B. These equations balance mass flow, axial, radial, and angular momentum, as well as energy for a control volume. The equation of state relating the pressure to total internal energy is shown below.

$$e = -\frac{1}{(\gamma - 1)}\frac{p}{\rho} + \frac{1}{2}\left(\vec{u}\cdot\vec{u}\right) \tag{4}$$

Equations (3) and (4) form a system of six equations for the pressure and the five flow variables shown in (2). For a typical cell volume, shown below, the equations are discretized in space to form a system of ordinary differential equations.

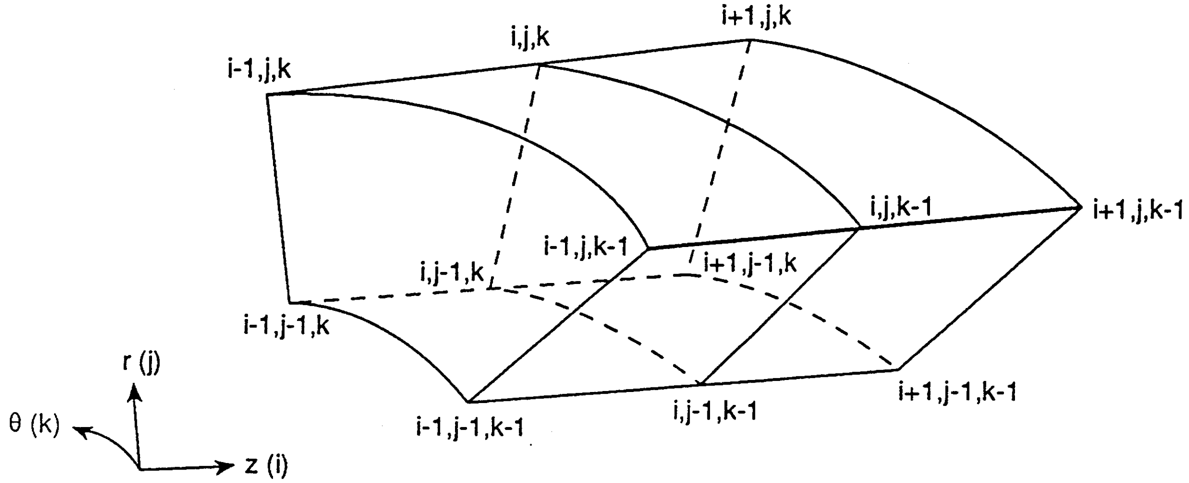

The flow variables associated with each cell are taken to be the average values for that cell. Since the variables are calculated for the center of the cell, the values needed at the control volume surface are taken as the average of that variable for the two neighboring cells. This scheme is equivalent to a central difference scheme and, for a smooth uniform mesh, is second order accurate in space.

All velocities in the equations are nondimensionalized by the reference speed of sound over the ratio of specific heats (gamma). The density and pressure are normalized by their reference values. The lengths in the equations, and in the computational grid geometry, are nondimensionalized by the diameter of the hub.

Artificial Dissipation

The discretized system of equations has unstable properties and can exhibit odd-even point decoupling. To suppress these instabilities, artificial dissipation terms are added to the equations. Jameson found that a dissipative system combining second and fourth difference smoothing operators was effective. The difference operator for the axial direction is shown below.

$$D_z(U) = d_{i+1/2,j,k} - d_{i-1/2,j,k} \tag{5}$$

$$d_{i+1/2,j,k} = \frac{V_{i+1/2,j,k}}{\Delta t_{i+1/2,j,k}} \left[\varepsilon^{(2)}_{i+1/2,j,k} \Delta_z U_{i+1/2,j,k} - \varepsilon^{(4)}_{i+1/2,j,k} \Delta^3_z U_{i+1/2,j,k} \right] \tag{6}$$

$$\varepsilon^{(2)}_{1+1/2,j,k} = \kappa^{(2)} \max(\nu_{i+1,j,k} , \nu_{i,j,k}) \tag{7}$$

$$\varepsilon^{(4)}_{1+1/2,j,k} = \max(0 , \kappa^{(4)}_{1+1/2,j,k} - \varepsilon^{(2)}_{1+1/2,j,k}) \tag{8}$$

$$\nu_{i,j,k} = \left| \frac{p_{i+1,j,k} - 2p_{i,j,k} + p_{i-1,j,k}}{p_{i+1,j,k} + 2p_{i,j,k} + p_{i-1,j,k}} \right| \tag{9}$$

$$\kappa^{(2)} = 0 \qquad \kappa^{(4)} = .4$$

The fourth difference dissipation is for solution damping in smooth regions of the flowfield while the second difference damping is used where sharp gradients in flow quantities exist (i.e., near shocks). Equation (9) is part of the gradient sensitive trigger for the second difference operator. The local Mach number was never greater than .5 for the cases run and, with the fourth difference dissipation sufficient for the inviscid cases, the coefficient for the second difference operator was set to zero.

Time Integration

The time stepping scheme used to fully discretize the system is a four-stage Runge-Kutta integration. The scheme is outlined below for the conservative flow variable vector.

$$\begin{aligned} U_1 &= U^n - \alpha_1 \Delta t\, L(U^n) + D(U^n) \\ U_2 &= U^n - \alpha_2 \Delta t\, L(U_1) + D(U^n) \\ U_3 &= U^n - \alpha_3 \Delta t\, L(U_2) + D(U^n) \\ U_4 &= U^n - \alpha_4 \Delta t\, L(U_3) + D(U^n) \\ U^{n+1} &= U_4 \end{aligned} \tag{10}$$

$$\alpha_1 = \frac{1}{8} \qquad \alpha_2 = \frac{1}{4} \qquad \alpha_3 = \frac{1}{2} \qquad \alpha_4 = 1$$

The CFL stability limit for this scheme was found by Jameson [20] to be $2\sqrt{2}$. Local time stepping for each cell and residual averaging is used to accelerate the convergence.

Boundary Conditions

Boundary conditions are needed for the inlet and exit surfaces of the flowfield domain as well as all solid and periodic surfaces. For the inviscid solution, the boundary condition is zero normal velocity at solid surfaces (endwall and blades). The pressure on solid surfaces is found by extrapolating from the neighboring cells inward in the domain.

In the present calculations, the flow solution is periodic with a period of one pitch. Therefore, all cell surfaces at the circumferential boundaries of the domain (and not defining a solid surface) must take their outward neighboring state variables from the cell at the opposite circumferential bound.

The inlet and exit of the flow domain are subsonic. This requires that four conditions must be set at the upstream boundary and one condition set at the downstream boundary. Two of the four inlet conditions are the flow angles in the z-theta and r-theta planes. The other two conditions may be specified as either total conditions (stagnation pressure and temperature) or as a mass flow condition (density and axial velocity). The experiment which was simulated had a radial gradient in total pressure at the inlet to the blade row, thus the total conditions were specified.

The equations governing the inlet axial velocity are derived from a one-dimensional isentropic approximation of the local flowfield.

$$\frac{\partial C^-}{\partial t} + (u - a)\frac{\partial C^-}{\partial z} = 0 \qquad \frac{\partial C^+}{\partial t} + (u - a)\frac{\partial C^+}{\partial z} = 0 \tag{11}$$

$$u + \frac{2a}{\gamma - 1} = C^+ \qquad u - \frac{2a}{\gamma - 1} = C^- \tag{12}$$

Here, the incoming Riemann invariant is set by a specified inlet condition and the outgoing invariant is found from the flowfield solution. These equations plus the isentropic and energy relations determine the inlet flow in time and space. For the downstream boundary, the static pressure at the hub is independently set. The pressure over the rest of the boundary is governed by the simple radial equilibrium relation.

$$\frac{\partial p}{\partial r} = \frac{\rho w^2}{r} \tag{13}$$

All other quantities are extrapolated from the interior.

2.3 Simulation of Hub Treatment

As stated in an earlier chapter, the hub treatment area extended from five percent to ninety-five percent axial chord, and was made up of discrete grooves which move with the rotor. While this provides an unsteady flow in the actual experiment, time resolved velocity vector data [6] showed little deviation from the time averaged data. Smith and Cumpsty [22] also found the unsteady effects in the casing treatment grooves to be of minor importance. It was thus concluded that a steady state simulation of the hub treatment would be an adequate first approximation to the actual flow situation.

The hub treatment effect is viewed as made up of two "components". The first is a suction (removal) area over the downstream portion, and the second is a jet (injection) over the upstream portion of the treatment area. These effects are those seen in the velocity data [6] discussed in the previous chapter. This combination of flow removal and injection can be simulated numerically by modeling the hub treatment area as another inlet to the flowfield domain. For this second inlet boundary area, the flow conditions were set using the same one-dimensional model discussed in Section 2.1.

The four conditions specified at the hub treatment boundary were the r-z flow angle, the r-theta flow angle, and the radial mass flow (density and radial velocity). The r-z flow angle was set at zero and the r-theta angle was calculated from the angle of the treatment grooves and the rotational speed of the hub as shown in figure 2.1. From the velocity data of Johnson [6] and Smith [4], it was seen that the radial velocity near the hub followed roughly a saw-tooth pattern in the axial direction similar to Figure 2.2. Note that only the radial velocity is shown in the figure. Using this characteristic shape for the radial mass flow, the magnitude can be set by prescribing the amount of flow injected (or removed since the two must balance) as a percent of the inlet mass flow. This treatment mass flow was calculated in [6] to be approximately 3.5 percent of the inlet mass flow.

2.4 Viscous Flow Solution Scheme

The inviscid solution procedure formed the framework for a simulation of the Navier-Stokes equations with the modifications described below. The viscous fluid equations of motion are shown in conservative form below.

$$\frac{\partial}{\partial t}\int_V U \, dV + L(U) = L_V(U) \tag{14}$$

The operator L_V contains the viscous and heat transfer terms. For brevity, they are not included here. Appendix B outlines the equations for the various terms in (14).

Turbulence in the flowfield is modelled by a turbulent viscosity:

$$\mu = \mu_l + \mu_t \tag{15}$$

The two layer algebraic model of Baldwin and Lomax [23] is used to calculate the turbulent viscosity. The molecular viscosity is determined by the Sutherland law.

Since molecular and turbulent viscosity are now modelled in the scheme, a modification to the artificial viscosity is required. A Mach number scaling is employed so that artificial dissipation would not influence the viscous regions of the flowfield. The modified second and fourth difference coefficients are shown below.

$$\varepsilon^{(2)}_{i+1/2,j,k} = \kappa^{(2)} \max(\nu_{i+1,j,k}, \nu_{i,j,k}) \min\left(\frac{M_{i+1/2,j,k}}{\overline{\overline{M}}}, 1 \right) \tag{16}$$

$$\varepsilon^{(4)}_{i+1/2,j,k} = \max\left(0, \kappa^{(4)}_{i+1/2,j,k} \min\left(\frac{M_{i+1/2,j,k}}{\overline{\overline{M}}}, 1 \right) - \varepsilon^{(2)}_{i+1/2,j,k} \right) \tag{17}$$

The boundary conditions for the solid surfaces are now no flow tangent or normal to the surface. Adiabatic conditions are also imposed at solid surfaces. The inlet and exit boundary conditions for the inviscid code are kept, but an added condition at the inlet is that no viscous shear stress or heat transfer occurs across the boundary.

2.5 Computational Grids

For both the viscous and inviscid solutions, an axisymmetric algebraic H-type mesh is generated. Two-dimensional splines are used to fit mesh locations on and around the specified blade geometry. The same grid is used for inviscid solutions of the smooth wall case as well as the hub treatment case, and shall be referred to as the inviscid grid. Figure 2.3 shows blade to blade planes at midspan for the grid of the inviscid and viscous solutions.

Another grid was generated for a viscous flowfield calculation. This calculation was for a blade geometry with no hub clearance. Table 2.1, containing pertinent statistics about the grids, is shown below.

Table 2.1

Number of Grid Points	Inviscid Grid	Viscous Grid Hub Clearance	Viscous Grid No Hub Clearance
Blade to Blade	29	49	41
Hub to Tip	33	47	33
Hub to Gap	6	9	---
Inlet to Exit	76	111	89
L.E. to T.E.	38	56	44

Figure 2.4 shows a r-theta plane of the grid used in the inviscid calculations. The lower third of the grid is shown to emphasize the grid in the gap region underneath the tip of the blade. A similar plane for the viscous calculation is shown in Figure 2.5.

The grid was formed in this way to help resolve the flow in the gap region. However, this introduces a significant grid distortion (or shear) in the gap near the blade tip. There was concern that such a grid distortion would introduce significant numerical errors to the flowfield solution. An investigation of the effect of this grid shear on the flow solution was carried out and is reported in Appendix A. The main conclusion is that there is not a strong effect of the shear on the tip flow solution.

A magnification of a z-theta grid plane around the leading and trailing edges of the viscous computation grid is shown in Figure 2.6. As is typically found with H-type grids, these areas are not very well resolved and are regions of high shear.

2.6 Convergence Criteria and Behavior

For a converged steady state solution, the time dependant terms in the equations and would ideally go to zero. However, this criterion is not practical because of the extremely long run times that would be required. Typically, the time derivative of the density is used to judge the amount that the numerical calculation has converged to a steady state. The average value of the density derivative was observed as well as the L_2 norm of the change (between time steps) of the flow variables for the entire domain. When the magnitudes of these values had been reduced a significant amount (usually two to three orders of magnitude) from their original values, the solution was judged to be converged. Figures 2.7 through 2.10 show the convergence history for the cases studied. Table 2.2 outlines the numerical solutions and their geometrical configurations.

Table 2.2

1.	Viscous solution	hub clearance, moving smooth hub
2.	Viscous solution	no hub clearance, stationary smooth hub
3.	Viscous solution	no hub clearance, moving smooth hub
4.	Inviscid solution	hub clearance, smooth hub
5.	Inviscid solution	hub clearance, hub treatment

Chapter 3
Comparison of Numerical Solutions to Experiments

3.1 Introduction

As was stated in the previous chapter, both viscous and inviscid flowfield solutions were generated for the internal geometry (blades and endwalls) of the research rig with the smooth hub configuration. An inviscid flow solution with a model simulating the hub treatment seen in the experimental rig was also generated. Table 2.2 showed the numerical solutions and their geometrical configurations.

The experimental inlet conditions to the stator blade row were reproduced (with small deviations to the actual conditions) in the numerical solution as well. These inlet conditions were the same for all the numerical cases listed in Table 2.2.

The viscous and inviscid solutions for the smooth hub configuration (i.e., cases 1 and 4) were compared to the experimental data of the same configuration. The inviscid hub treatment solution (case 5) was compared to hub treatment experiment data. Velocity measurements taken in the lower third of the blade passage were the primary source of experimental data used to compare with the numerical solutions. This data was studied in a variety of ways to determine how well the numerical scheme captured the important flow structures in the endwall region. Good comparison of the general flow features was found between the numerical solutions and the experimental data. This was the primary objective, for analysis of the flow features is desired instead of a detailed verification of the computational scheme.

3.2 Smooth Wall Cases

Passage Total Pressure and Flow Angles

Figure 3.1 shows the flow angles measured upstream of the stator blade row for the smooth wall experiment. Figure 3.2 shows a profile of the stagnation pressure coefficient at the same measurement location. The coefficient is the difference between the local total pressure and the ambient reference pressure divided by the inlet dynamic pressure at the midspan ($(P_T - P_0)/Q_m$). These quantities were used to establish the axisymmetric inlet condition to the calculation.

Flow angles were measured downstream of the blade row in the experiment and are compared to values taken from the inviscid solution in Figure 3.3. Roughly the same amount of turning is done in the numerical solution, but there is a discrepancy between the experiment and computation in the lower portions of the passage. This is due to the clearance flow in the numerical solution not mixing out after it leaves the blade.

The stagnation pressure coefficient at the same down stream location is compared in Figure 3.4 for the experiment and the viscous flow solution. The pitch averaged values for the numerical solution show that the overall total pressure profile is similar to that of the experiment.

Velocity Vectors

Velocity data in the experiments was taken on a grid similar to that shown in Figure 3.5. The first radial plane of data was taken at two percent span (roughly the blade tip) and the last radial plane was at twenty-seven percent span. For the comparison, the numerical velocities were interpolated from the numerical solution grid to the experimental data locations.

In viewing the velocity data, the three dimensional vectors had to be portrayed in a two dimensional figure. To do this, planes of data were first chosen similar to the one shown in Figure 3.6, which shows a "radial plane" of data (i.e., a plane at a constant radius). The dashed line in the figure outlines a radial section of an axial plane of data. The angle at which the vector data was viewed is found to be important in discerning flow features. For most axial planes of data, the view angle chosen is the stagger angle of the blades. This is displayed in Figure 3.6 by the lower eyeball with a dashed line at the viewing angle. This angle gives a perspective of looking down (or up) the passage between the blades and will thus be referred to as a passage view. An axial view (i.e., a viewing angle in line with the axis of the machine) is also shown in the figure.

To illustrate the significance of the view angle, Figure 3.7 displays experimental velocity data for the 100% chord axial plane at the two view angles. In the axial view the axisymmetric component of the tangential velocity is large and overshadows the non-axisymmetric flow feature. With the passage view, the tangential velocity is reduced and the flow pattern associated with a tip clearance vortex is clearly brought out. More effects of view angle on the velocity data will be discussed in Chapter 4.

Chordal planes of data were also used. One radial section of such a plane is shown by a dashed line in Figure 3.8. The viewing angle, which is perpendicular to the stager angle of the blades, is also shown in the figure; this will be referred to as a chordal view.

Velocity vectors on the first radial plane of data (at two percent span) are shown in Figure 3.9. The figure shows the data for the experiment and the viscous and inviscid numerical solutions. Similarity between the experiment and the two numerical solutions is seen at this radial location. This radial position is the same as the blade tip and the strong crossflow which results from the tip leakage fluid is apparent. Similarity between the experiment and the two numerical solutions is also seen in the line of interaction between the passage through flow and the cross flow.

Velocity vectors for the second radial plane (at six percent span from the hub) are displayed in Figure 3.10. Similarity is seen between the experiment and the numerical solutions in this plane of data as well. Since the clearance flow has the greatest effect on the two percent span location however, the comparison will focus mostly on that plane.

While the velocity vector data is useful for showing the basic similarity between computation and experiment, more detailed comparisons can be seen if the data is displayed as a contour plot. Figure 3.11 shows contour plots of velocity magnitude over the average inlet axial velocity ($|\vec{u}|/CX$) for the experiment and the computations at the two percent span location. Similarity is seen between the viscous calculation and the experiment. In the contour plot of the inviscid calculation, a higher velocity is seen in the cross flow region, but the relative magnitudes are still similar in pattern.

Velocity vectors in chord planes at seventy percent pitch from the blade pressure surface for the smooth wall cases are seen in Figure 3.12. The significant feature in this plane of data is the outward radial velocity near the hub near the midchord axial location. When this flow feature was first seen in the experimental data, it was thought to be an endwall separation, but the behavior is seen in the inviscid solution which has no viscous endwall boundary layer.

The cause of the radial velocity pointed out in Figure 3.12 is introduced in Figure 3.13, which shows velocity vectors on axial planes at 90% chord. In the figure, the fluid motion associated with a tip vortex emanating from the blade to the right of the passage can be seen. It is the vortical motion seen as an upwash region to the left of the vortex which causes the radial velocity near the hub.

The clearance flow (and the consequent clearance flow vortex) are the major fluid mechanical features in the end wall region, and both numerical solutions capture these features. The strength of the clearance vortex in the numerical solutions is similar to the experiment and the main difference is that the position of the vortex (i.e., the trajectory) was different in the inviscid solution.

To determine further the agreement between experimental data and numerical solutions, vorticity was calculated from the velocity vectors. Contours of vorticity are shown in Figure 3.14. The vorticity is nondimensionalized by the inlet average axial velocity and the blade chord (i.e., ω C/CX). The magnitude of the vorticity associated with the clearance vortex is the same for all the smooth wall cases.

As a final comparison, the circulation was calculated in the passage. The circulation calculated as a line integral around the plane of velocity data gives a good estimate of the vorticity normal to the plane at that point in the passage. As the path of the clearance vortex (symbolized by the thick line in figure 3.15) is not perpendicular to an axial plane of data, an approximate "cross flow" plane of data was chosen. This plane, shown in figure 3.15 as a dashed line, is perpendicular to the stagger angle of the blades.

Figure 3.16 shows the velocity vectors for the cross flow plane of the previous figure. Khalid [24] found that the circulation (nondimensionalized by the blade chord and CX) calculated around the perimeter of the plane of data (on the path shown in the upper plot) is as follows:

1) Experiment	.68
2) Viscous calculation	.58
3) Inviscid calculation	.79

The circulations found for the numerical solutions bound the value calculated for the experiment to within 16%.

3.3 Hub Treatment Cases

Velocity Vectors

The experimental velocity data was taken at the same physical grid locations as the smooth wall case. The hub treatment inviscid numerical solution was interpolated to these experimental grid locations as before.

Velocity vectors on the radial plane at two percent span are shown in Figure 3.17 for the hub treatment experiment and numerical calculation. In both cases a strong jet flow from the forward portions of the treatment is observed.

For a more detailed examination of the data, the radial velocity (v/CX) at the plane at 2% span was isolated and shown as a contour plot in Figure 3.18. The two contour plots are quite alike in their magnitude of radial velocity as well as the pattern the relative magnitudes take. The only significant difference seen is the higher downward velocity in a downstream portion of the plot for the numerical solution.

Figure 3.19 shows contour plots of the magnitude of the velocity ($|\vec{u}|$/CX) for the two cases. Again, the numerical solution appears to pick up the salient flow features.

Velocity vectors on an axial plane at 90% chord are displayed in Figure 3.20 (passage view angle). The downward velocity into the treatment area is apparent in both the experiment and numerical solution. Both plots show a vortical structure in the left portion of the passage. However, it should be noted that this vortical fluid pattern was not picked up originally in the numerical solution when interpolated to the grid locations. The interpolation locations were shifted 5% of the blade pitch closer to the pressure surface (to the left) and the interpolation made to these adjusted locations is seen in the figure.

Finally, Figure 3.21 shows velocity vectors on the cross flow plane defined in Figure 3.15. Both the experiment and numerical solution show a similar vortical pattern. Nondimensional circulation calculated around the planes of data is 1.43 for the experiment and 1.05 for the CFD solution. The difference in circulation between the hub treatment and the smooth hub cases is due to the treatment jet.

3.4 Summary

Numerical solutions for the smooth wall and hub treatment configurations were compared to the experimental measurements. The experimental data used was velocity measurements taken in the endwall region of the passage. Comparison with this data showed that the numerical solutions agreed fairly well with the experiments. In particular it was found that the major flow features in the endwall region (clearance cross flow, vortex, treatment jet, etc.) were captured by inviscid and viscous solutions. A detailed quantitative comparison was not conducted since the research objective was to investigate fluid mechanical trends and global flow features, not to vigorously verify the computational scheme.

Chapter 4
Analysis of Numerical Solutions

4.1 Introduction

A more detailed analysis of the computational solutions follows. Table 4.1 outlines the particular cases studied and their geometrical configurations.

Table 4.1

1.	Viscous solution	no hub clearance, stationary hub
2.	Viscous solution	no hub clearance, moving smooth hub
3.	Viscous solution	hub clearance, moving smooth hub
4.	Inviscid solution	hub clearance, smooth hub
5.	Inviscid solution	hub clearance, hub treatment

The viscous solutions were examined to investigate the effects of hub clearance flow and a moving hub on the endwall region. It was found that a suction surface-hub corner stall existed in case 1 (with no clearance and stationary wall), and case 2 (with no clearance and moving wall). The clearance flow (and the resulting vortex) relieved the corner stall but also generated much blockage in the hub region.

Next, the inviscid solutions were compared to each other to investigate the effects of hub treatment on the endwall flowfield. It was found that the blockage associated with the clearance vortex was removed by the treatment. Further, the two components of the treatment (i.e., the jet and the flow removal) as well as the streamwise vorticity acted in cooperation with each other in removing the blockage.

4.2 Viscous Solutions

4.2.1 No hub clearance/stationary hub

A significant feature of the case with no clearance and stationary wall was a suction surface-hub corner separation. Figure 4.1 shows axial velocity normalized by the average inlet axial velocity (u/CX) one computational cell (0.3% pitch) from both blade surfaces. The figure shows the lower fifty percent of the blade span. The increment between contour lines is one tenth of CX. The pressure surface velocity contour varies little in the radial direction and is not greatly affected in the endwall boundary layer region. The suction surface exhibits a radial variation, starting at the hub at midchord and continuing to 15% of span at the trailing edge, and this is caused by the corner separation.

Axial velocity for radial planes at two spanwise locations (0.4% span and 2.4% span) are shown in Figure 4.2. The corner separation is seen as a defect in axial velocity. Figure 4.3 displays the magnitude of the momentum nondimensionalized by the inlet axial momentum at 2.4% span (this is roughly a measure of $|\vec{u}|/CX$). The defect in momentum caused by the corner stall affects a substantial portion of the passage near the trailing edge. This corner separation is similar to that found by Dong et. al. [14], although the separation shown here is much smaller in extent.

Figure 4.4 and 4.5 show the total pressure loss coefficient for axial planes at two positions down the blade chord. The coefficient is the difference between the local total pressure and the total pressure averaged over the entire inlet, divided by the average inlet dynamic pressure ($(P_T - P_{T\mathrm{in}})/Q_{\mathrm{in}}$). Each division is one tenth of a dynamic head. The boundary on the left and the right of the figures is at 25% pitch and the lower 30% of the blade is shown.

From figures 4.4 and 4.5, the axial development of the blade surface and end wall boundary layers can be shown. At the 36% chord location in Figure 4.4, the boundary layer on the suction surface (left side) is already larger than the one on the pressure surface. This is expected since the peak velocity on the surface was near 20% chord and the flow is experiencing an adverse pressure gradient.

At the 50% chord location, there is an increased build up of low total pressure fluid on the suction surface near the hub. Part of this is due to the migration of boundary layer fluid on the hub to the suction surface. Although the boundary layer at the hub is not large (about 2% of span), the classical secondary flow would result in a migration of endwall fluid toward the suction surface. Boundary layer fluid does not move much down the suction surface. It is also noted that the boundary layer on the endwall, away from the build up, is the same size as the suction surface boundary layer away from the build up.

Figure 4.5 shows the total pressure loss coefficient at two locations further downstream. The loss region in the suction surface corner grows through the passage, and by 79% chord the separation region has formed.

Figure 4.6 displays the flowfield solution in three dimensions. The blue surface in the figure is the lower half of the blade suction surface. The leading edge of the blade is on the left and the trailing edge is on the right. The white lines in the figure outline the hub surface at the leading edge, the trailing edge, and at the line defining the pressure surface of the neighboring blade. The neighboring blade surface is not drawn because it would block the view of the passage.

In the figure, the red and yellow lines represent particle paths where the particle motion is restricted to the planes one computational cell away from the hub and suction surface. The lines are somewhat analogous to oil streak traces. These restricted particle traces were generated to show the effect of the secondary flow and corner separation on the fluid near the surfaces shown. From the figure, one can see in the yellow particle paths the convection of end wall fluid to the suction surface due to secondary flow. The red particle paths outline the separation region and show no strong radial motion down the blade surface.

4.2.2 No hub clearance/moving hub

The case with no clearance and a moving end wall at the hub is described in this section. Although not a practical turbomachinery configuration, this situation was examined to isolate effects of the moving wall on the endwall region from the effects of clearance flow.

Figure 4.7 shows the nondimensional axial velocity 0.3% pitch from the suction surface for the two cases with moving wall and with stationary wall. The two contour plots look similar in that the corner separation apparent in both cases has a similar location and size. The axial velocity is shown for the two cases for radial planes at 1.4% span in Figure 4.8. Again, similarity is seen, with the axial velocity defect occupying the same region for both cases.

The total pressure loss coefficient is shown for axial planes of data in Figure 4.9. At the 50% chord location, the effect of the moving wall on the boundary layer build up is small. The total pressure loss coefficient very near the hub is higher for the moving wall case, because of work done on the fluid by the moving hub. However, this affects only the fluid very close to the hub (less than 1% span), and the size of the endwall boundary layer changes little. The loss coefficient for axial planes at 79% chord is shown in Figure 4.10, where the corner separation is present and a loss area associated with it is seen. Again the moving wall is seen to have little effect on the overall endwall flowfield.

4.2.3 Hub clearance/smooth moving hub

With clearance introduced, the lower blade and endwall flow changes entirely. Figure 4.11 shows axial velocity on two planes. The figure can be compared to the no clearance/stationary hub case shown in Figures 4.1 and 4.2. At 0.2% pitch from the suction surface there are no unusually low velocities near the blade tip. In fact, higher velocities are apparent in the midchord region near the blade tip. This high velocity is due to the action of the clearance vortex, and will be discussed in the next section. The negative velocity contours in the gap represent clearance flow.

The radial plane at 2.4% span in Figure 4.11 also shows strong differences compared to the no clearance cases of Figure 4.8. There is now no suction surface separation. The only low axial velocities are the ones associated with blockage at the center of the passage near the trailing edge; this is associated with the clearance vortex, as will be shown in greater detail subsequently.

Figure 4.12 shows velocity vectors at one computational grid location (0.2% pitch) away from the suction surface. The lower half of the blade is shown for the no hub clearance/stationary wall case and for the clearance case. For the no clearance case there is a region of low velocity due to a separation near the trailing edge close to the hub. The clearance case shows no separation on the blade. Note that the vectors near the hub with the negative axial velocity are in the clearance gap. The velocity vector pattern near the blade tip is caused by the clearance vortex.

Clearance vortex/clearance flow

The clearance flow and resulting vortex are fundamental features in the endwall flowfield. For this reason, the study will focus on these features and their effects.

The pattern shown in the last Figure 4.12 is better understood by examining the flowfield in axial planes. Figure 4.13 thus shows velocity vectors in an axial plane at two locations. The vectors are viewed at an angle in line with the local camber angle of the blades. At the 36% chord location, a vortex is shown forming close to the tip of the blade. The flow around the vortex creates a stagnation region (on this plane) on the suction surface of the blade. The positive radial motion observed near the leading edge in Figure 4.12 is caused by fluid being drawn to the blade surface by the vortical motion and spreading radially along the surface.

At the 64% chord location the vortex has grown and moved away from the blade. The radial motion near the suction surface is now downward and is again part of the vortical motion.

Role of the vortex in mixing

The previous paragraphs explained some effects the clearance vortex has on the flow near the blade suction surface. The effect of the radial motion appears to be important in energizing the boundary layer near the blade tip.

Figure 4.14 shows the total pressure loss coefficient for two axial planes. The axial locations of these planes are near the locations for Figure 4.4 and thus, the two cases can be compared directly. At the 36% chord location a difference in the suction surface boundary layer can already be seen. The clearance flow has convected away the boundary layer that was on the endwall and on the lowest portion of the suction surface. Secondly, the boundary layer fluid that was on the lowest portion of the blade suction surface is being entrained into the clearance vortex. From the data at the second axial position, it is seen that this fluid travels with the vortex away from the blade surface.

The mixing effect of the vortex is shown from the two planes of data. The vortical action draws higher total pressure fluid from outside the boundary layer close to the blade surface. As observed in Figure 4.15, this scouring, or reenergization, of the boundary layer on the blade suction surface near the tip continues along the passage.

Vortex source and location

A vortex has been identified in the axial planes of Figure 4.13 and its effect of removing the corner stall has been shown in Figures 4.14

and 4.15. However, its source (or formation) and its detection need further examination. Streamwise vorticity is produced whenever a jet is injected crosswise to a flow. A recent example of this is seen in the work of Johnston & Nishi [15], who exploited this when they introduced jets skewed to the through flow to produce vortices in their experiment. In the same way a clearance flow jet also has streamwise vorticity associated with it. When a gap is opened up, the bound vorticity on the blade is shed at the tip. Chen [25] has reproduced the vortex trajectory for many different blade rows and clearances by predicting the shed vorticity in this way.

A blade with clearance sheds vorticity continuously along the length of the blade. The clearance vortex is thus not an isolated vortex line, but a continuous sheet of vortex lines which is "rolled up" into a vortex core as shown in Figure 4.16. This creates a flow pattern like the one shown in Figure 4.13; from such a pattern one can infer the position of the vortex "center".

One can see a vortex center in the plots of Figure 4.13, but this is a visual judgement on velocity vectors viewed at a particular angle. In fact, if the viewing angle is changed severely, no vortex can be seen at all (see Figure 3.7). Figure 4.17 further demonstrates this point. The figure shows velocity vectors for an axial plane at 90% chord. The upper plot shows the vectors viewed at an angle equalling the local camber angle of the blades (about 31 degrees). The plot below it shows the same vectors viewed at an angle of 55 degrees, which is about the angle that the vortex trajectory has in the passage. In the lower plot, the vortex is more clearly defined. The perceived vortex center has been circled in both planes and the centers are reproduced at the bottom of Figure 4.17. There is a significant radial difference (one clearance height) between the two perceived vortex centers, and a lesser difference in the circumferential position of the centers.

It would be useful if some quantity (preferably a scalar one) could be calculated which would find the position of the vortex core or "center" unambiguously. Three contour plots of various quantities (streamwise vorticity, static pressure and total pressure) are shown in Figure 4.18. Superimposed on the plots are velocity vectors viewed at the vortex trajectory angle. The "X" shown in the plots marks the vortex center as seen in the velocity vectors. The streamwise vorticity lines up well with the vortex but does not specifically locate the center. The low point in static pressure differs from the vortex center by about 8 percent of the blade pitch. The low total pressure center comes very close to the vortex center (3% of pitch) identified from the velocity vectors. The results of Figure 4.18 show that all three quantities are roughly correct at locating the vortex. In this case, however, the total pressure locates the vortex center most precisely. The streamwise vorticity was thought to be the quantity that places the center of the vortex. Perhaps viscous or numerical diffusion has obscured the vorticity in the core. Also, the vorticity is in a diffusing blade passage which would reduce the amount of streamwise vorticity seen.

Clearance flow

In Figure 4.14, the stripping away of the end wall boundary layer by the clearance flow is observed in the forward portions of the blade passage. To see the action that this endwall flow takes, one can examine Figure 4.19, showing velocity vectors near the hub (0.3% span). The two curved lines on the figure represent the camber lines of the blades.

Velocity vectors at the 2% span location are shown in Figure 4.20. Note the line of interaction between the cross flow and the through flow.

In Figure 4.14 it is observed that the flow going through the blade gap is at a higher total pressure than the fluid near the hub. To determine where most of the fluid going through the gap comes from, particle paths in the 3-D flowfield were generated. Figure 4.21 shows the particle paths. The blue surface is the blade suction surface, the left side is the leading edge, and the hub is outlined in white. The neighboring blade surface is not displayed because it would obstruct the view of the passage.

Particles were released in the gap under the invisible blade and the velocities were integrated backward in time to learn where specific particles came from. Yellow lines represent particles released at the top of the gap just below the blade tip. The red lines represent particles released just above the hub in the gap. Some of the fluid going into the gap comes from the clearance flow of the neighboring gap, as seen by the red paths running across the hub. Some fluid comes from the suction surface of the neighboring blade across the pitch. The paths representing this fluid follow the suction surface, become imbedded in the strong crossflow near the hub, and cross the passage near the trailing edge. Most of the fluid going into the gap, however, seems to come from an area (at the passage inlet plane) closer to the pressure surface. The area at the inlet plane of the passage bound by the paths ranged from 1.5% to 6% span. This is outside the range of the endwall boundary layer and thus, the flow going into the gap comes from an area of higher energy flow than the endwall fluid with which it is mixing.

Pressure loss in the vortex

From the pressure loss coefficient plots of Figures 4.14 and 4.15, it is observed that there is a region of low total pressure fluid in the vortex core. Figure 4.22 also shows pressure loss coefficient at the 2.4% span location for the clearance case and the no clearance/stationary wall case. The high loss area corresponding to the corner separation in the no clearance case is not present in the clearance case. However, high losses are present across the passage in the clearance case. This low total pressure area follows the path of the vortex. The source or generation of this loss is the subject of this section.

Figure 4.23 shows contour plot planes in the 3-D flowfield. In the figure, the blue surface in the upper right corner is the suction surface of the blade from midchord to the trailing edge. The trailing edge of the blade is on the right and the hub is outlined in white. The view is looking down at the exit plane of the passage. The neighboring blade that should be to the left is not plotted. The large surface in the upper portion of the figure is an axial plane of data at 50% chord. On it is displayed the total pressure divided by the reference ambient pressure. The color scale in terms of the total pressure loss coefficient ranges from red ($(P_T-P_{Tin})/Q_{in} \sim 0$) to blue ($(P_T-P_{Tin})/Q_{in} \sim -0.8$). The other colored surface is another axial plane showing total pressure. This plane is at 80% chord and only shows the lower 8% of the blade span. The figure shows the low total pressure associated with the clearance vortex at 50% chord. At 80% chord this loss or blockage region has grown to occupy much of the endwall region. The lowest total pressure fluid has moved and is outlined by the box shown, which will be referred to as the high loss box.

To make sure the highest loss fluid was being tracked by stream lines, and to see where the high loss fluid was coming from, particles were released in the lowest total pressure region at 50% chord and tracked both forward and backward in time. The paths integrated forward in time fell in the high loss box and thus, the particle paths tracked total pressure. When the particle paths integrated backward in time were examined, it was found that all of the paths came from the suction surface near the tip and under the blade.

Progressing from that observation, particles were released along the suction surface in the lower 4% of the blade span. These particle paths are displayed in Figure 4.24. In the figure, the red lines are particles released from 10% to 40% chord locations. The yellow lines are particles released at 50%, 60%, and 70% chord locations. The red particles form helical paths as they are caught up in the vortex flow, and pass into the high loss box which has been reproduced in the figure. The yellow particles also form helical paths, but their paths end up outside the box.

Particles were also released at the tip two computational cells (0.2% span) underneath the blade, as shown in Figure 4.25. In this figure, the exit of the passage is viewed from a position below the radial plane of the hub. The hub is only outlined in white so that one can see through it (i.e., so that the under side of the blade, where the particles originate, may be observed). The yellow paths originate from the first 40% of the blade chord. These particles are entrained in the vortex core and end up in the high loss box. The red paths originate from 50% to 80% of the chord. The particles end up encircling the loss box.

Finally, particles were released from two cells below the blade tip over the last 20% of the chord. These are shown in Figure 4.26. In the figure, the exit plane of the passage is viewed from a position above the hub. The paths from the previous figure are reproduced, but continue to the trailing edge plane, instead of stopping at the axial plane where the high loss box is located. Green lines represent the particles released over the last 20% of the chord. These particles are convected across the passage, and through vortical action end in radial positions higher than the blade gap.

The boundary that the green and red particles make at the exit of the blade row is extremely similar to the boundary that the low total pressure fluid has at that axial location. This pattern is shown in Figure 4.23 by the plane of data at the further downstream location.

It is observed in Figures 4.14 and 4.15 that there is high loss fluid coming from over the blade tip. Much of this fluid appears to be convected across the endwall region, resulting in blockage on the endwall near the rear of the passage.

4.2.4 Viscous Investigation Summary

For the case with no hub clearance and stationary wall, a build up of boundary layer fluid was found on the blade suction surface near the hub. This later developed into a corner stall near the trailing edge.

Moving the wall under the sealed hub did not reduce the boundary layer build up appreciably. In particular it did not relieve the corner stall.

When a gap was opened up between the blade and the hub the flowfield changed greatly. The corner stall was removed by the clearance flow and vortex. The clearance flow was found to scour away the endwall boundary layer over the first half of the blade chord. The flow structure associated with the vortex was inherent in the corner stall removal, by bringing higher momentum fluid into the suction surface boundary layer.

The clearance vortex also serves as a repositor of total pressure loss. It was found that much of the loss fluid associated with the clearance vortex core emanates from the blade surface boundary layer and the blade tip. The clearance flow and vortex are thus primary contributors to endwall blockage.

4.3 Inviscid Solutions

The hub treatment was modelled in an inviscid flow solution. Time did not permit the generation of a viscous solution of the hub treatment case. To have a more consistent comparison of the effects of the treatment, an inviscid solution of the smooth hub configuration was used as a basis for comparison. Section 4.3.1 introduces the inviscid smooth wall solution and outlines the similarity between it and the viscous/hub clearance/smooth hub solution. In Section 4.3.2, the effects of the hub treatment are examined.

4.3.1 Hub clearance/smooth hub

The inviscid solution for the smooth wall configuration exhibits the main endwall flow features shown with the viscous calculation. To briefly display this, Figure 4.27 shows velocity vectors on two axial planes. The view angle is 55 degrees and the lower 20% of the passage is shown. At the 40% chord location the vortex forms off the suction surface of the blade. The vortex has left the blade tip and is half way across the passage at the 80% chord location. The extent of the cross flow is also apparent at this location.

Figure 4.28 shows total pressure loss coefficient ($(P_T - P_{Tin})/Q_{in}$) for the same axial planes of data. At the 40% chord location there is a total pressure loss associated with the clearance vortex at the right side of the passage. A high blockage area, similar to the one observed in the viscous case, forms near the endwall by the 80% chord location. The source of this inviscid loss region is a topic covered in Appendix A.

4.3.2 Hub treatment

The hub treatment case has a fundamentally different endwall flowfield. The two components of the treatment, the jet and the removal, act to change the endwall stream pattern and energy makeup entirely. To demonstrate this, Figure 4.29 shows contours of total pressure loss coefficient on a radial plane at 1% span for the smooth hub and hub treatment cases. The jet of the hub treatment appears as the high total pressure region near the leading edge of the lower plot. The total pressure in the jet is greater than the inlet total pressure by as much as five times the inlet reference dynamic head. In fact, all areas of the hub treatment case are between 0.75 to five times the inlet dynamic head higher in total pressure than the smooth wall case.

Figure 4.30 shows velocity vectors for the hub treatment case at two axial locations. The vectors are viewed at an angle 55 degrees from axial, which is roughly the angle that the vortex has as it crosses the passage. At the 10% chord location, the jet flow is seen coming at an angle from the treatment area. At the right of the passage there is a vortex forming near the tip of the blade. This area of vorticity grows and moves away from the blade by the 40% chord location. At that location, less jet flow is seen but there is a high velocity flow moving up the pressure surface of the blade at the left of the passage. This flow on the pressure surface originates from the jet shown at the 10% location.

Velocity vectors on two more axial planes are shown in Figure 4.31. At the 60% location, the vortex has moved across the passage and the vortical pattern has spread somewhat. Fluid is also beginning to be drawn off at the hub. The suction effect is stronger at the 80% chord location. The vortex at the 80% location has moved further across the passage and is being influenced by the treatment suction.

Streamwise vorticity nondimensionalized by the axial chord and CX (i.e., ω_S C/CX) is displayed for two axial positions in Figure 4.32. At the 10% chord location, the vortex is forming near the tip of the blade on the right of the passage. By 40% chord the high vorticity area has increased and moved away from the blade tip.

Figure 4.33 shows streamwise vorticity for the inviscid smooth hub solution at the same axial locations as Figure 4.32. At the 10% chord position only a small region of streamwise vorticity is seen near the blade tip when compared to the hub treatment solution. At 40% chord the streamwise vorticity associated with the clearance vortex has increased, but it is still small compared to the hub treatment solution. The treatment jet is generating more streamwise vorticity than the clearance flow, as one might expect from the very high dynamic pressure of the jet. This is reflected in these figures and in the hub treatment circulation calculations done in Chapter 3.

Streamwise vorticity for the hub treatment solution at two more axial locations is shown in Figure 4.34. At the 60% chord location the vortex generated by the treatment jet has moved across the passage and is being drawn down to the hub by the suction. By the 80% chord location, the vortex has moved to the other blade and much of the high vorticity fluid has been sucked into the treatment area.

The effect of the treatment on the flow near the blade surfaces is seen in Figure 4.35, which shows velocity vectors one computational cell (0.2% pitch) from the blade suction and pressure surfaces. The lower

40% of the blade is displayed in the figure. On the suction surface, the velocity pattern near the leading edge is due to the forming vortex and is similar to the flow pattern seen in Figure 4.12. The negative radial velocities in the region beyond the midchord are effects of the treatment suction. On the pressure surface the jet fluid flows radially outward, away from the endwall.

To demonstrate the effect hub treatment has on the end wall flowfield from another view, figures of total pressure loss coefficient on axial planes are shown. Planes at 10% chord for the smooth wall and hub treatment cases are displayed in Figure 4.36. The figures show the lower 20% of the blade span. At this axial location, a high total pressure jet emanates from the hub for the treatment case.

Figure 4.37 shows the axial planes at 40% chord for smooth wall and for hub treatment. With hub treatment, high total pressure fluid from the jet "fills" the end wall region. Very high total pressure fluid from the jet is against the pressure surface and is headed away from the end wall region. With the smooth wall at this location, the loss area associated with the clearance vortex is beginning to form. With the hub treatment, the vortex does not have low total pressure fluid associated with it. In fact, a high total pressure area, with a coefficient of 1.2, is in the region of the vortex (the effect of this vortex will be shown in later figures). No low total pressure fluid is seen coming from the blade tip in the hub treatment case at all. The high pressure jet washes the blade tip and removes (by mixing) the low total pressure fluid.

At the 60% chord location shown in Figure 4.38, the same total pressure pattern is seen in the hub treatment case. The suction at the hub has the effect of drawing the pressure contours down. For the smooth wall case, the low total pressure area is being convected across the passage.

Planes displaying loss coefficient at 80% chord are shown in Figure 4.39. For the smooth wall case, a region of blockage takes up most of the passage in the endwall region. The same area in the hub treatment case is occupied by high momentum flow. The suction at the rear of the treatment further draws the high total pressure fluid down to the hub. At the left of the figure much of the high total pressure fluid originating from the treatment jet at the front of the passage can be seen. This flow is moving away from the end wall on the pressure surface of the blade.

To get another perspective of the roles of treatment jet, suction, and vortex, particle paths in the 3-D flowfield are displayed. Figure 4.40 shows particles released in the region of the treatment with the highest total pressure (at 10% and 15% axial chord). The lower portion of the blade suction surface is at the top of the figure. Figure 4.41 shows the same particle paths viewed at a different angle, with the view down the blade passage. The leading edge of one blade is at the left of the figure and the lower 40% of the blade span is shown. The neighboring blade at the right of the passage is invisible. The two figures can be used together to help comprehend the path trajectories.

The particles released in the jet are two colors. The red particles were released over 80% of the pitch and the yellow particles over 20% of the pitch near the suction surface. Most of the red particles cross the passage, run into the pressure surface of the blade that is not shown, and follow the surface of the blade as they travel away from the endwall. The yellow particles, however, form helical paths and go back towards the endwall.

This pattern is similar for all of the treatment jet flow examined. About 80% of the high momentum fluid rides up the pressure surface of the blade, and appears to have little effect on the endwall region. The other 20% gets caught up into the vortex flow and is brought down into or close to the hub by the treatment suction.

This flow pattern is shown again in Figure 4.42, which displays a surface of constant total pressure (i.e., Bernoulli surface) in the 3-D flowfield. The leading edge of the blade is at the left of the figure and the lower 50% of the blade is displayed. The surface of constant total pressure (which is a 3-D stream surface) is the green surface starting at the hub near the leading edge. There is a section of the surface in a shadow on the right of the figure which represents the jet flow climbing up the blade pressure surface.

Figure 4.43 shows the Bernoulli surface viewed from the rear of the passage. The surface is seen wrapping around the vortex over the first half of the blade chord and further downstream, is seen going into the hub.

4.3.3 Inviscid Investigation Summary

For the smooth wall case, the inviscid and the viscous solutions had similar flow features. In particular the clearance vortex and cross flow was seen to have common characteristics for the two solutions. A total pressure loss area also existed in the endwall near the trailing edge for the inviscid computation. This was due to an artifact of the artificial viscosity which is discussed in Appendix A.

With the hub treatment, the blockage was removed and higher total pressure fluid was found near the endwall. The mechanism for this is a combination of the treatment jet pumping up the high loss fluid from the tip in the front of the passage, and the suction removing the low total pressure fluid from the blade tip in the rear of the passage.

Lee [10] found a good correlation between stall inhibiting effectiveness of fluid injection and streamwise momentum introduction. The results of the numerical investigation show some effects of this momentum introduction (e.g., tip loss fluid mixing). However, it is noted that much of the momentum of the jet has no role in the endwall region.

Chapter 5
Summary, Conclusions and Recommendations

5.1 Summary and Conclusions

An investigation was carried out of the endwall flowfield to examine effects of hub clearance and hub treatment. Viscous and inviscid numerical solutions were generated of the three-dimensional flowfield around a stator blade row. A numerical solution was also generated for a blade row with a model of an axial skewed groove tip treatment.

The computational solutions were shown to compare qualitatively well to experimental data consisting of detailed blade passage velocity measurements. This was true for both the smooth wall and the hub treatment configurations.

The viscous solutions were examined to determine the effects of clearance flow and a moving wall. With a sealed hub, boundary layer build up occurred in the suction surface corner and separation in this region was found. Wall motion had little effect on the stall. Clearance flow, and the resulting vortex, however relieved the corner stall. The clearance flow and clearance vortex were the most important features of the endwall flowfield. The clearance flow convected away the endwall boundary layer in upstream portions of the blade row, and the mixing associated with the vortex brought high energy fluid to the suction surface boundary layer.

While they remove the suction surface corner stall, the clearance flow and vortex have associated with them a region of low total pressure fluid in the downstream portions of the passage. The vortex: 1) collects high loss fluid from the suction surface and blade tip boundary layer, and 2) increases the net total pressure loss due to viscous mixing in its core. It is suggested that this low momentum region is the source of the large increase in blockage associated with "endwall stall".

With hub treatment there was much higher energy fluid near the endwall. It is thought that removal of the low momentum fluid found in the smooth wall solution by the hub treatment is the chief stall inhibiting effect. This endwall flow energization is accomplished by three mechanisms. First, the high loss fluid coming from the tip of the blade is either mixed out by the high total pressure jet or is sucked directly into the treatment area. Second, the endwall boundary layer is drawn into the treatment by the suction at the rear of the passage and diverted from the endwall by the jet. This is conjecture since there was no endwall boundary layer in the inviscid solution. The third mechanism is the broad mixing of a portion of the momentum in the jet and the endwall fluid by the vortex and suction component.

5.2 Recommendations For Future Work

A next step in the numerical investigation of casing treatment would be to generate a viscous solution of the flow with with a hub treatment model. This can be compared to the inviscid solution to check the effects of viscosity. The author found that the viscous smooth wall solution captured the actual vortex trajectory better than the inviscid solution. Since the vortex position was somewhat incorrectly predicted by the inviscid hub treatment solution, this might be corrected with a viscous flow solution.

Lee [10] shows data on compressor performance vs. jet injection rate. To recreate some of Lee's trends with a numerical simulation would be a significant development for at least three reasons. First, it would demonstrate (or evaluate) the code's ability to create stalling conditions reflecting physical trends. Second, it would give better insight as to what truly generates end wall stall. Third, it would give a better understanding of the particular jet parameters that prevent stall.

In coordination with the recreation of Lee's experimental trends, more numerical experiments could be run to optimize the stall inhibiting components of the treatment. Much of the jet fluid leaves the endwall in the present configuration. Parametric variations of the treatment jet could be performed to optimize the treatment and keep more of the high momentum fluid near the endwall.

References

1. Prince, D. C., Jr., Wisler, D. C., and Hilvers, D. E., "Study of Casing Treatment Stall Margin Improvement Phenomena," NASA CR-134552, March 1974.

2. Takata, H. and Tsukuda, Y., "Stall Margin Improvement by Casing Treatment-Its Mechanism and Effectiveness," ASME J. Eng. Power, Vol. 99, January 1977, pp. 121-133.

3. Greitzer, E. M., Nikkanen, J.P., Haddad, D. E., Mazzawy, R. S., and Joslyn, H. D., "A Fundamental Criterion for the Application of Rotor Casing Treatment," ASME J. Fluids Eng., Vol. 101, June 1979, pp. 237-243.

4. Smith, G. D. J., "Casing Treatment in Axial Compressors," Ph.D. Thesis, Engineering Department, University of Cambridge, April 1980.

5. Cheng, P., Prell, M. E., Greitzer, E. M., and Tan, C. S., "Effects of Compressor Hub Treatment on Stator Stall Margin and Performance," J. Aircraft, Vol. 21, No. 7, July 1984, pp. 469-475.

6. Johnson, M. C., "The Effects of Hub Treatment on Compressor Endwall Flowfields," M. S. Thesis, Department of Aeronautics and Astronautics, MIT, January 1985.

7. Lee, N. K. W., "Effects of Compressor Endwall Suction and Blowing on Stability Enhancement," MIT GTL Report No. 192, January 1988.

8. Koch, C. C., "Stalling Pressure Rise Capability of Axial Flow Compressor Stages," ASME J. Eng. Power, Vol. 103, 1981, pp. 645-656.

9. Rains, D. A., "Tip Clearance Flow in Axial Flow Compressors and Pumps," California Institute of Technology, Hydrodynamics and Mechanical Engineering Laboratories Report No. 5, 1945.

10. More, J., Tilton, J. S., "Tip Leakage Flow in a Linear Turbine Cascade," ASME Paper No. 87-GT-222, 1987.

11. Lakshminarayana, B., "Method for Predicting the Tip Clearance Effects in Axial Flow Turbomachinery," ASME J. of Basic Eng., Vol. 104, 1970, pp. 467-481.

12. Peacock, R. E., "A Review of Turbomachinery Tip Gap Effects," Int. J. Heat & Fluid Flow, Vol. 4, March 1983, pp. 3-16.

13. Senoo, Y., Ishida, M., "Pressure Loss Due to the Tip Clearance of Impeller Blades in Centrifugal and Axial Blowers," ASME J. Eng. Power, Vol. 108, January 1986, pp. 32-37.

14. Dong, Y., Gallimore, S. J., and Hodson, H. P., "Three-Dimensional Flows and Loss Reduction in Axial Compressors," ASME Paper 86-GT-193, June 1986.

15. Johnston, J., Nishi, M., "Vortex Generator Jets-A Means for Passive and Active Control of Boundary Layer Separation," AIAA-89-0564, January 1989.

16. Hah, C., "A Numerical Modelling of Endwall and Tip Clearance Flow of an Isolated Compressor Rotor," ASME J. Eng. Power, Vol. 108, January 1986, pp. 15-21.

17. Pouagare, M., Delaney, R. A., "Study of Three Dimensional Viscous Flows in an Axial Compressor Cascade Including Tip Leakage Effects Using a SIMPLE-Based Algorithm," ASME J. of Turbomachinery, Vol. 108, July 1986, pp. 51-58.

18. Dawes, W. N., "A Numerical Analysis of the Three-Dimensional Viscous Flow in a Transonic Compressor Rotor and Comparison with Experiment," ASME J. of Turbomachinery, Vol. 109, January 1987, pp. 83-90.

19. Jameson, A., Schmidt, W., and Turkel, E., "Numerical Solutions of the Euler Equations by Finite Volume Methods Using Runge-Kutta Time-Stepping Schemes," AIAA-81-1259, June 1981.

20. Celestina, M. L., Mulac, R. A., and Adamczyk, J. J., "A Numerical Simulation of the Inviscid Flow Through a Counterrotating Propeller," ASME Paper 86-GT-138, June 1986.

21. Adamczyk, J. J., Celestina, M. L., Beach, T.A., and Barnett, M., "Simulation of Three-Dimensional Viscous Flow Within a Multistage Turbine," ASME Paper 89-GT-152, June 1989

22. Smith, G. D. J., Cumpsty, N. A., "Flow Phenomena in Compressor Casing Treatment," ASME J. Eng. Power, Vol. 106, July 1984, pp. 532-541.

23. Baldwin, B., Lomax, H., "Thin Layer Approximation and Algebraic Model for Separated Turbulent Flows," AIAA Paper No. 78-257, 1978.

24. Khalid, A., Personal communication (August 1989)

25. Chen, G. T., Progress report on Doctoral research, MIT GTL, 1989.

Table 1.1 Flowpath Geometry

	Rotor	Stator
Hub diameter (mm)	444	444
Casing diameter (mm)	597	597
Number of blades	44	45
Chord (mm)	38	38
Solidity at midspan	1.0	1.0
Aspect ratio	1.9	1.9
Camber (deg)	30	30
O.D. stagger angle (deg)	65	40
Midspan stagger angle (deg)	60	42.5
I.D. stagger angle (deg)	55	45
Blade clearance (mm)	0.8	1.5

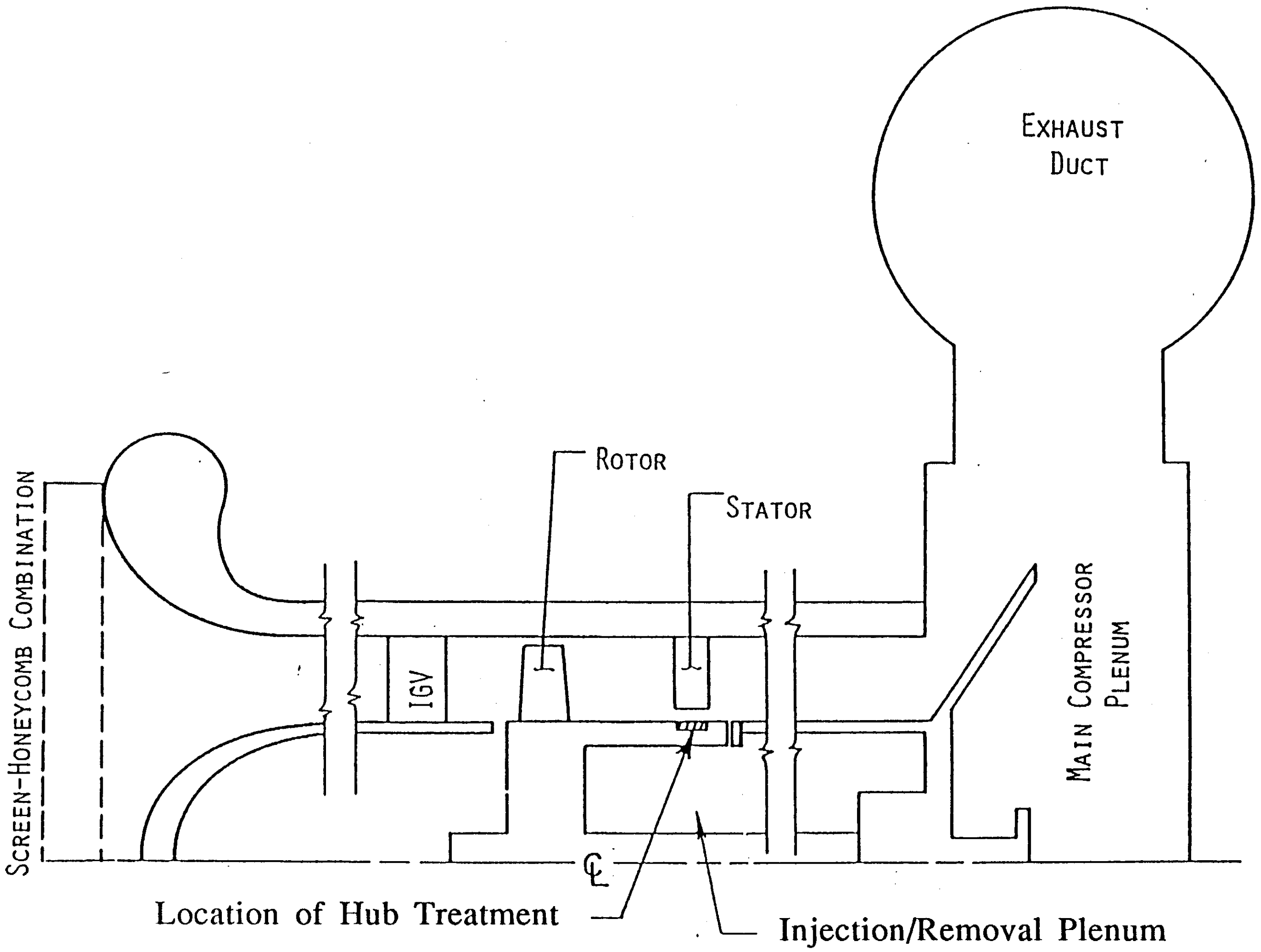

Figure 1.1 Schematic Drawing of Compressor Research Rig

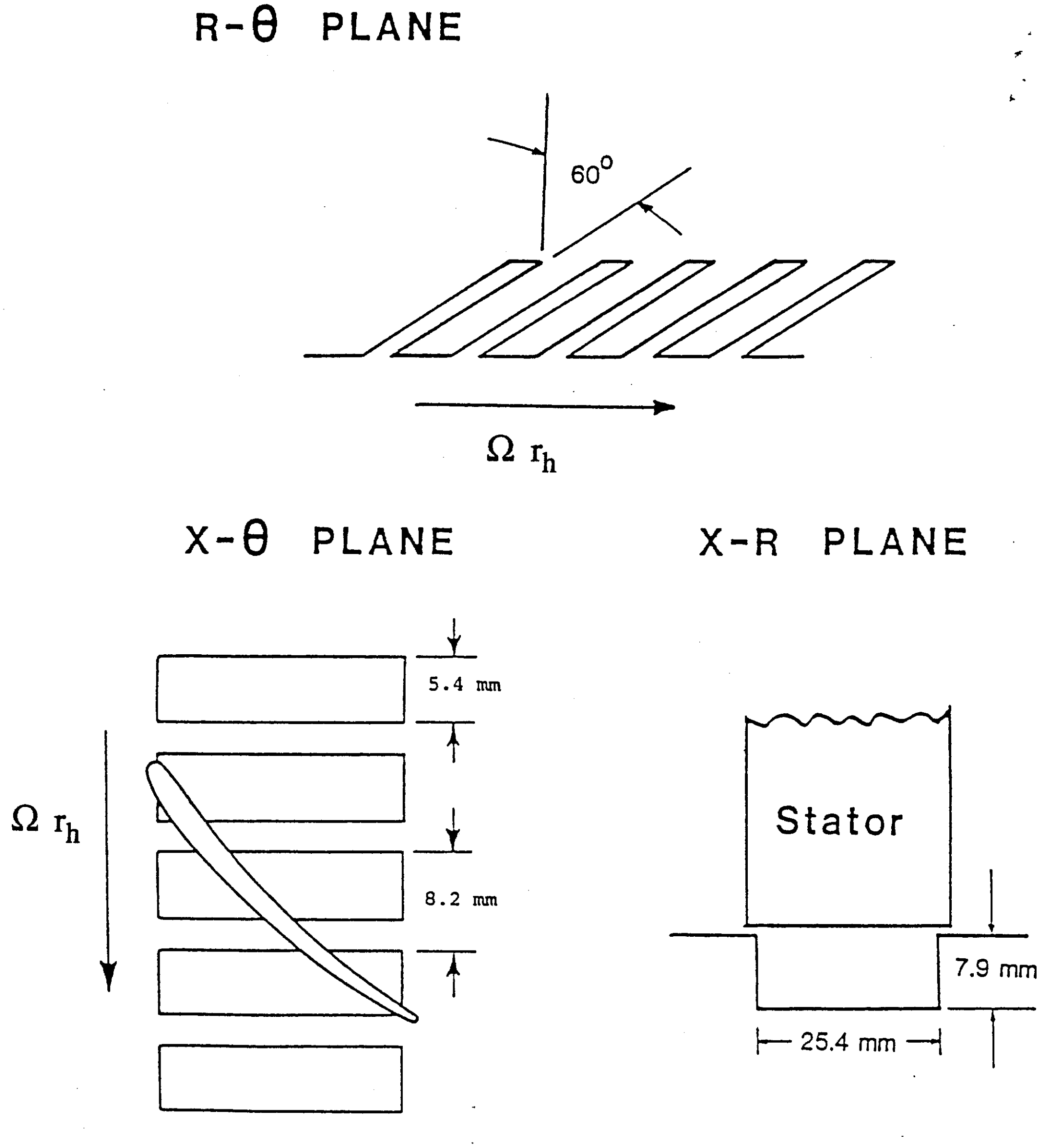

Figure 1.2 Detail of Hub Treatment

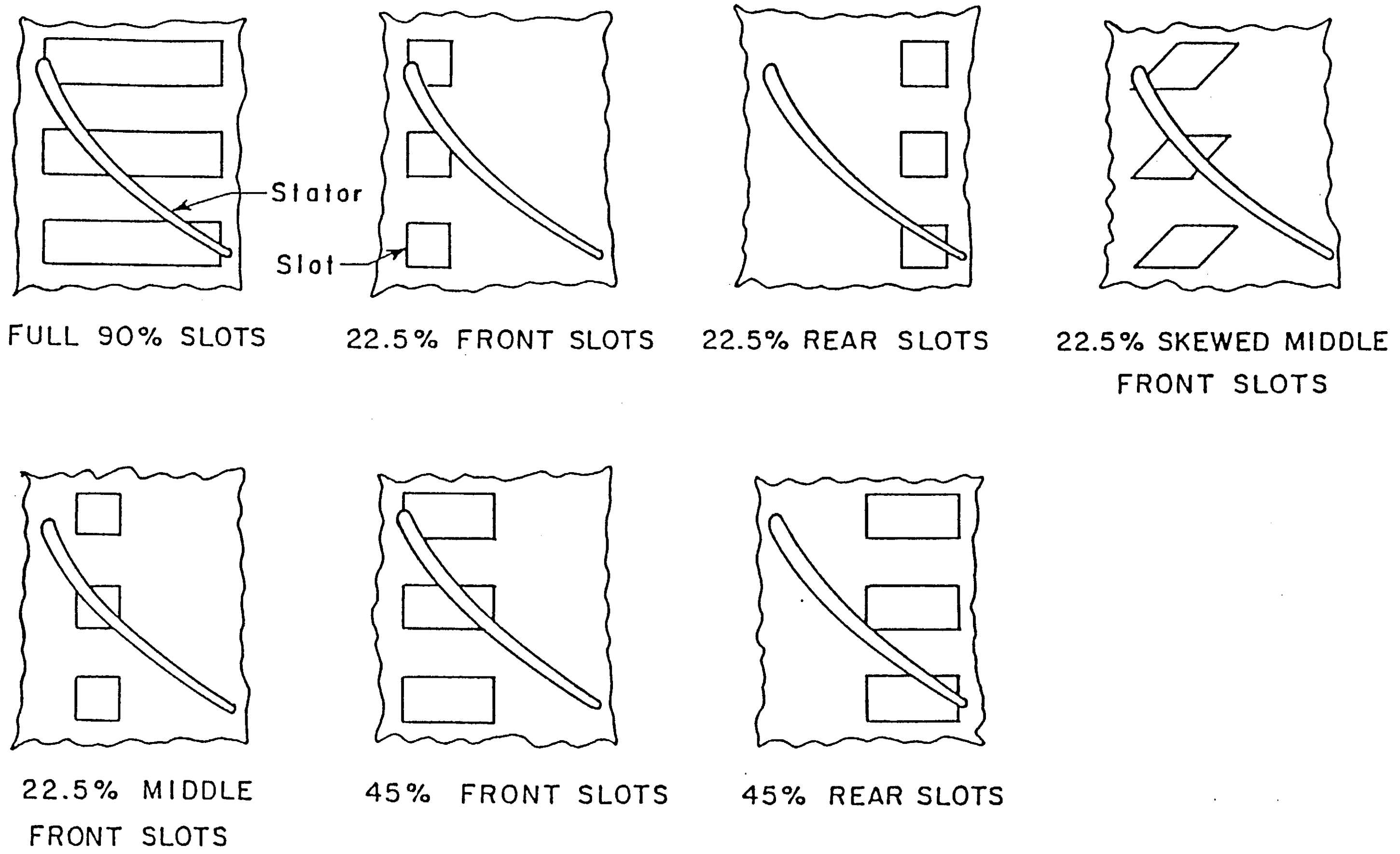

FULL 90% SLOTS

22.5% FRONT SLOTS

22.5% REAR SLOTS

22.5% SKEWED MIDDLE FRONT SLOTS

22.5% MIDDLE FRONT SLOTS

45% FRONT SLOTS

45% REAR SLOTS

Figure 1.3 Injection/Removal Configurations

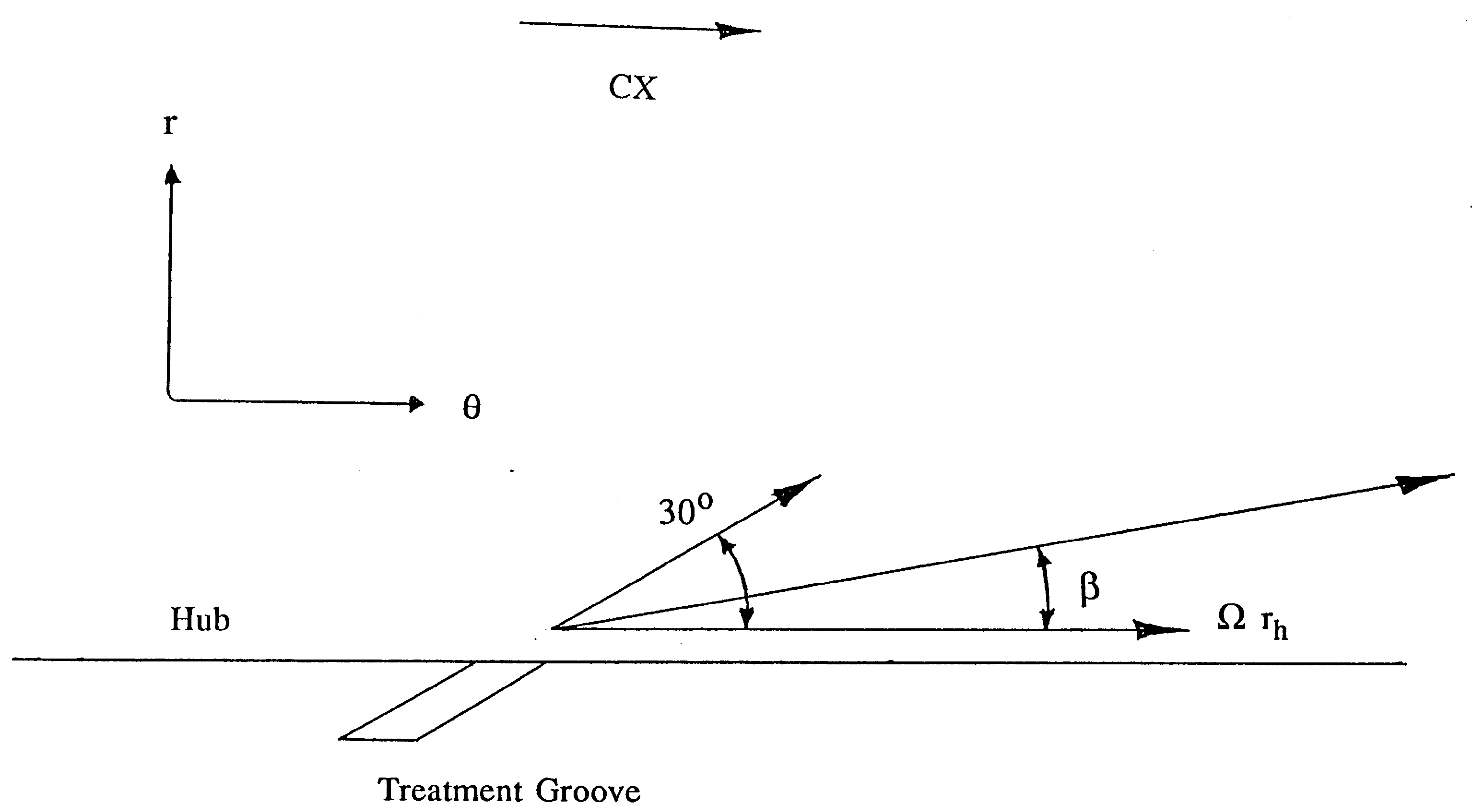

β = Flow Angle Leaving Hub

Figure 2.1 Flow Angle Leaving Treatment Area

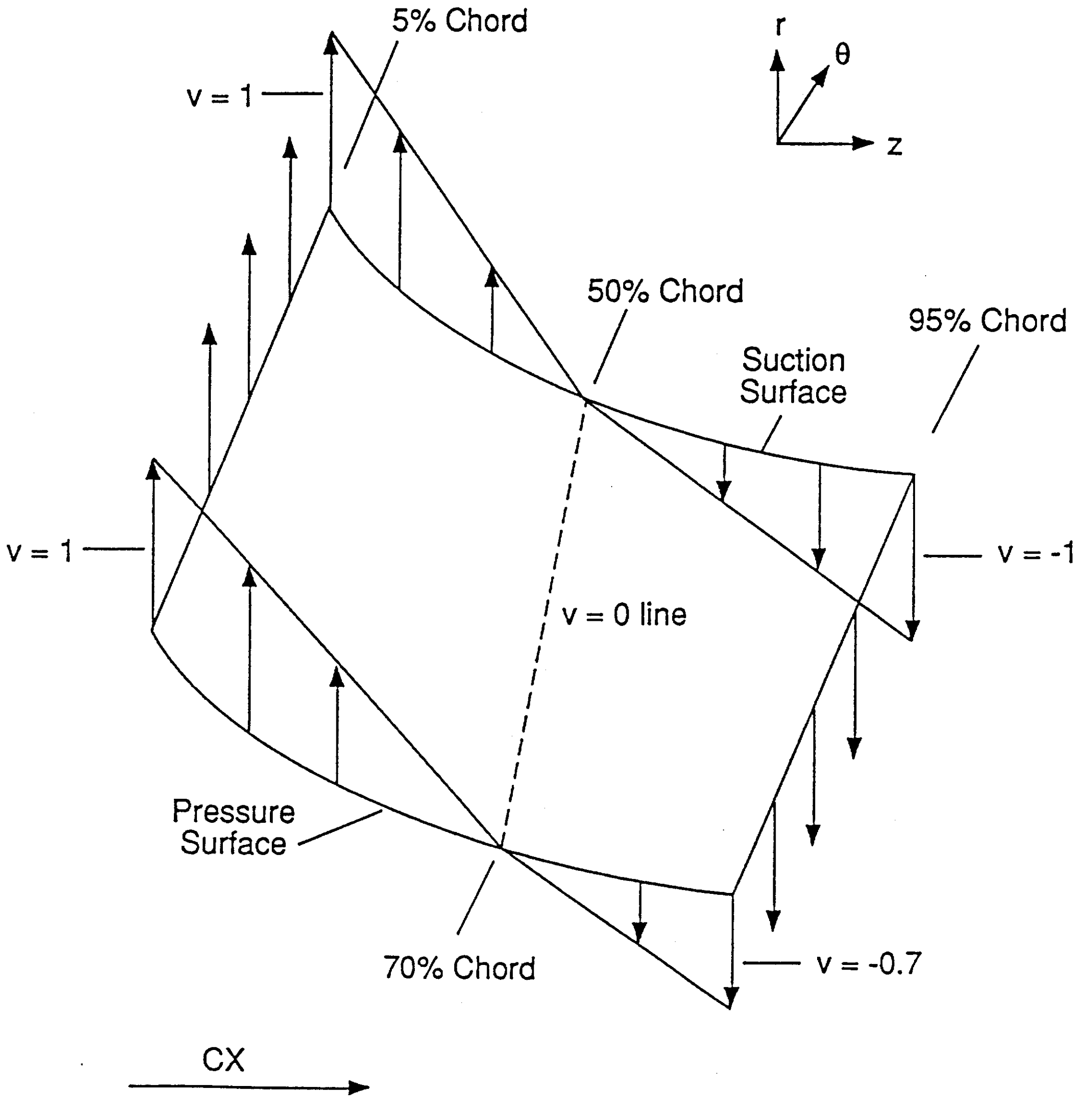

Figure 2.2 Hub Treatment Radial Velocity Profile

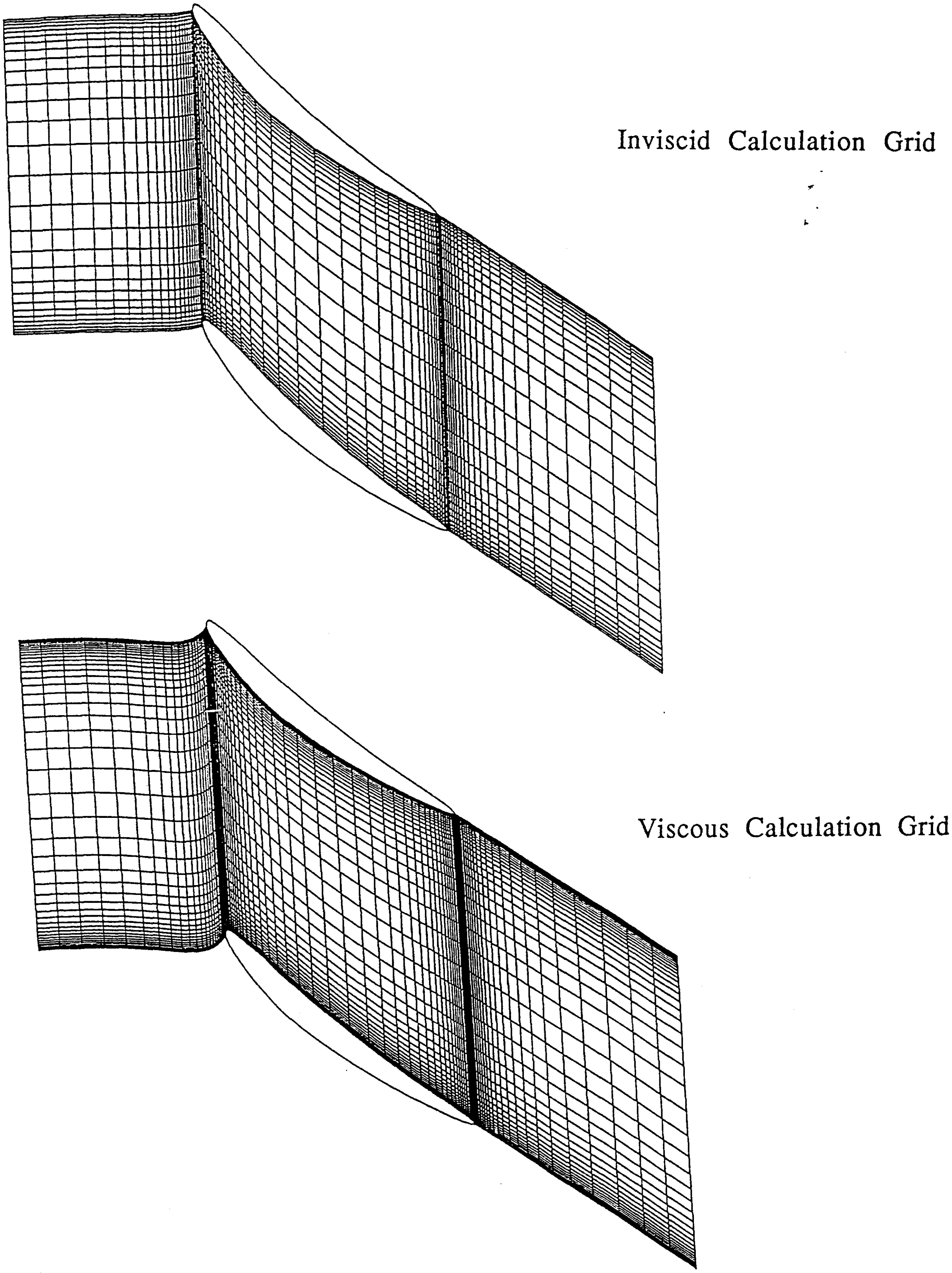

Figure 2.3 Computational Grids at Midspan

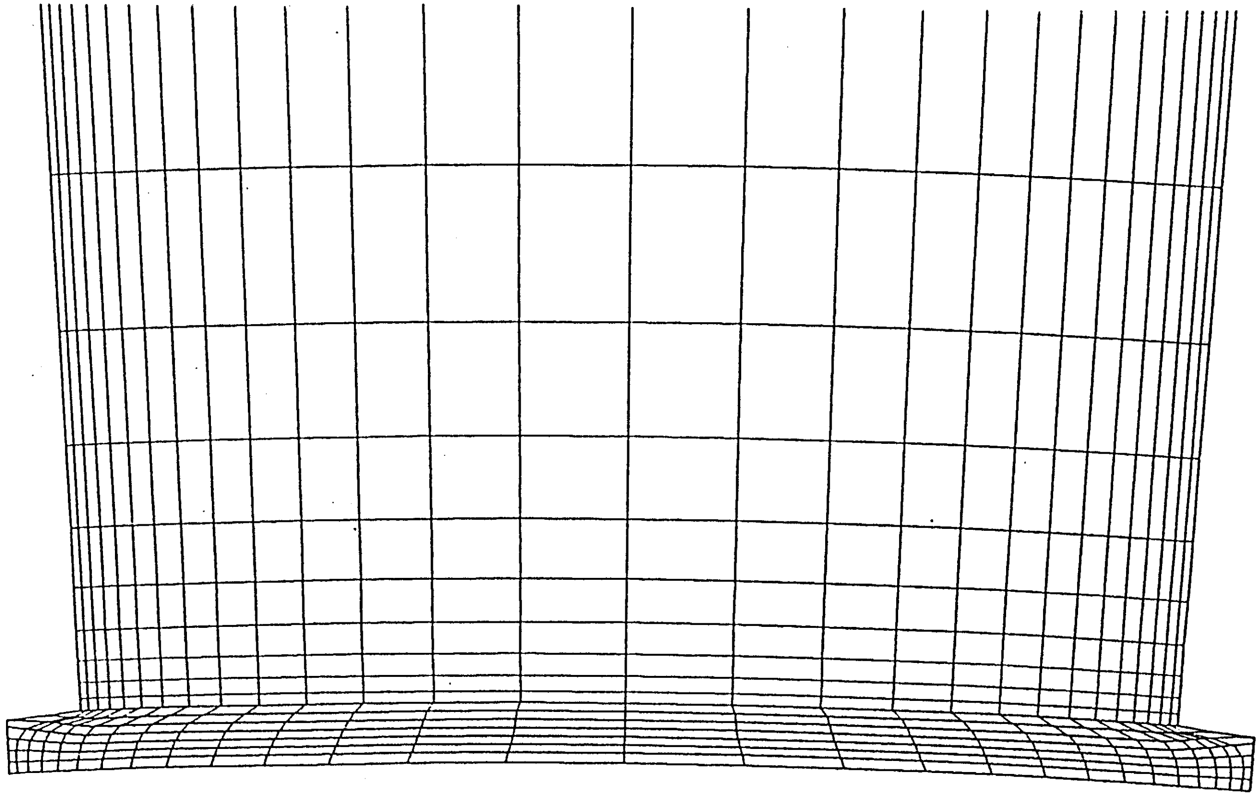

Figure 2.4 Inviscid Computation Grid - Midchord Location

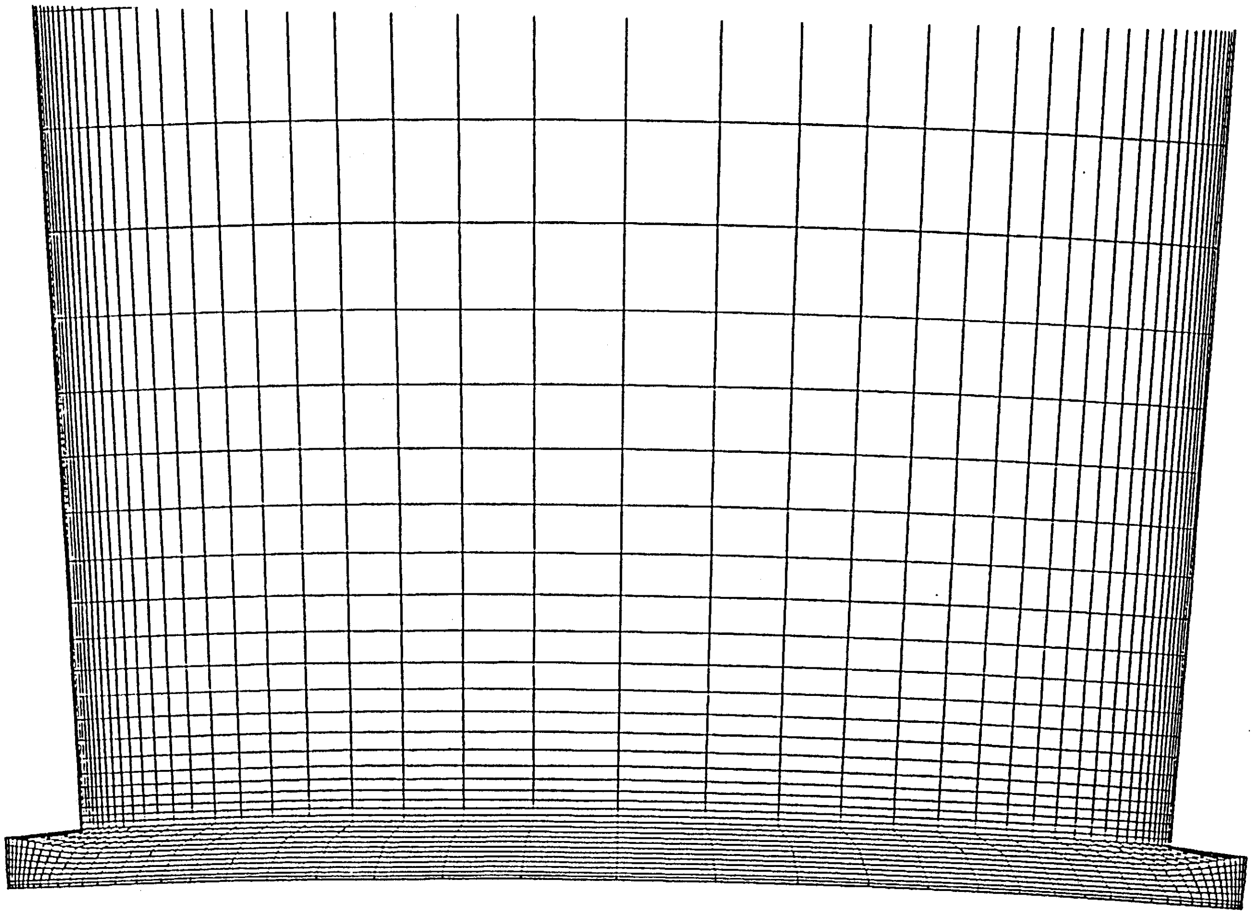

Figure 2.5 Viscous Computation Grid - Midchord Location

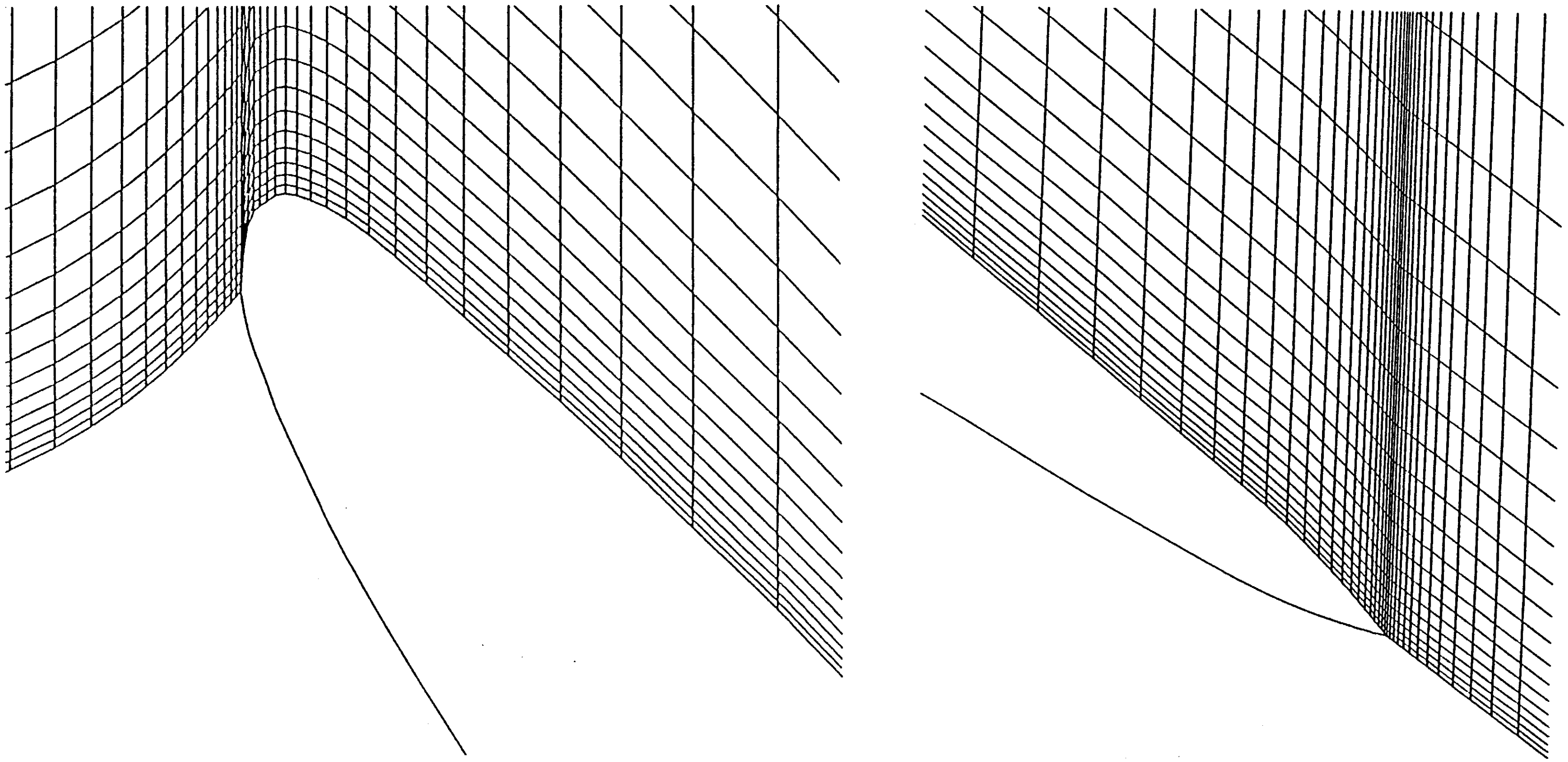

Figure 2.6 Viscous Computation Grid Near L.E. and T.E.

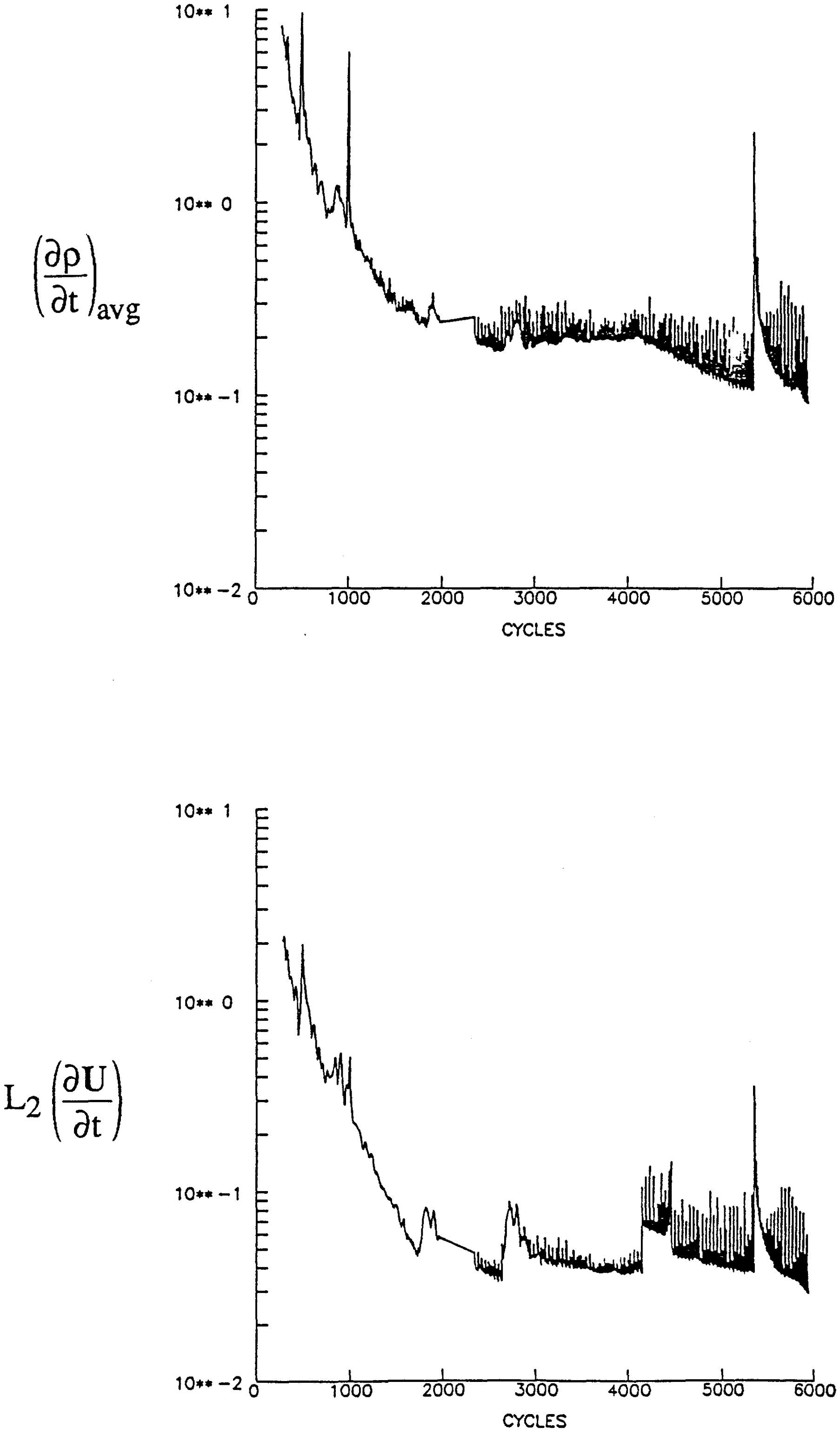

Figure 2.7 Convergence History: Viscous Solution, Hub Clearance, Smooth Moving Hub

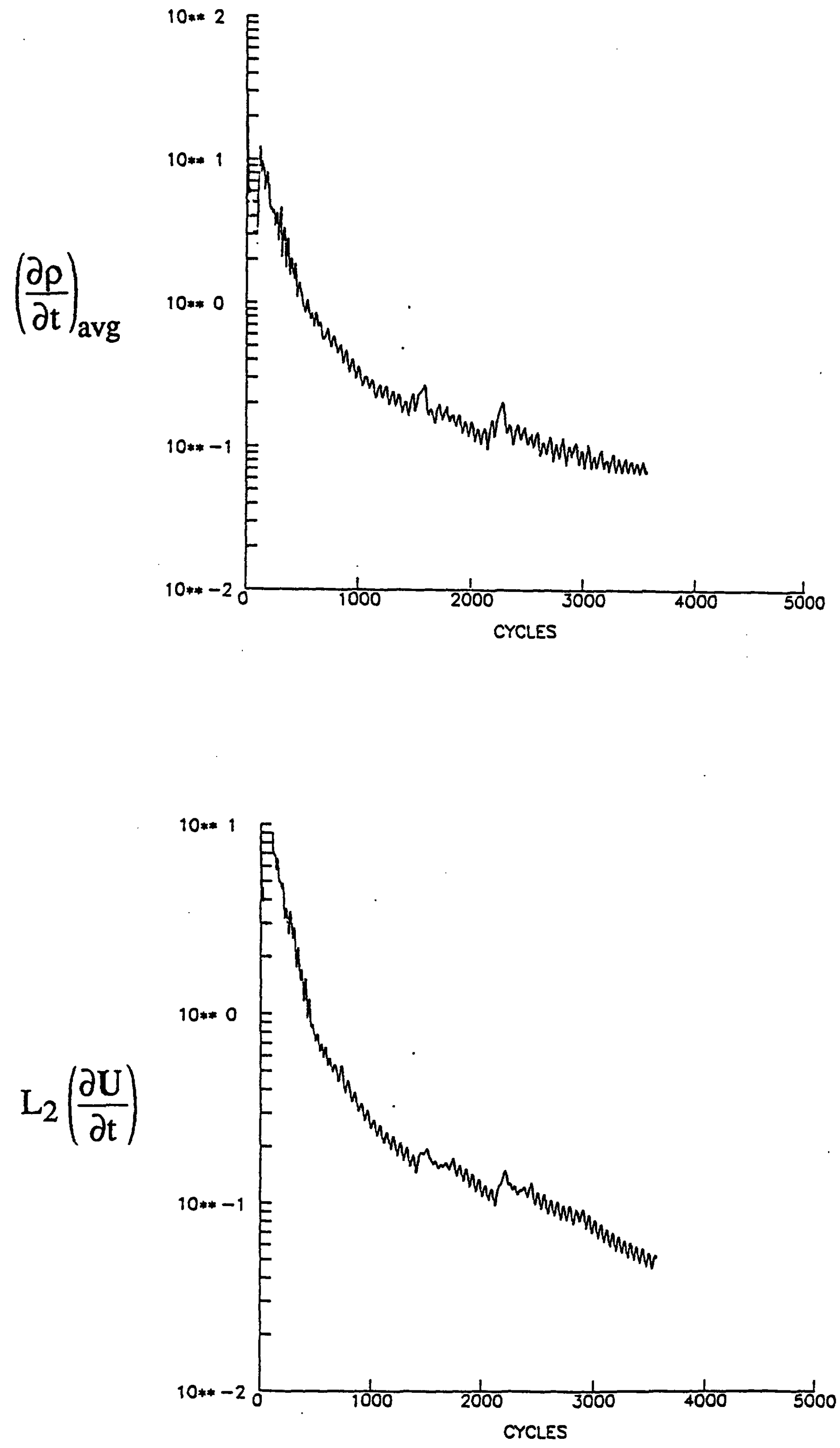

Figure 2.8 Convergence History: Viscous Solution, No Hub Clearance, Both Moving and Nonmoving Hub

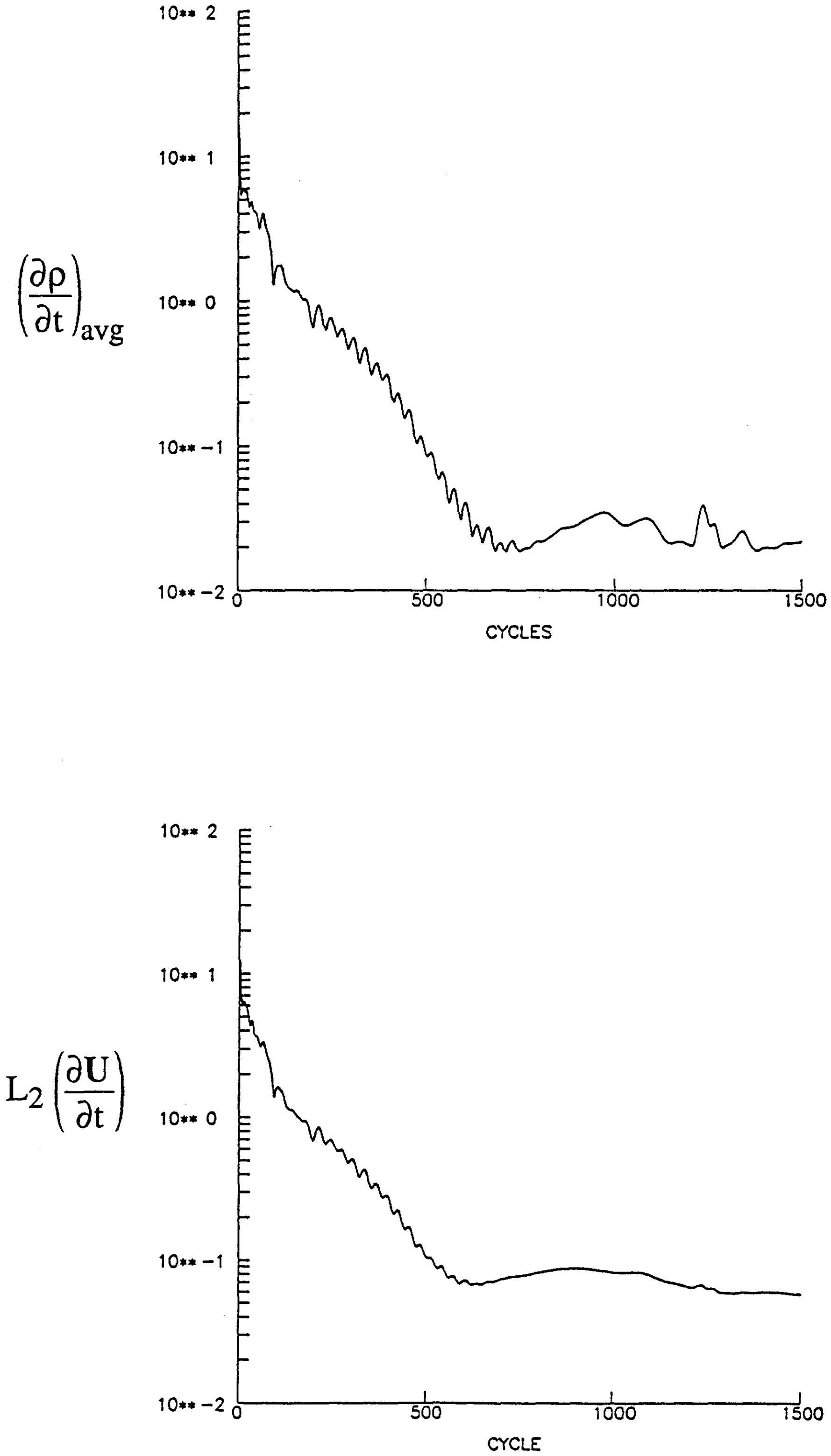

Figure 2.9 Convergence History: Inviscid Solution, Hub Clearance, Smooth Hub

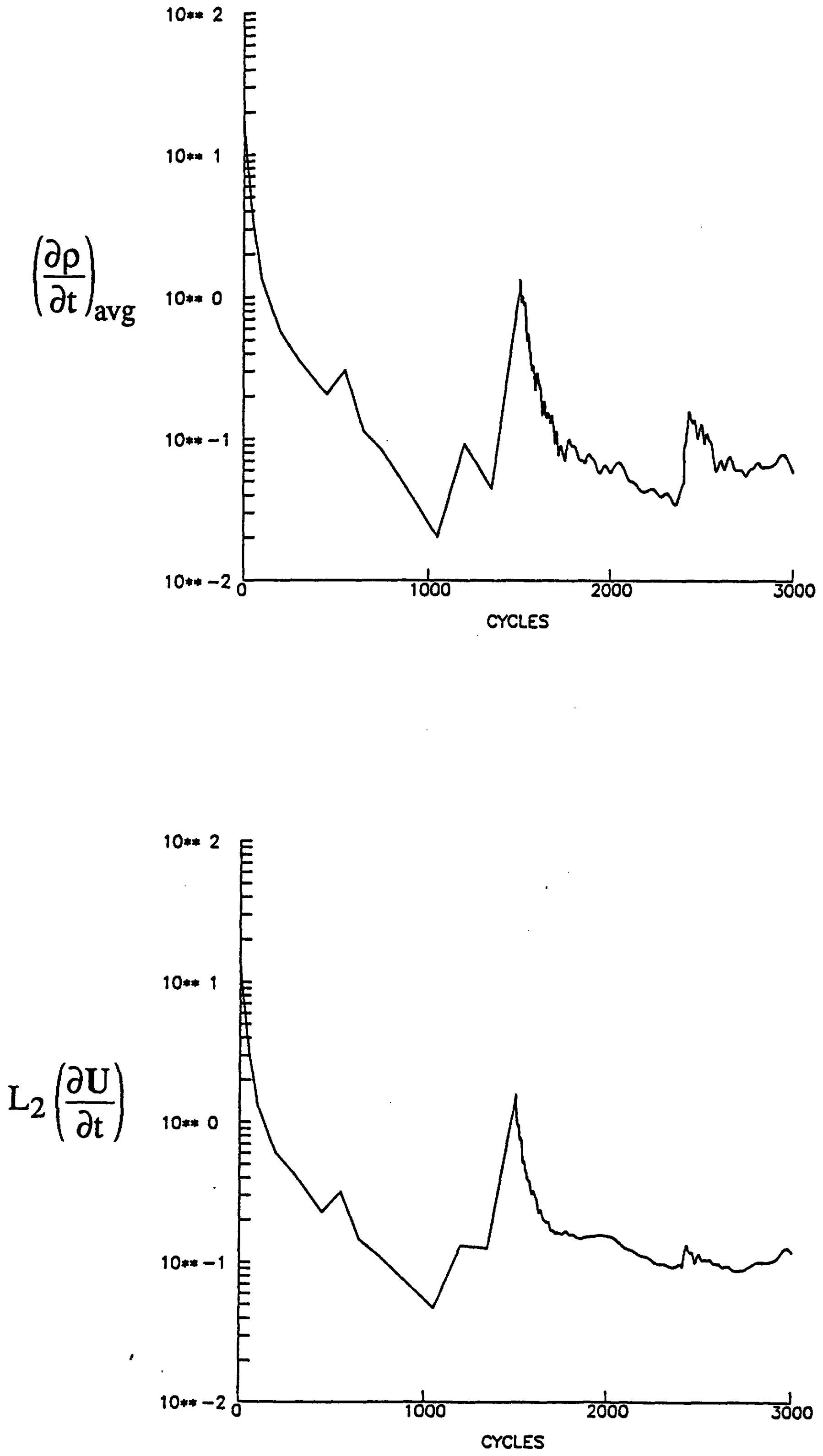

Figure 2.10 Convergence History: Inviscid Solution, Hub Clearance, Hub Treatment

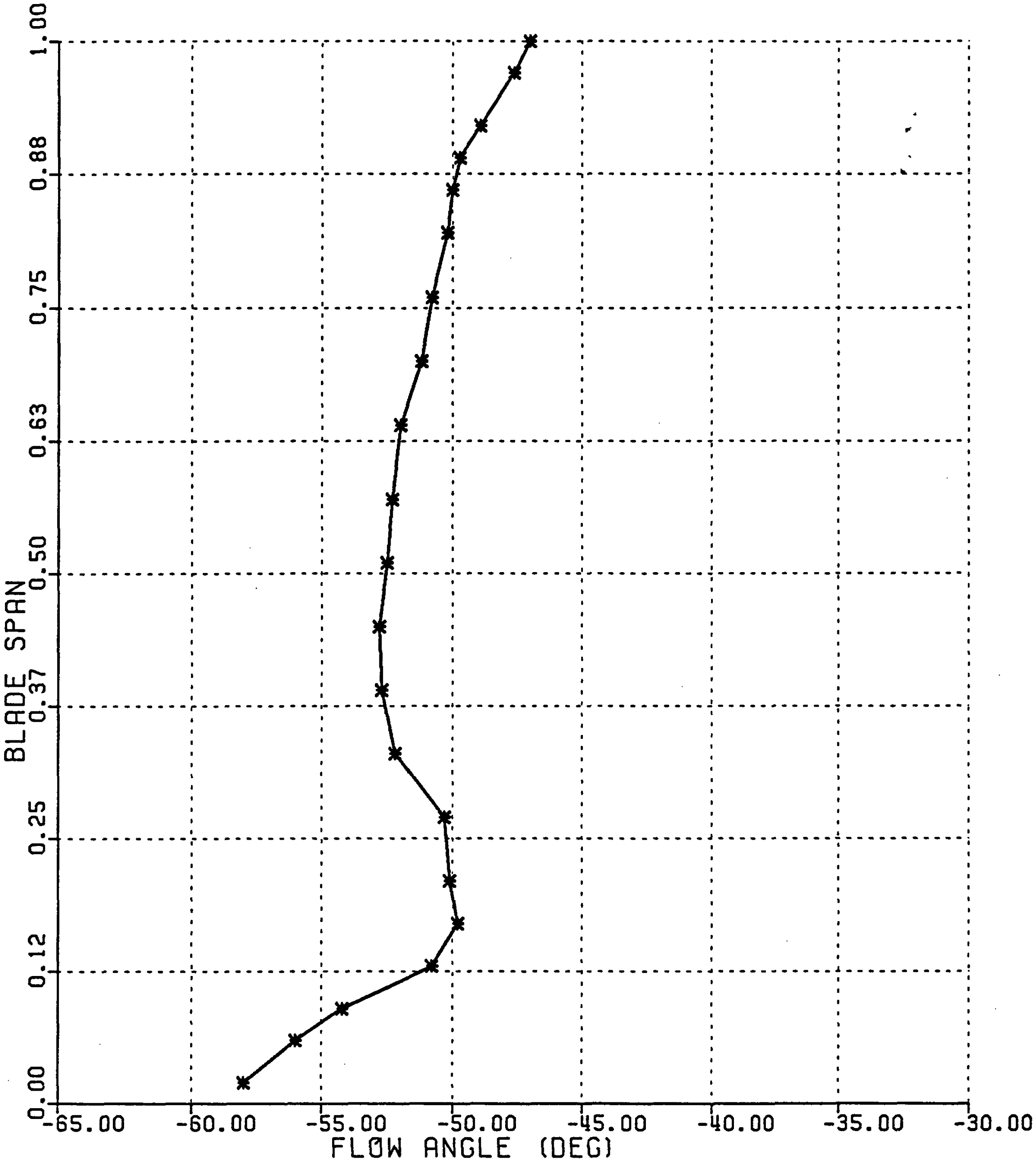

Figure 3.1 Inlet Flow Angles (Experiment)

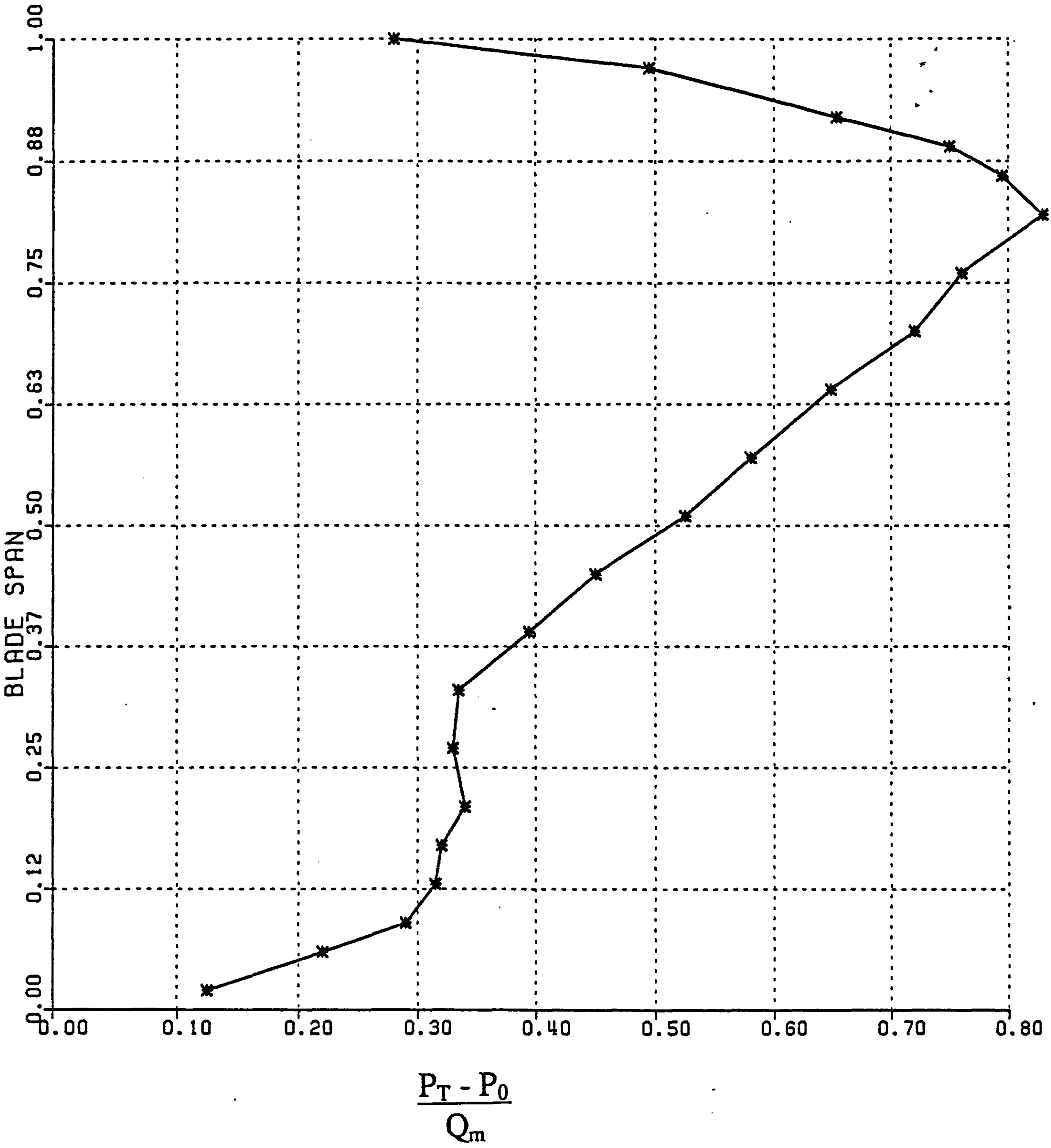

Figure 3.2 Total Pressure Coefficient at Inlet (Experiment)

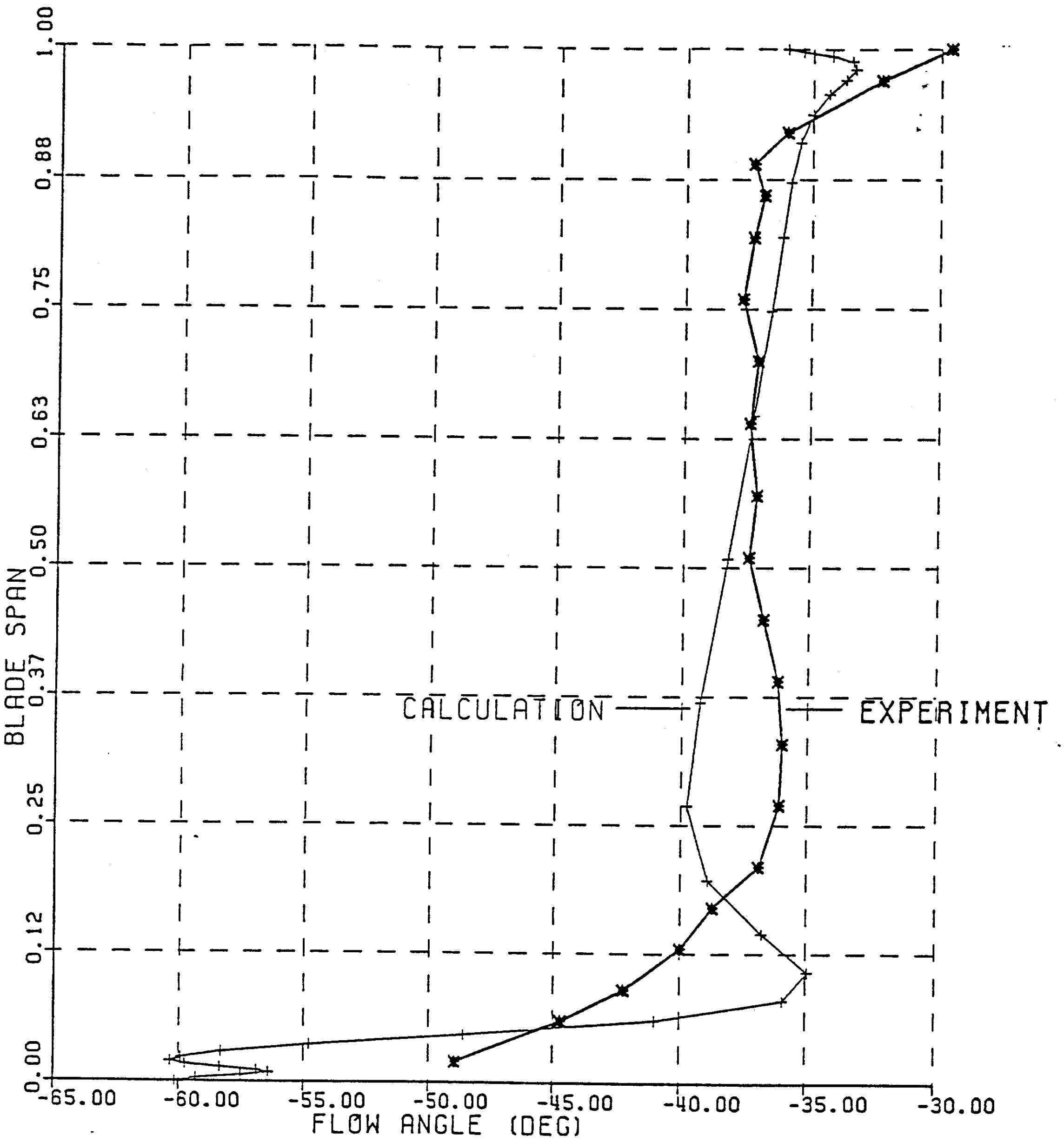

Figure 3.3 Flow Angles Downstream of Stator

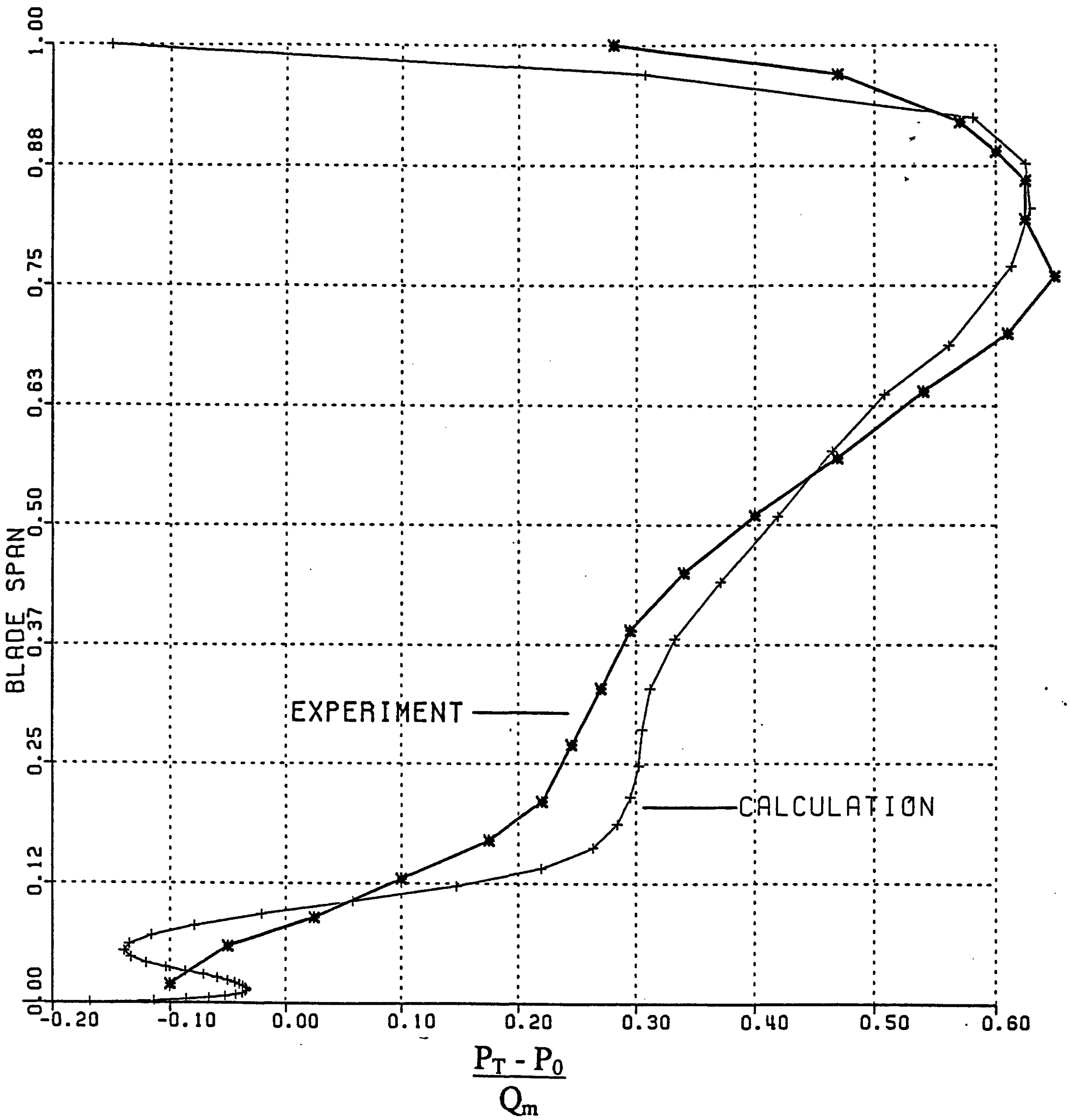

Figure 3.4 Total Pressure Coefficient Downstream of Stator

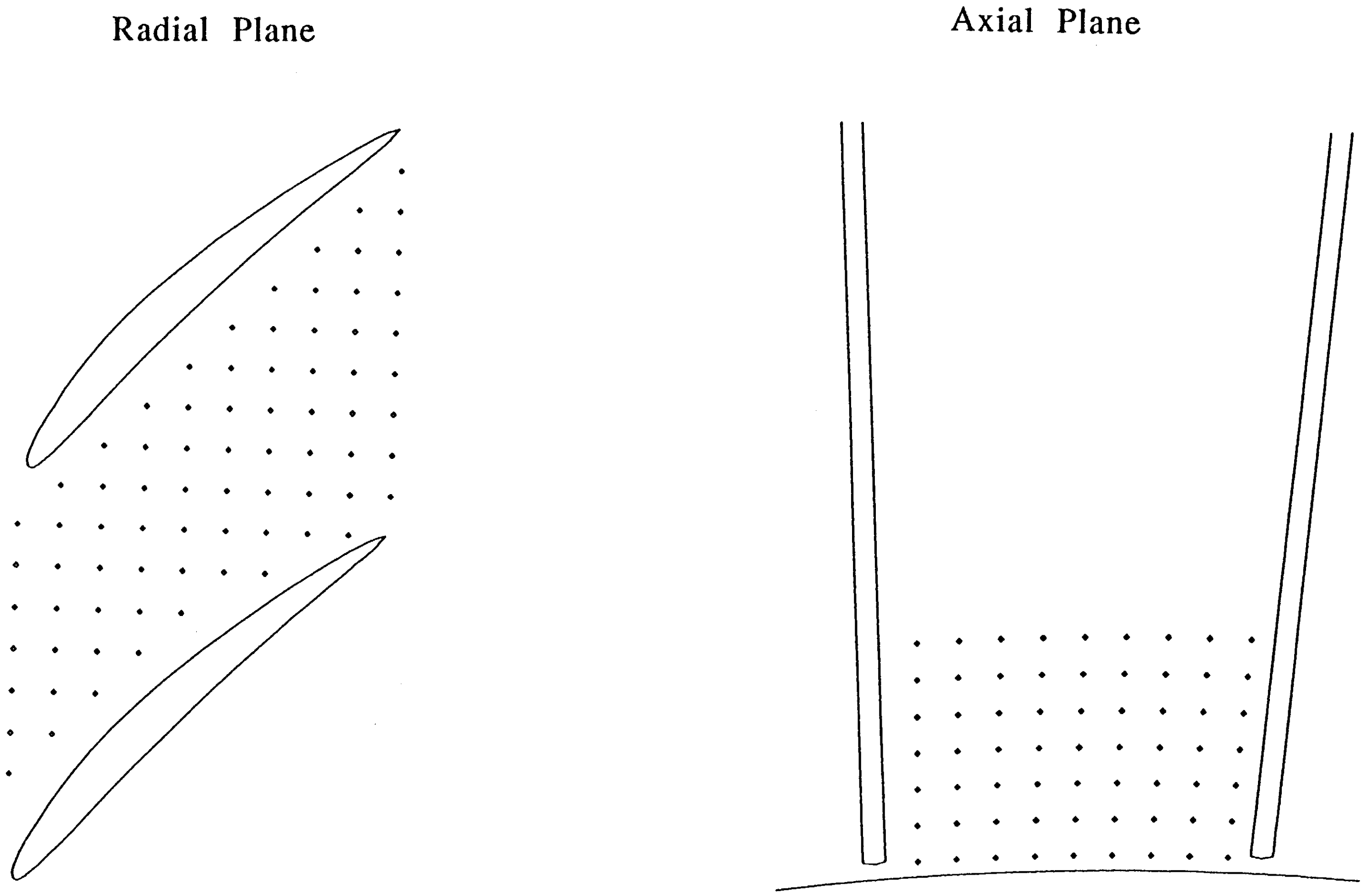

Figure 3.5 Experimental Grid for Velocity Data

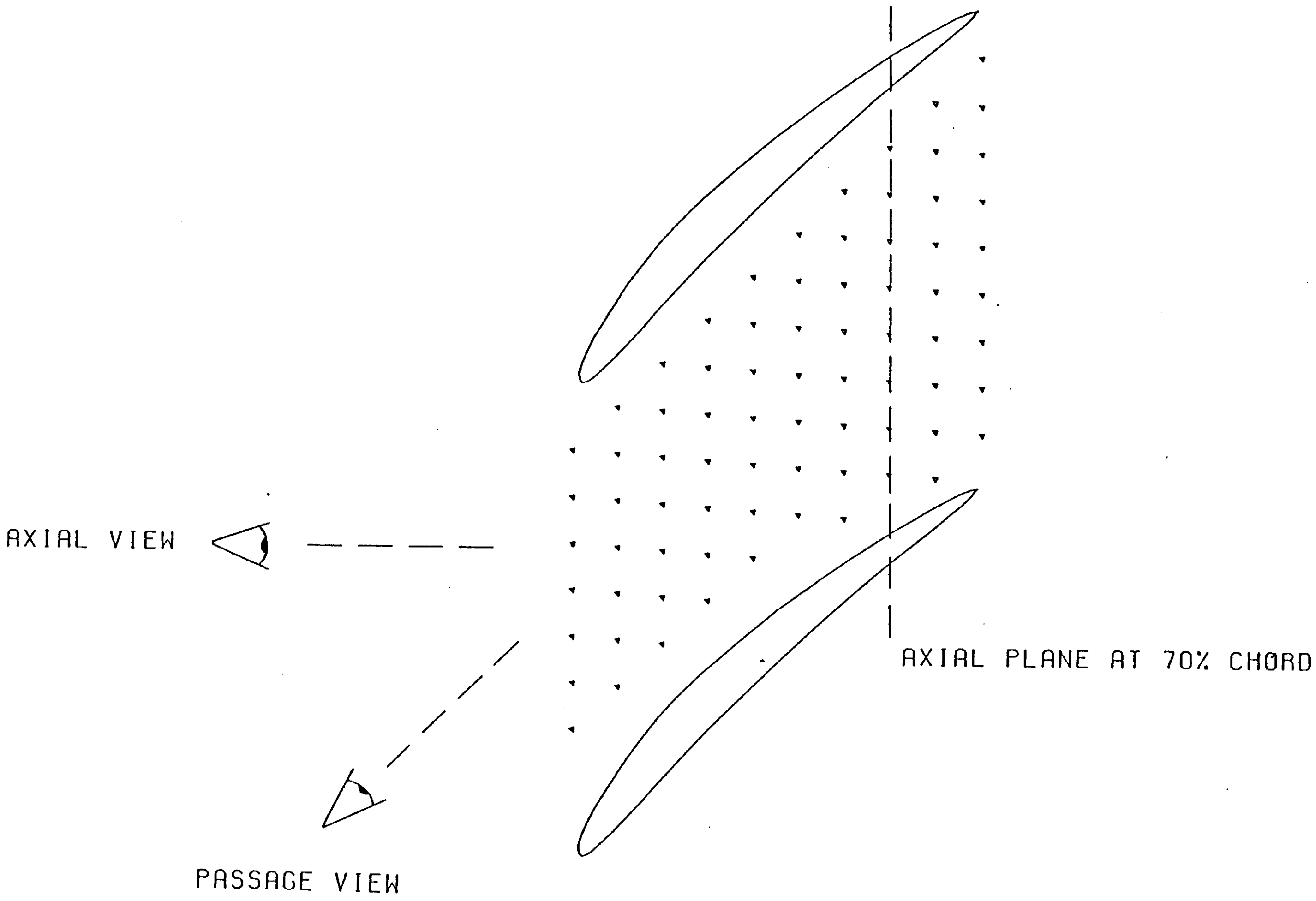

Figure 3.6 Axial Plane and Passage View

Axial View

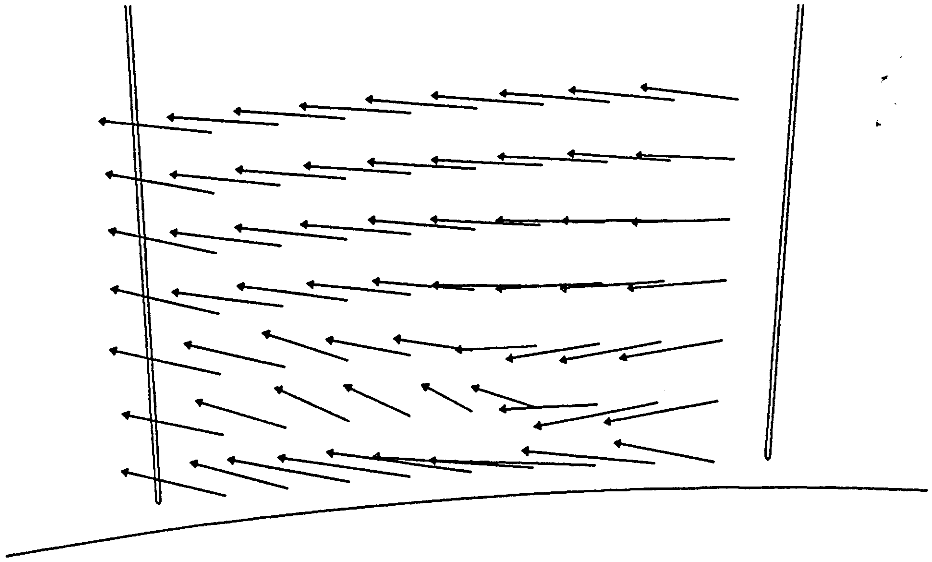

Passage View

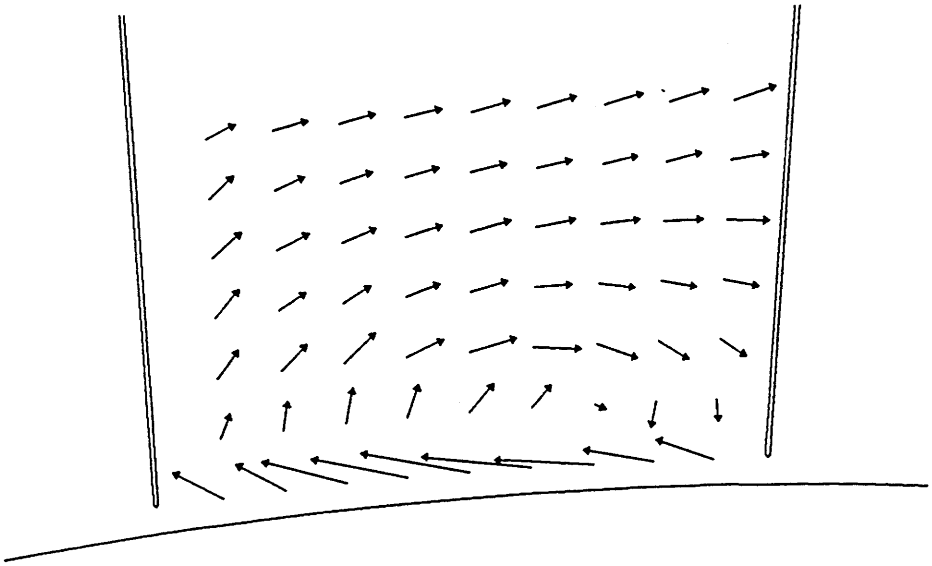

Figure 3.7 Velocity Vectors on Axial Planes at 100% Chord

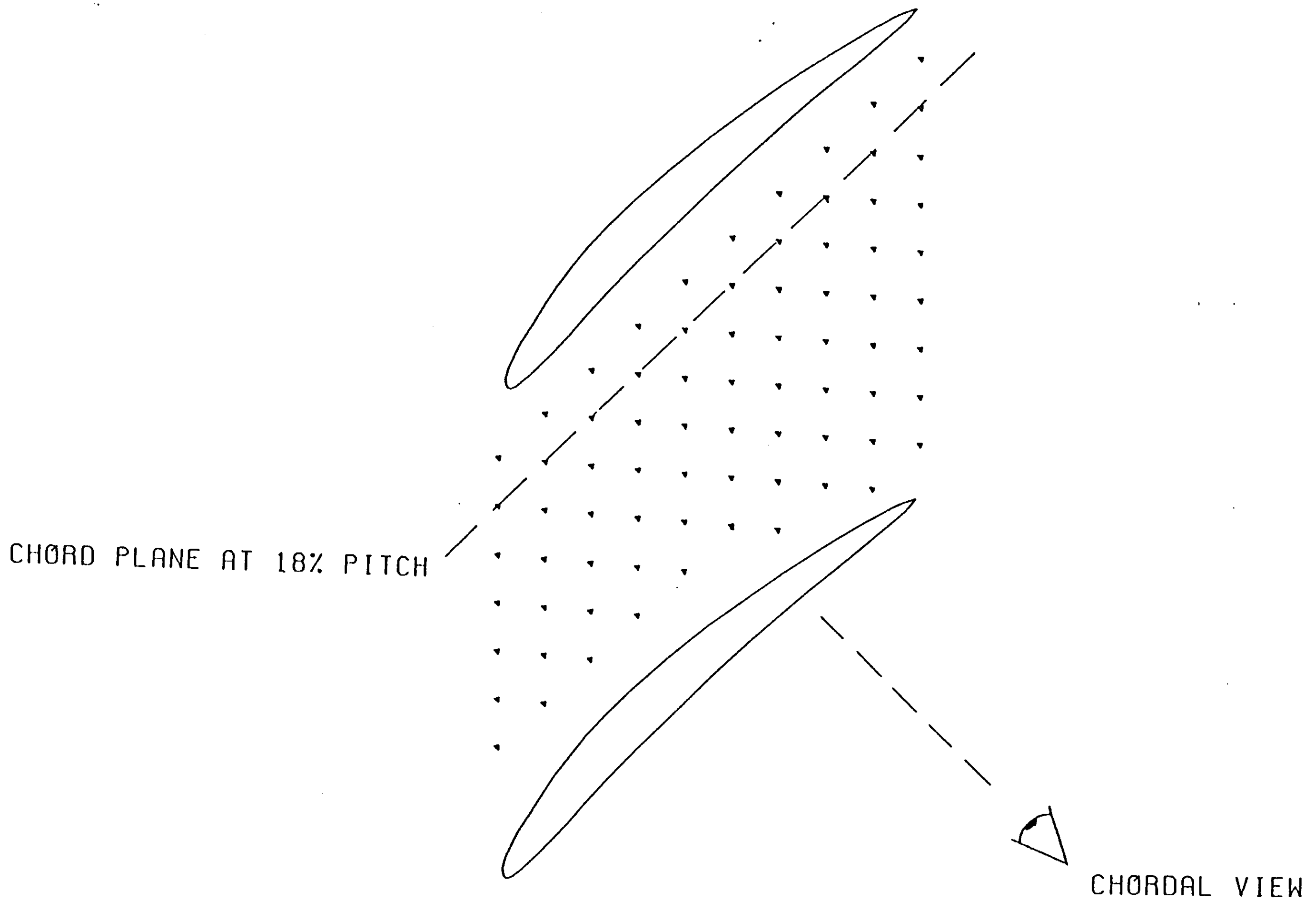

Figure 3.8 Chordal Plane and Chordal View

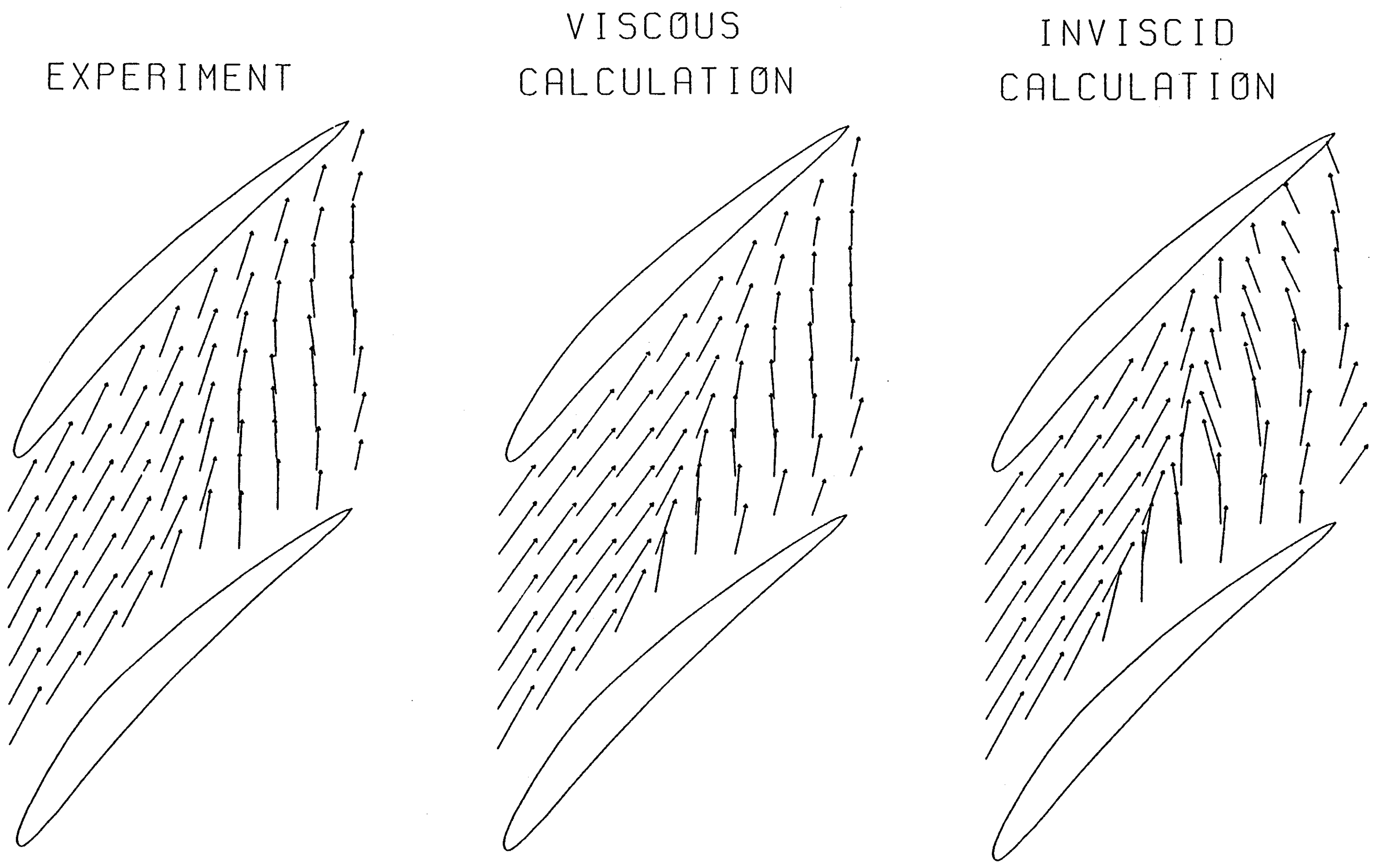

Figure 3.9 Velocity Vectors on Radial Planes at 2% Span

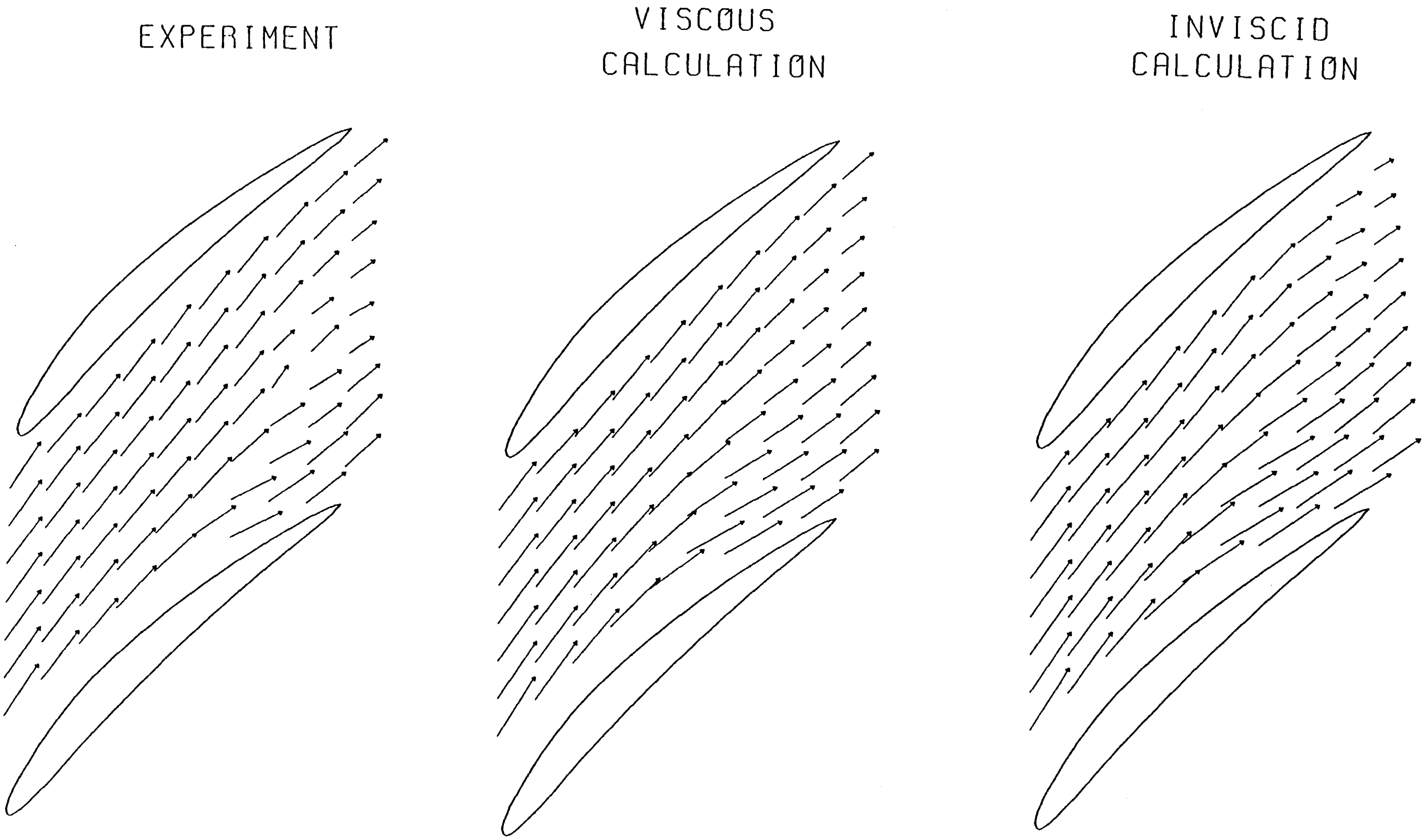

Figure 3.10 Velocity Vectors on Radial Planes at 6% Span

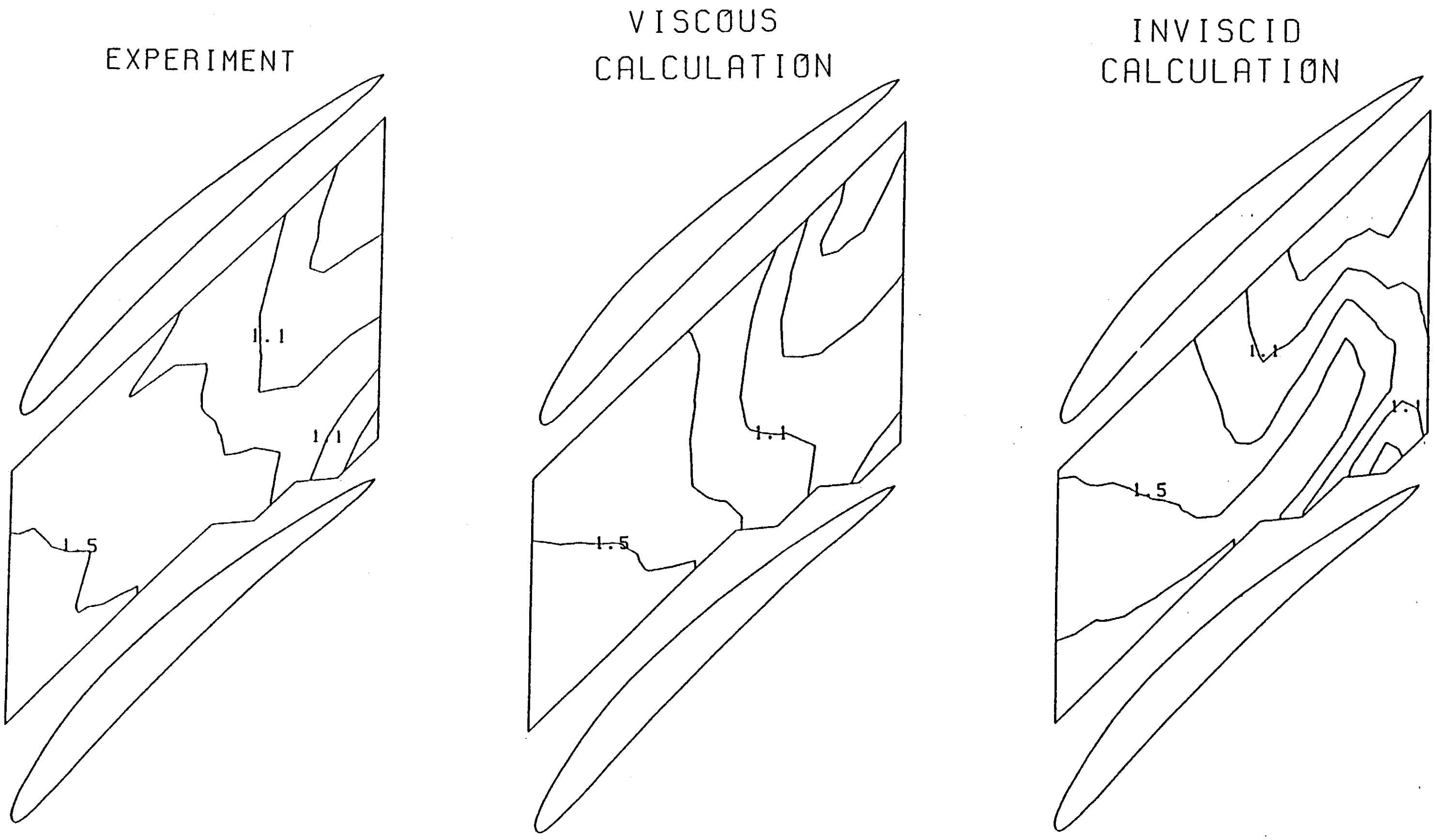

Figure 3.11 Contours of $|\vec{u}|/CX$ at 2% Span

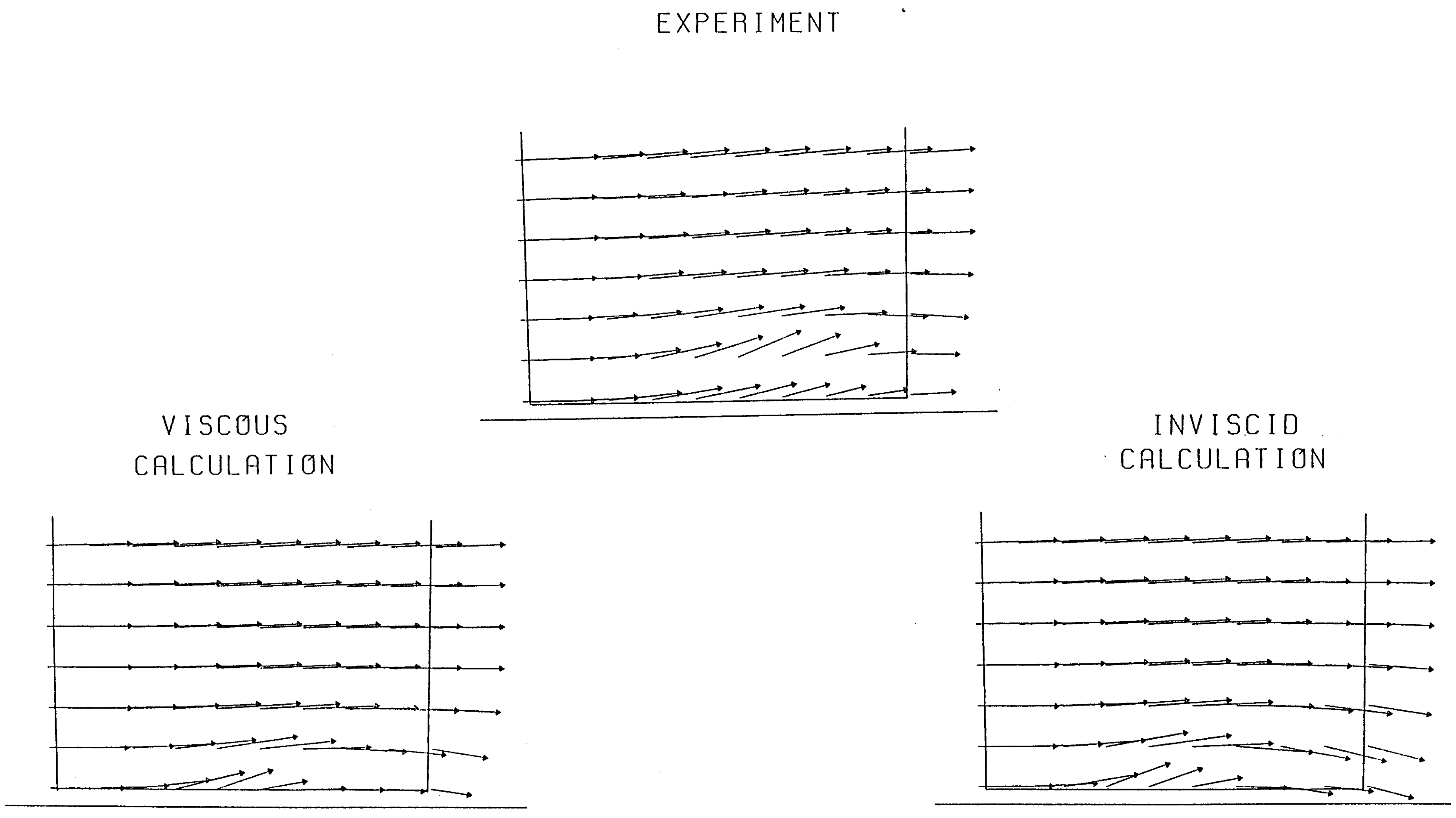

Figure 3.12 Velocity Vectors on Chord Planes at 70% Pitch

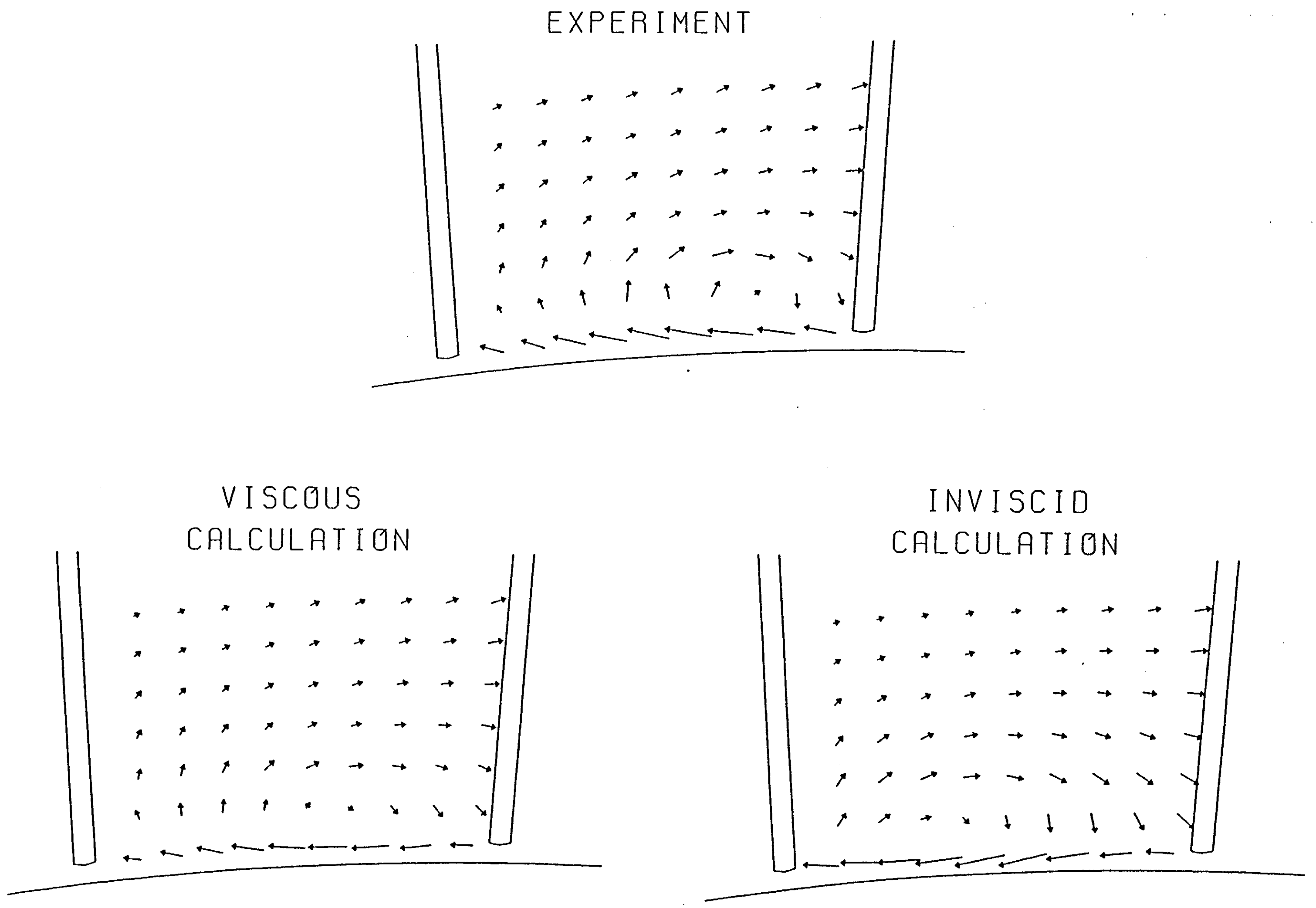

Figure 3.13 Velocity Vectors on Axial Planes at 90% Chord

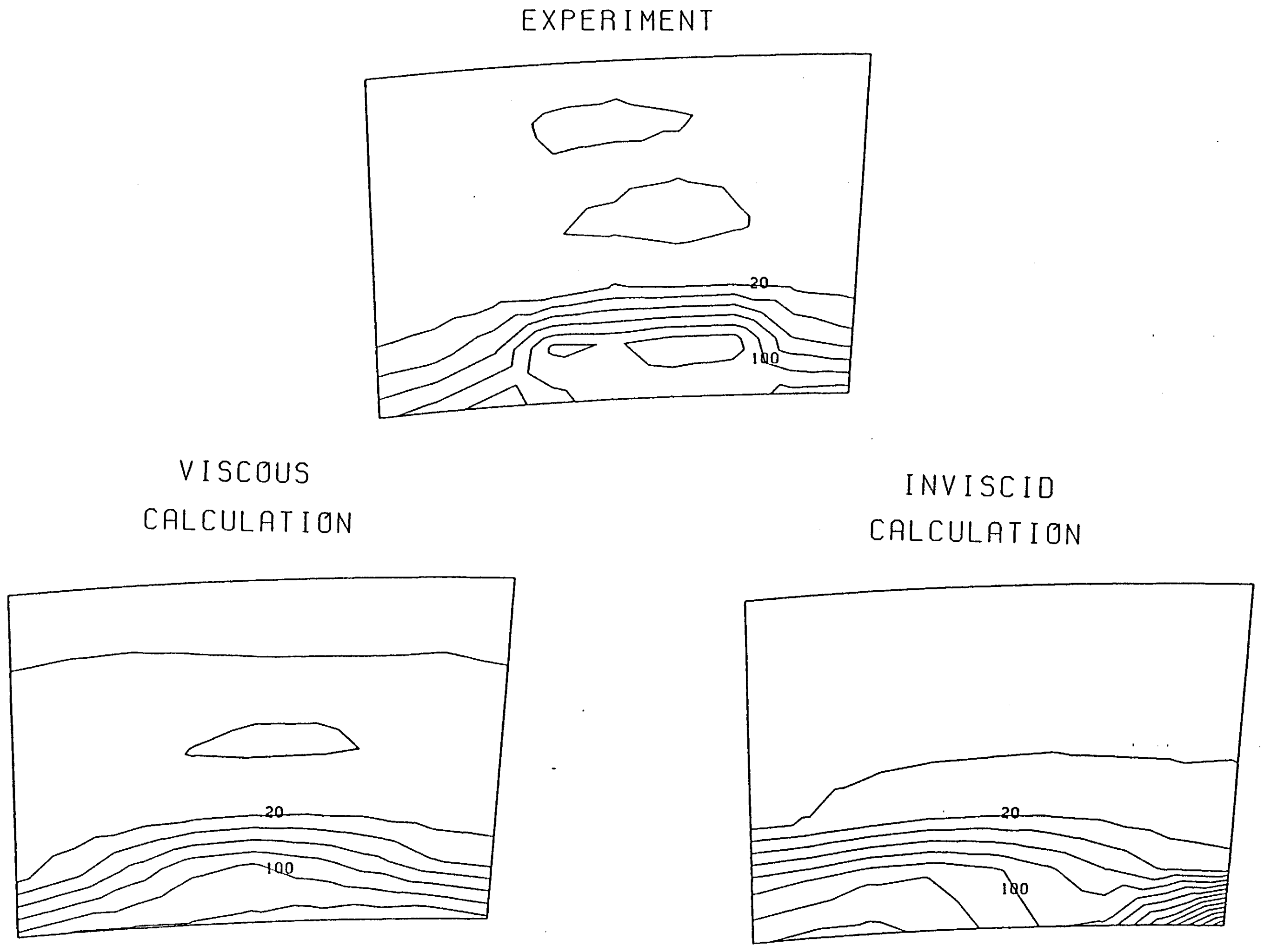

Figure 3.14 Contours of Vorticity at 90% Chord

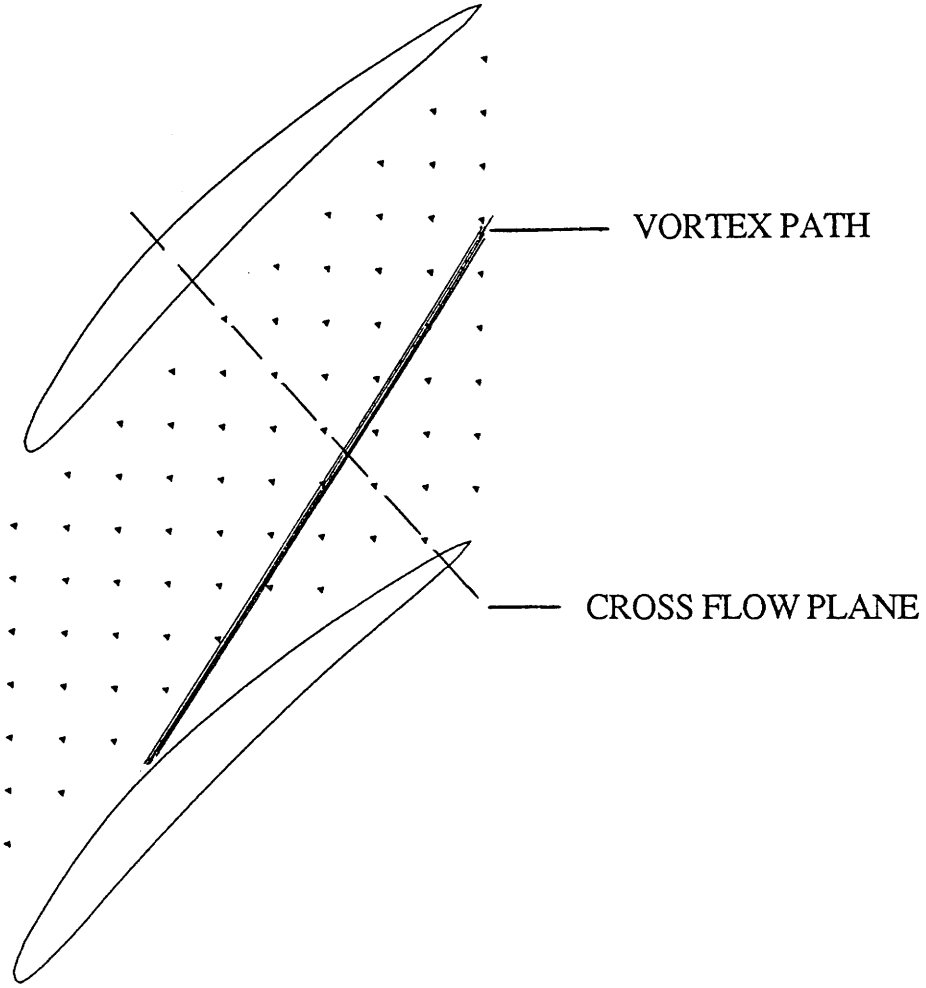

Figure 3.15 Cross Flow Plane

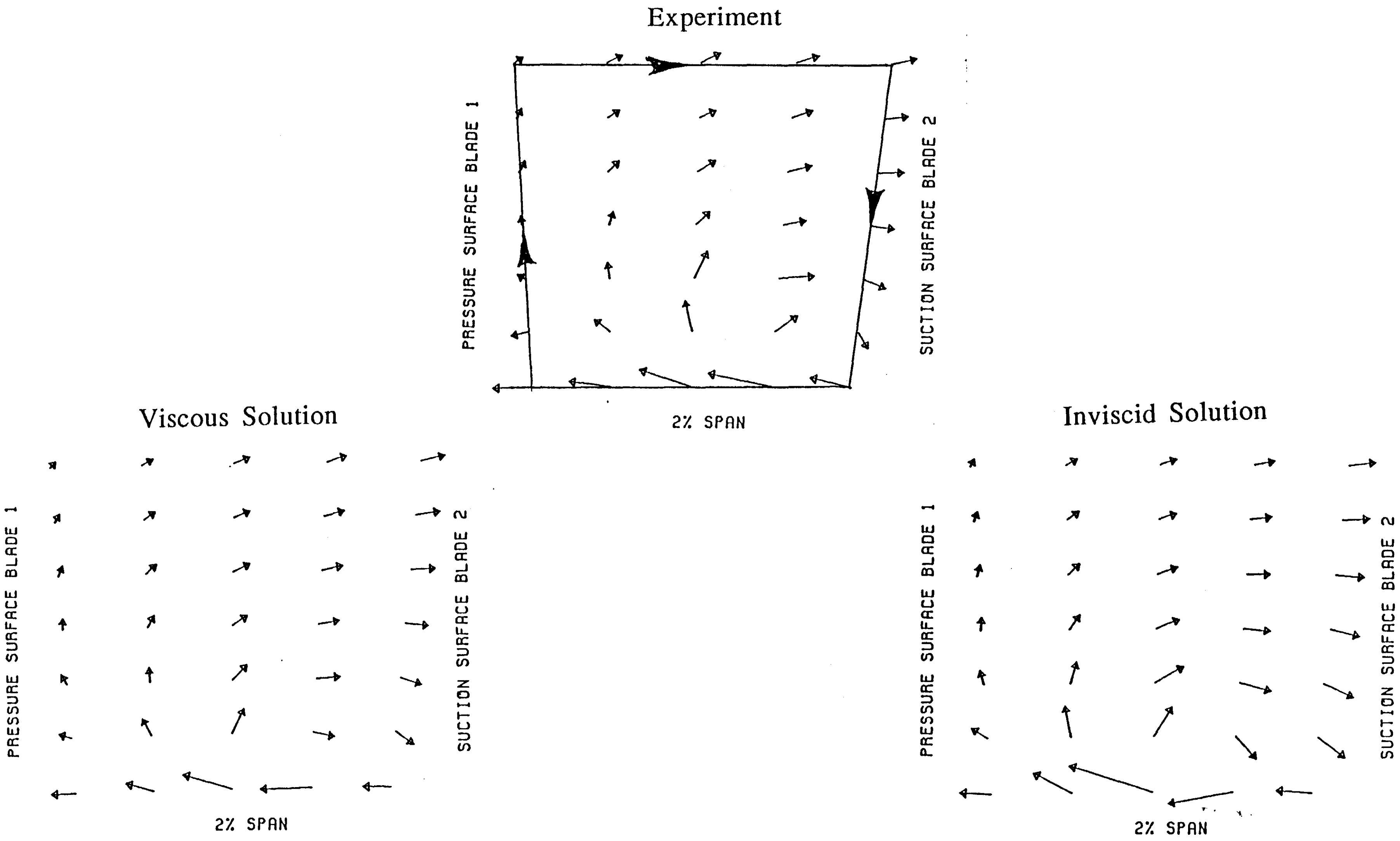

Figure 3.16 Velocity Vectors on Cross Flow Planes

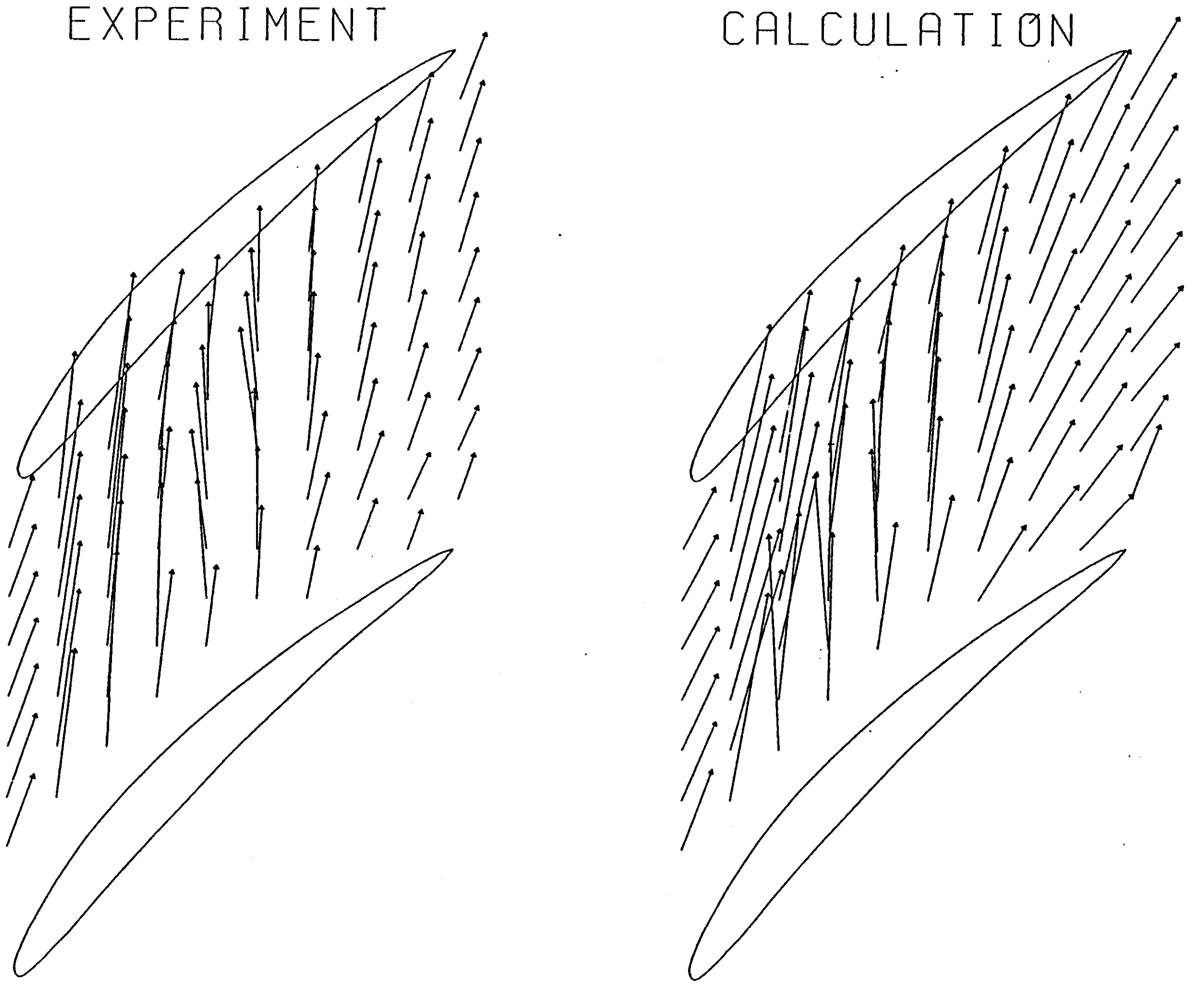

Figure 3.17 Hub Treatment Velocity Vectors on Radial Planes at 2% Span

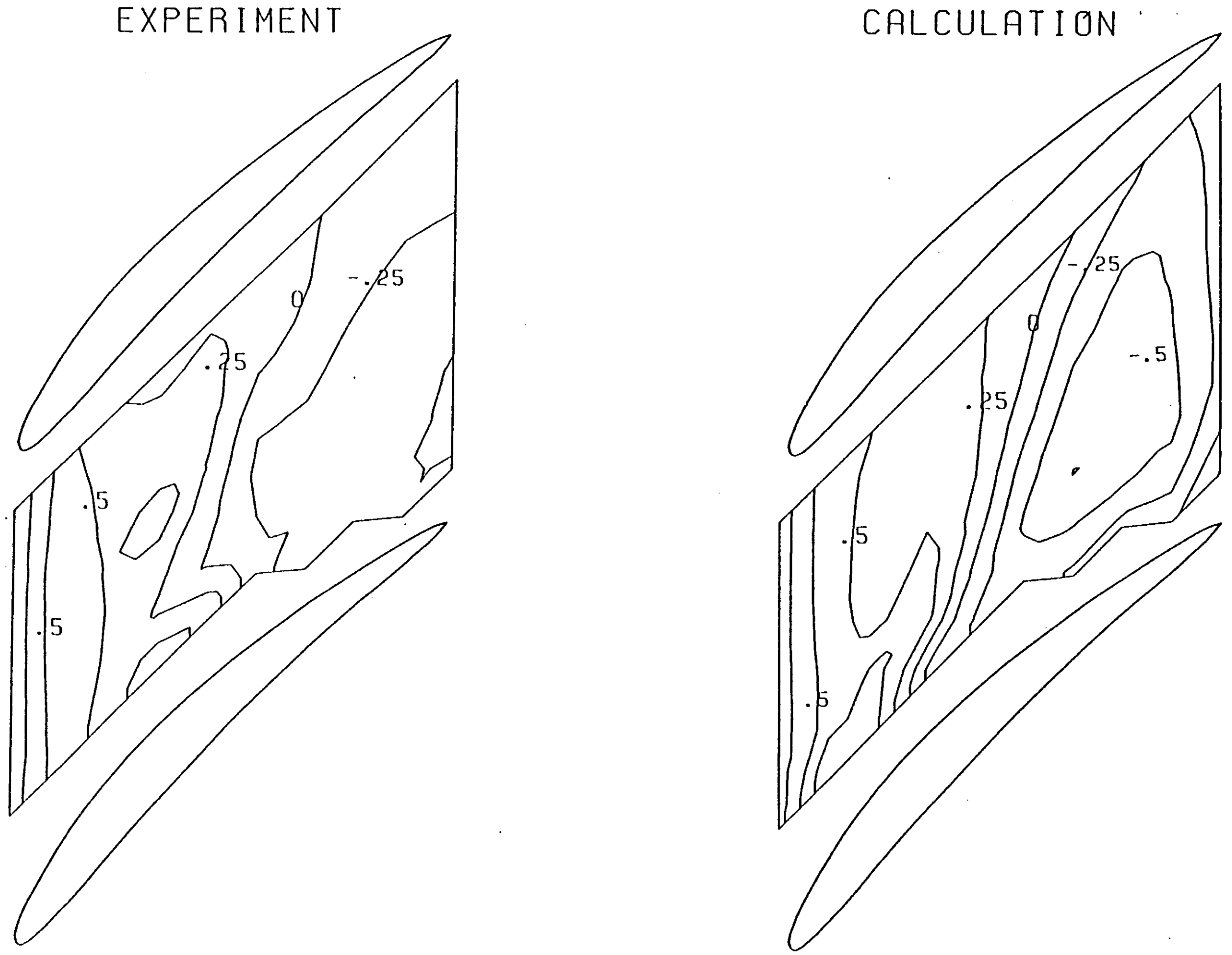

Figure 3.18 Contours of v/CX at 2% Span

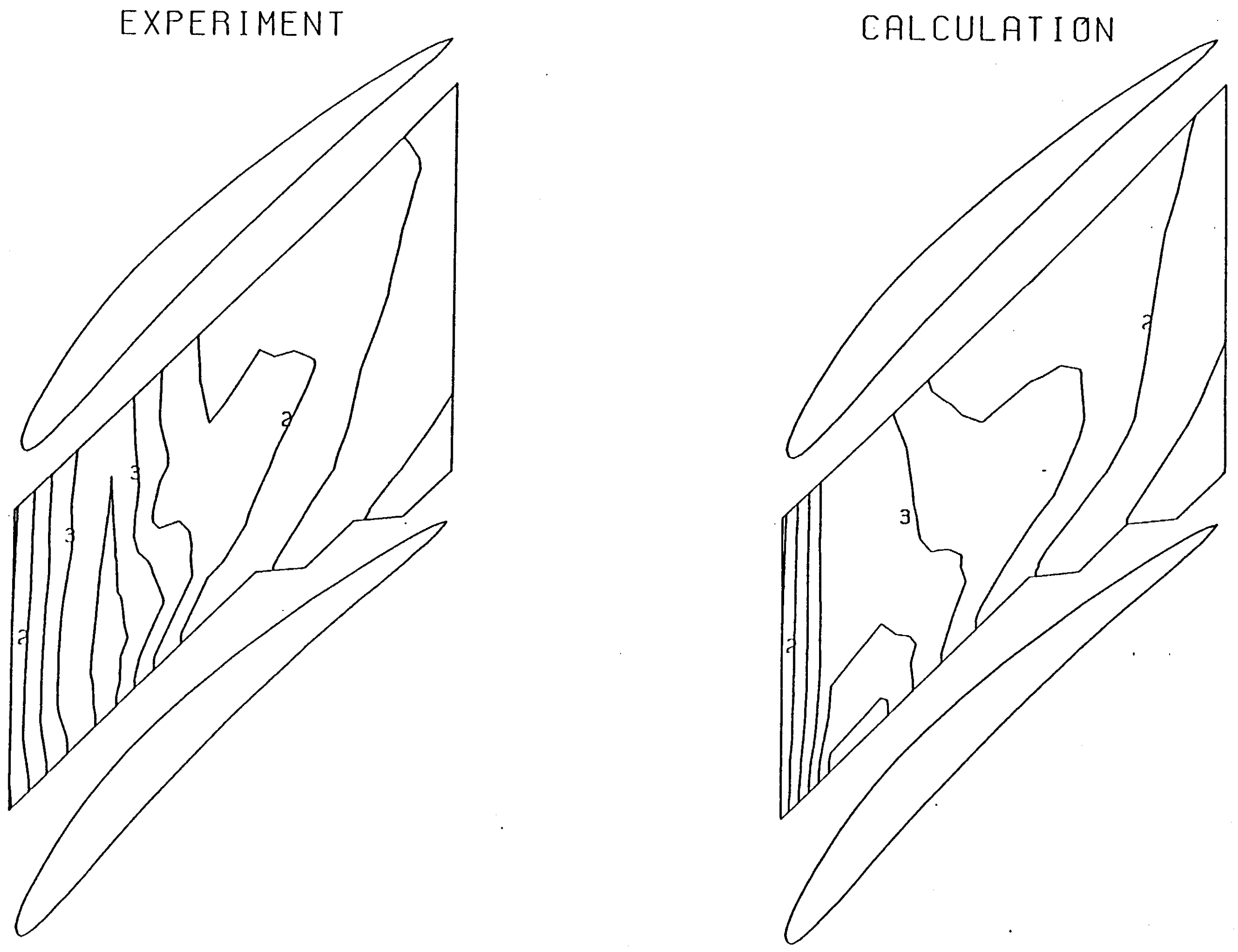

Figure 3.19 Contours of $|\vec{u}|/CX$ at 2% Span

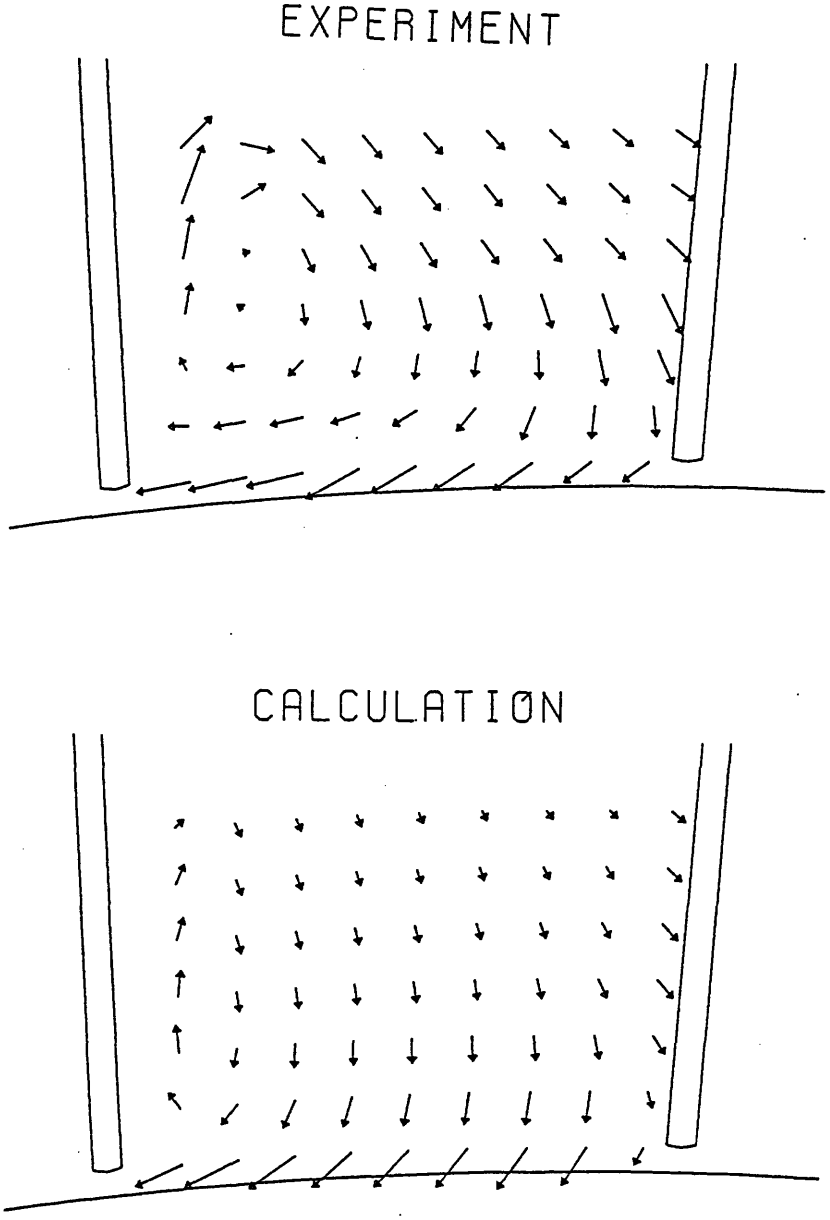

Figure 3.20 Velocity Vectors on Axial Planes at 90% Chord

Experiment

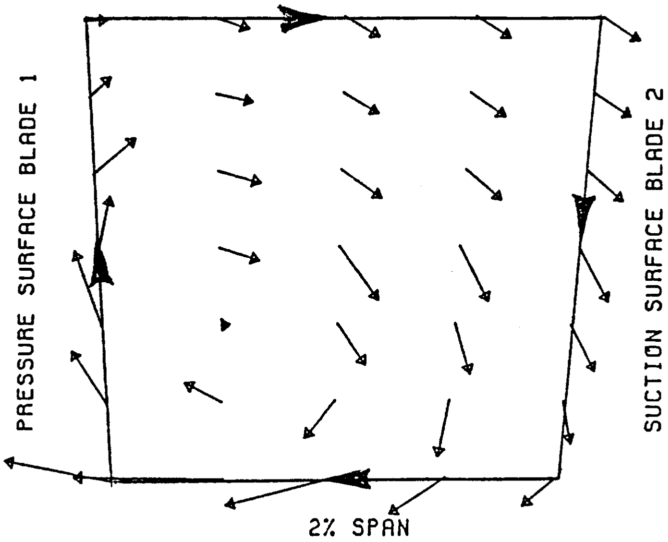

Inviscid Solution

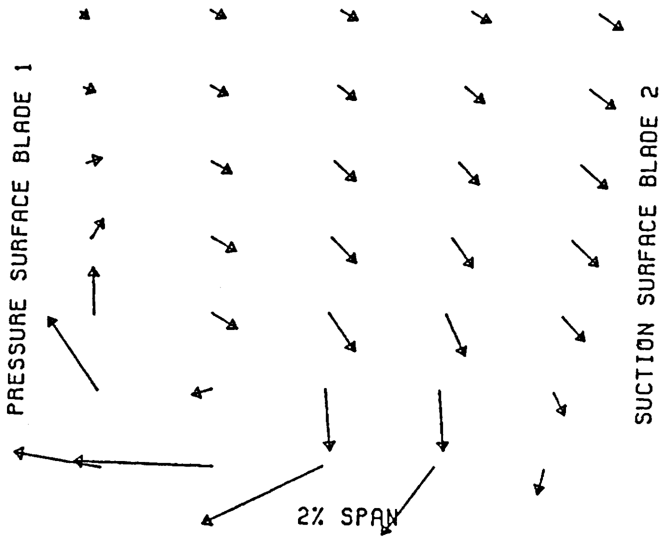

Figure 3.21 Velocity Vectors on Cross Flow Planes

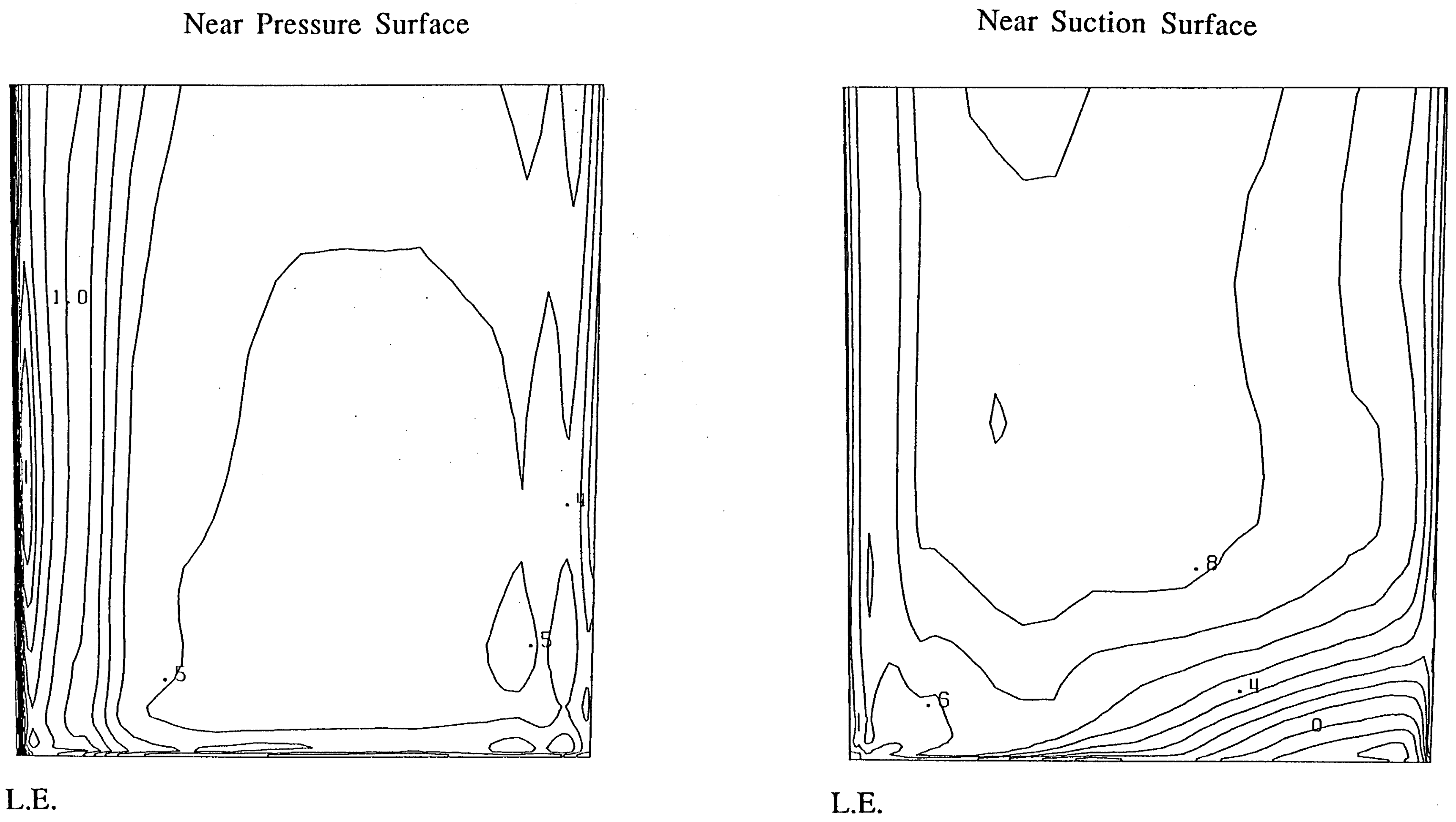

Figure 4.1 No Hub Clearance/Stationary Hub: u/CX Near Blade Surfaces

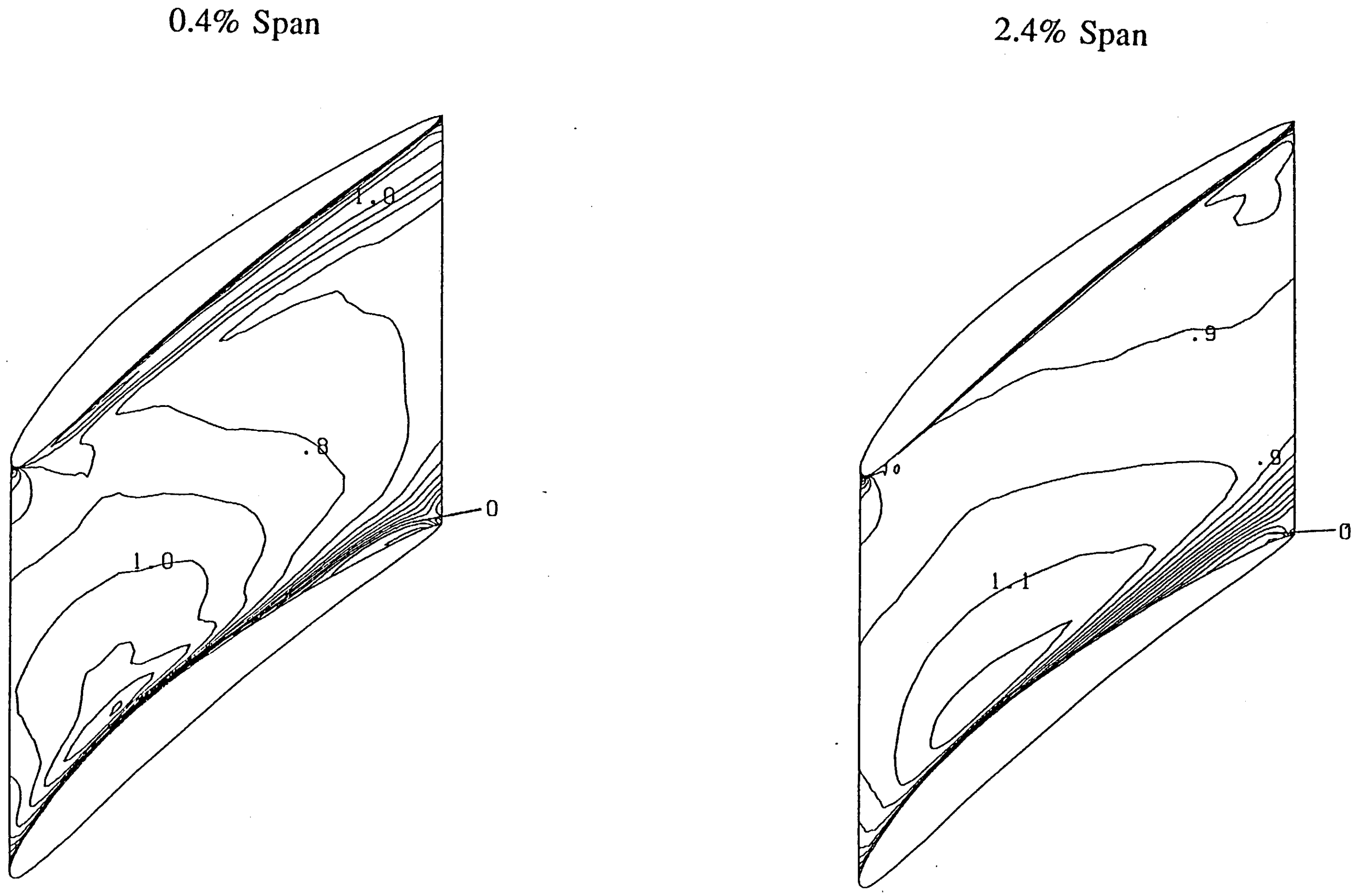

0.4% Span

2.4% Span

Figure 4.2 No Clearance/Stationary Hub: u/CX at Radial Planes

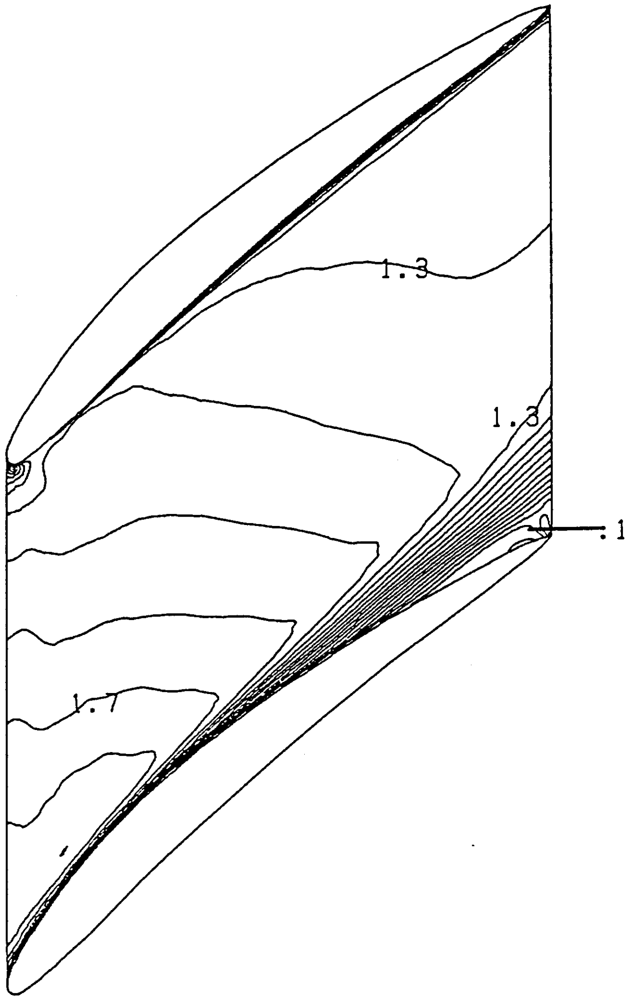

Figure 4.3 No Clearance/Stationary Hub: $|\rho\vec{u}|/\rho CX$ at 2.4% Span

36% Chord

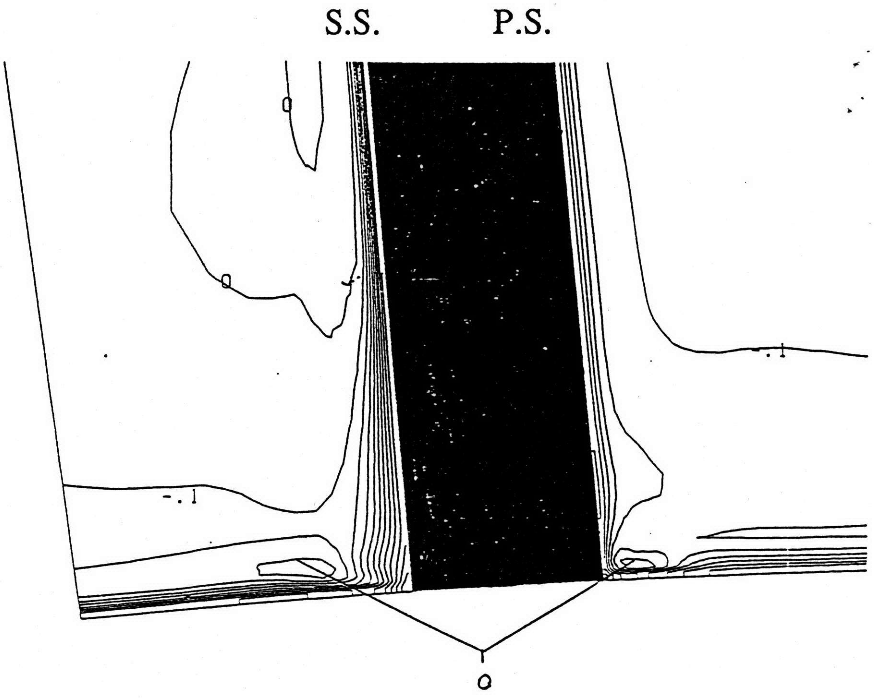

50% Chord

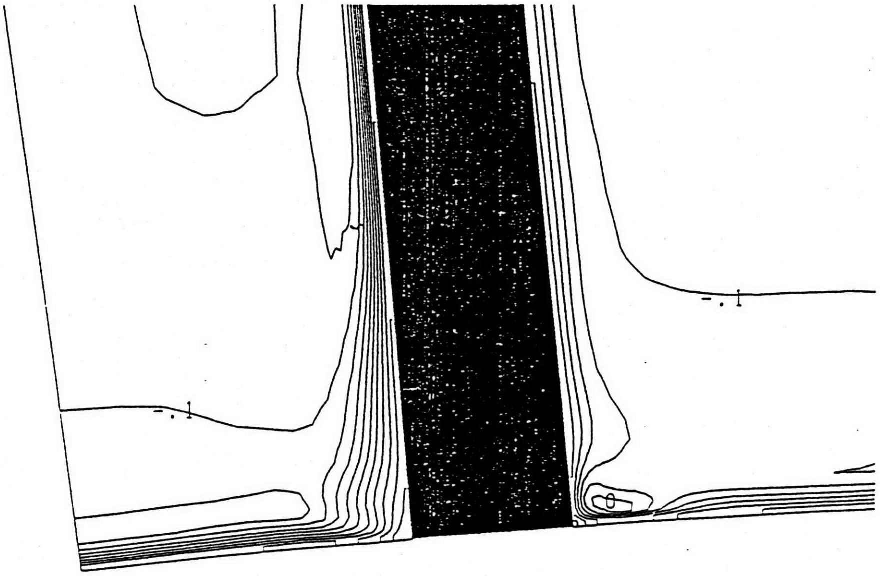

Figure 4.4 No Clearance/Stationary Hub: $(P_T\text{-}P_{T_{in}})/Q_{in}$ at Axial Planes

65% Chord

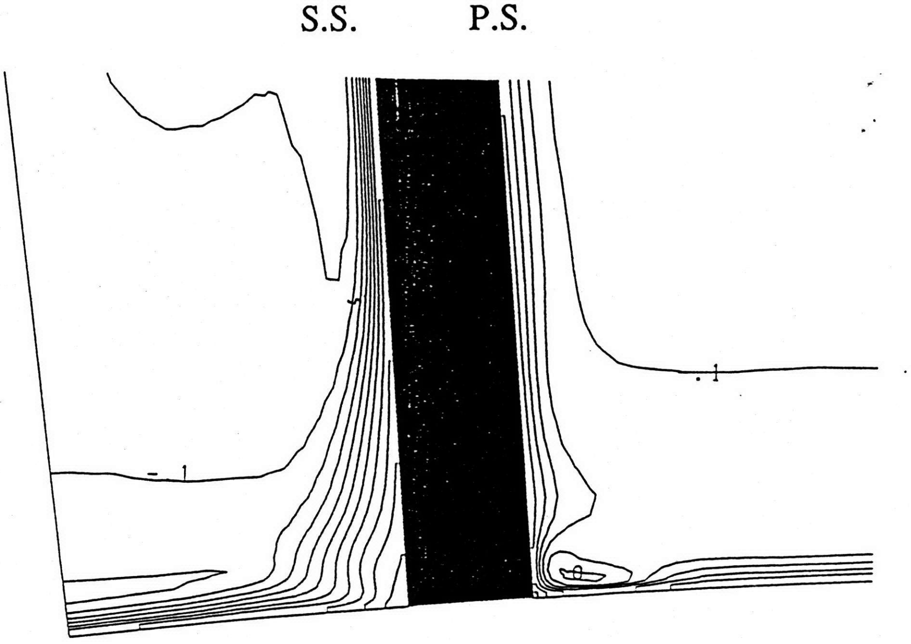

79% Chord

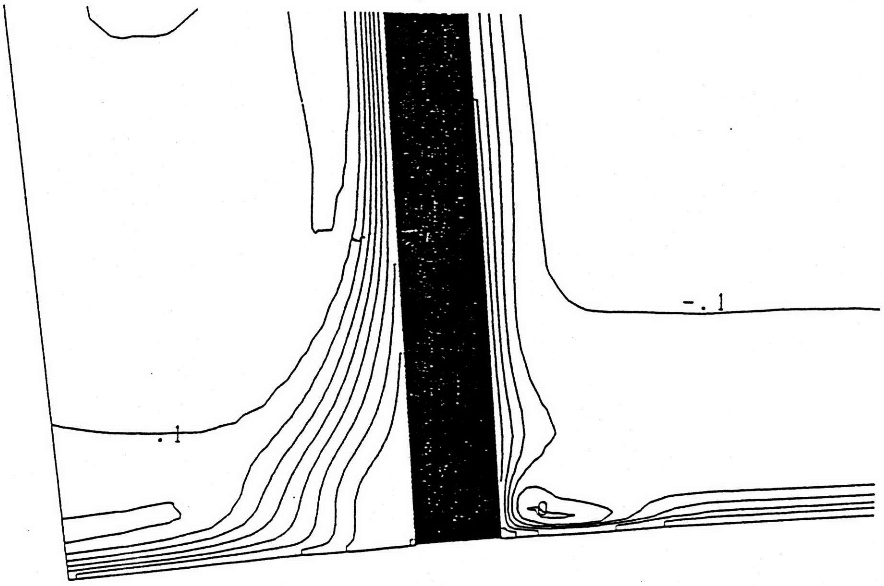

Figure 4.5 No Clearance/Stationary Hub: $(P_T-P_{Tin})/Q_{in}$ at Axial Planes

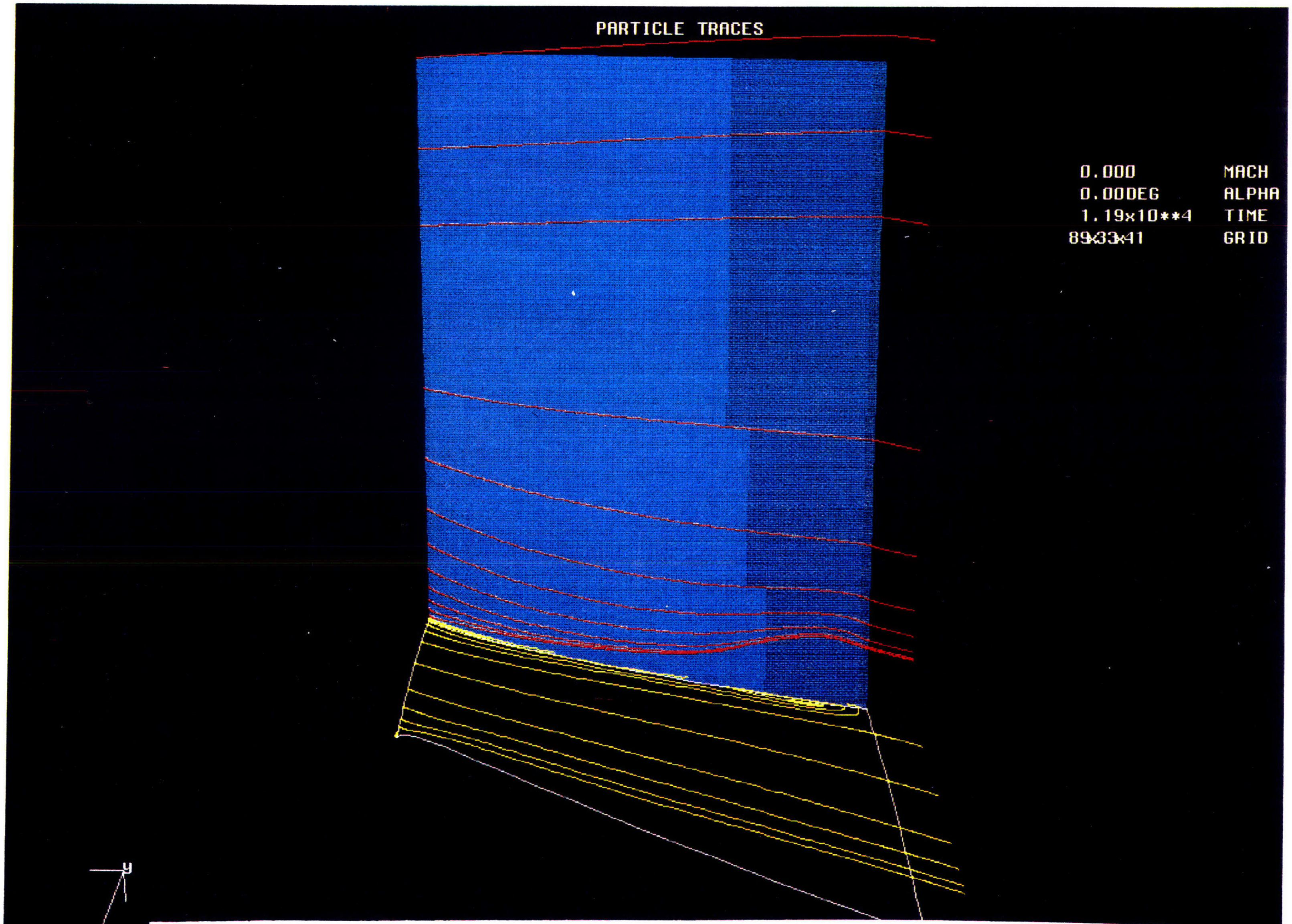

Figure 4.6 No Clearance/Stationary Hub: Particle Traces in the 3-D Flowfield

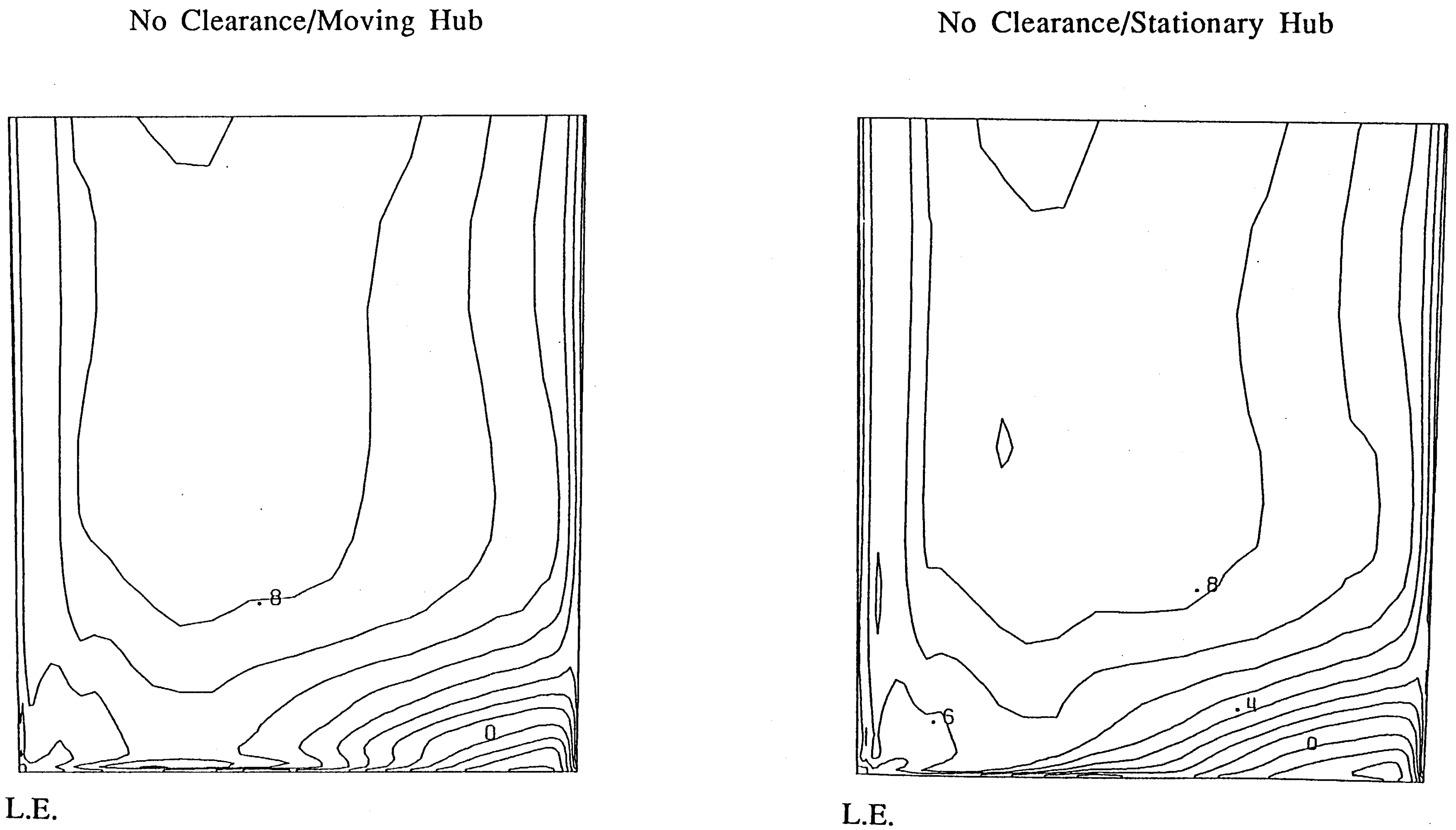
No Clearance/Moving Hub

No Clearance/Stationary Hub

Figure 4.7 u/CX Near Suction Surface

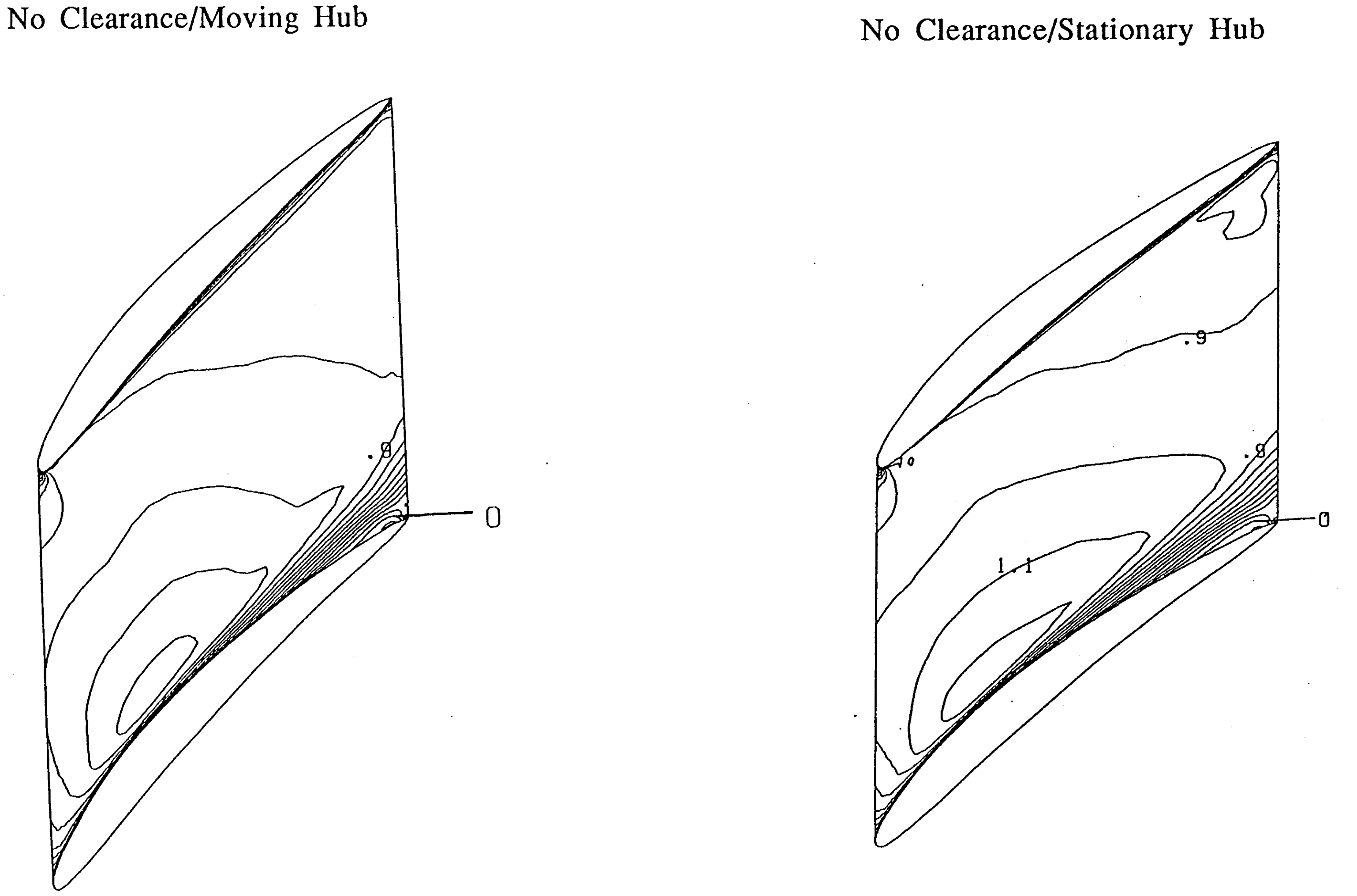

Figure 4.8 u/CX on Radial Planes at 2.4% Span

No Clearance/Moving Hub

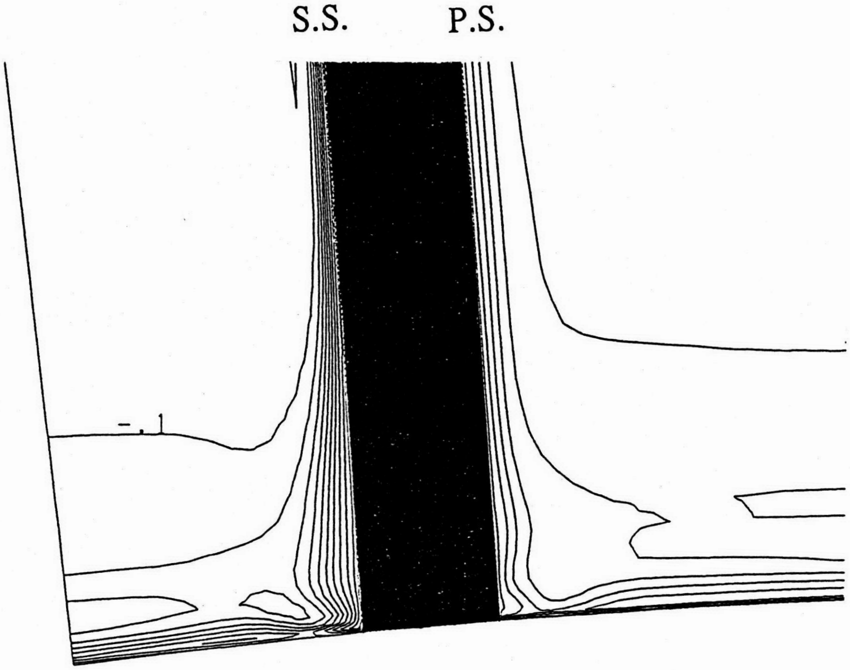

No Clearance/Stationary Hub

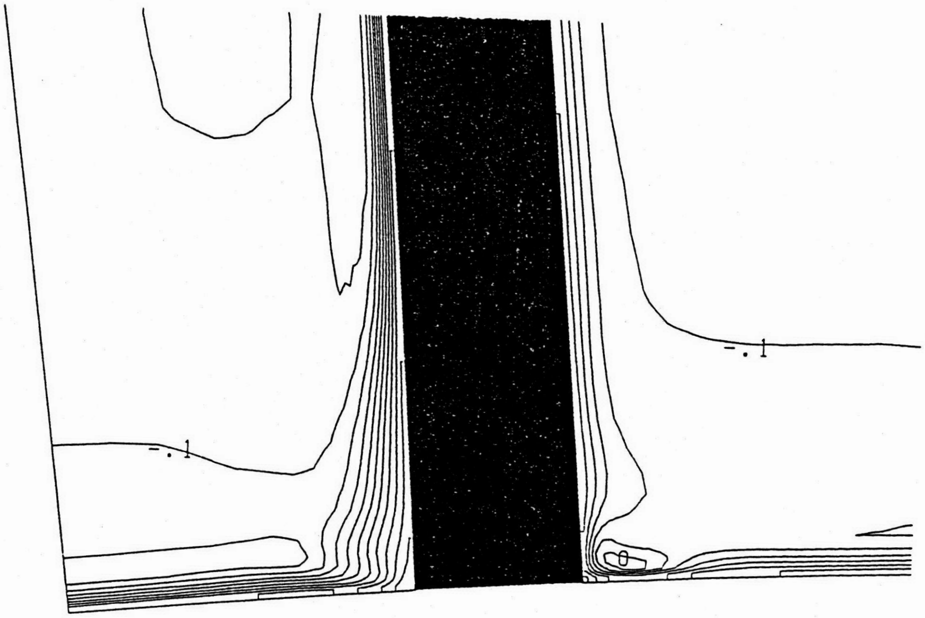

Figure 4.9 $(P_T - P_{Tin})/Q_{in}$ at 50% Chord

No Clearance/Moving Hub

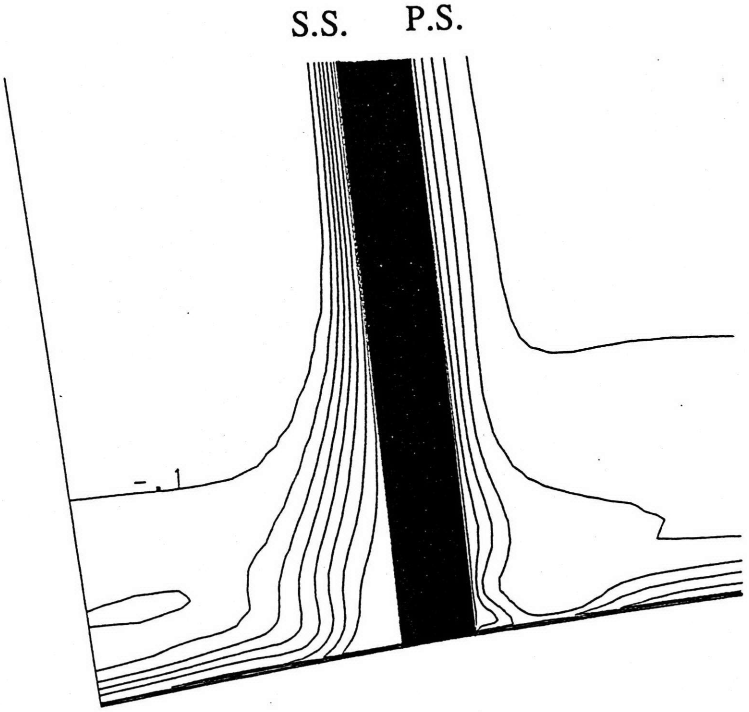

No Clearance/Stationary Hub

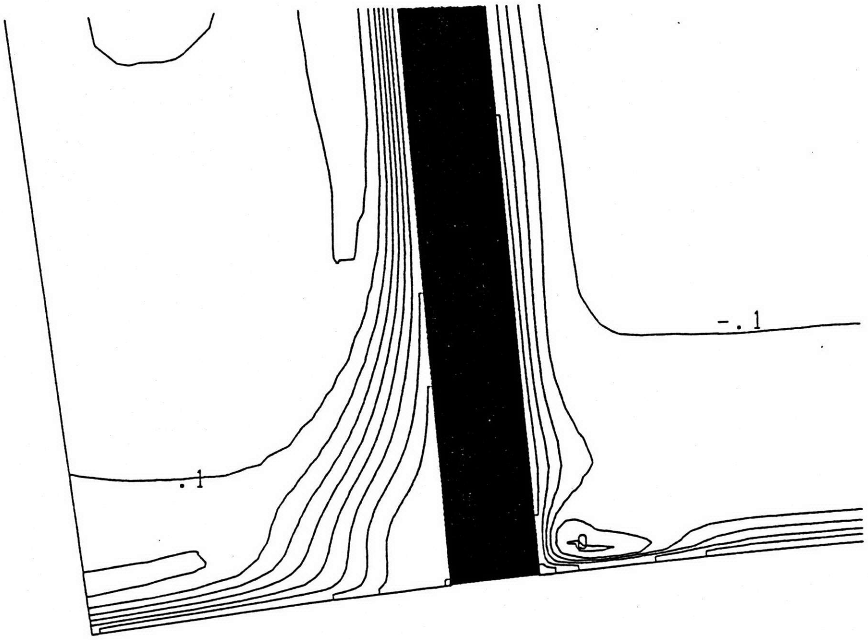

Figure 4.10 $(P_T - P_{Tin})/Q_{in}$ at 79% Chord

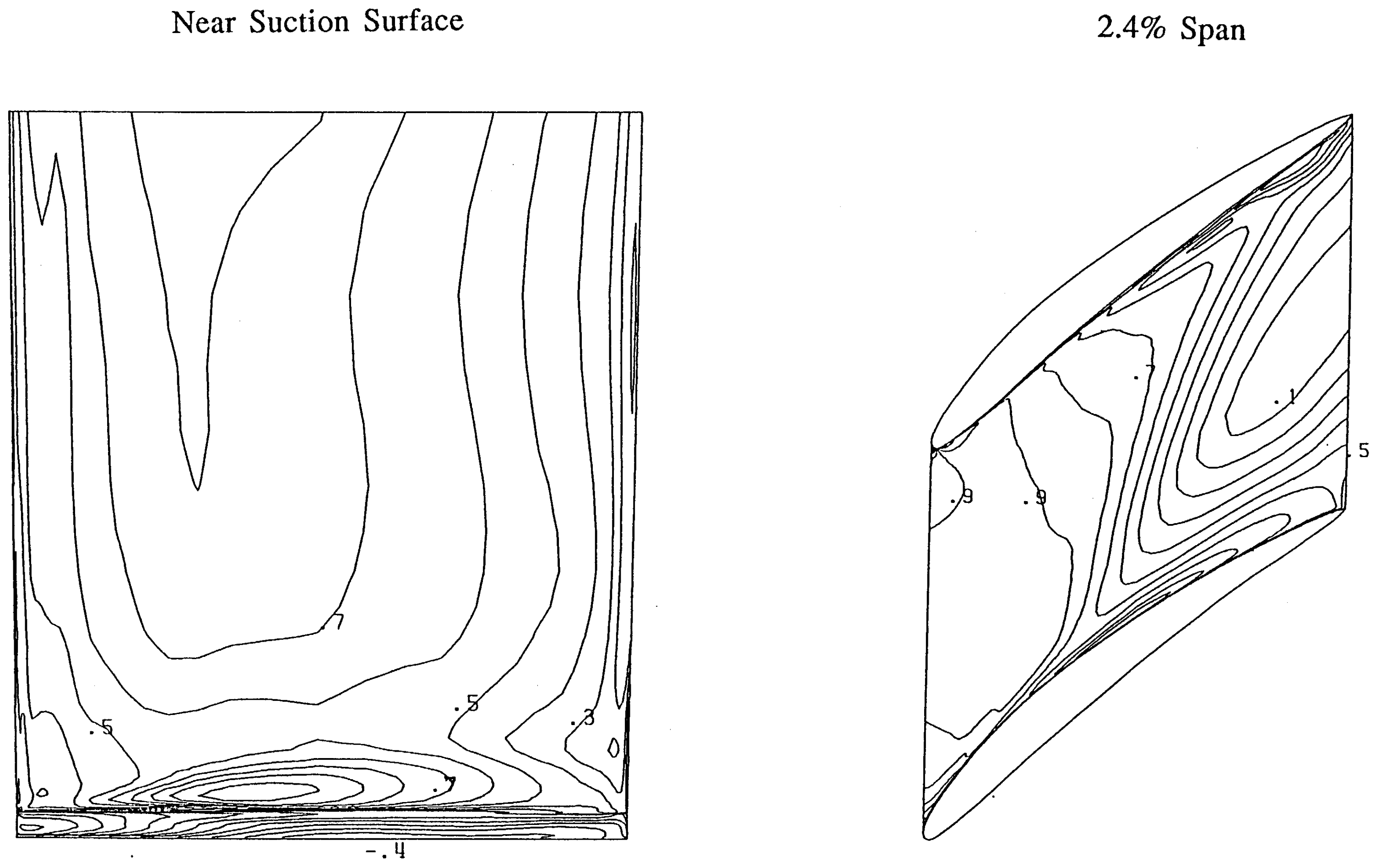

Near Suction Surface

2.4% Span

Figure 4.11 u/CX for Hub Clearance/Smooth Moving Hub

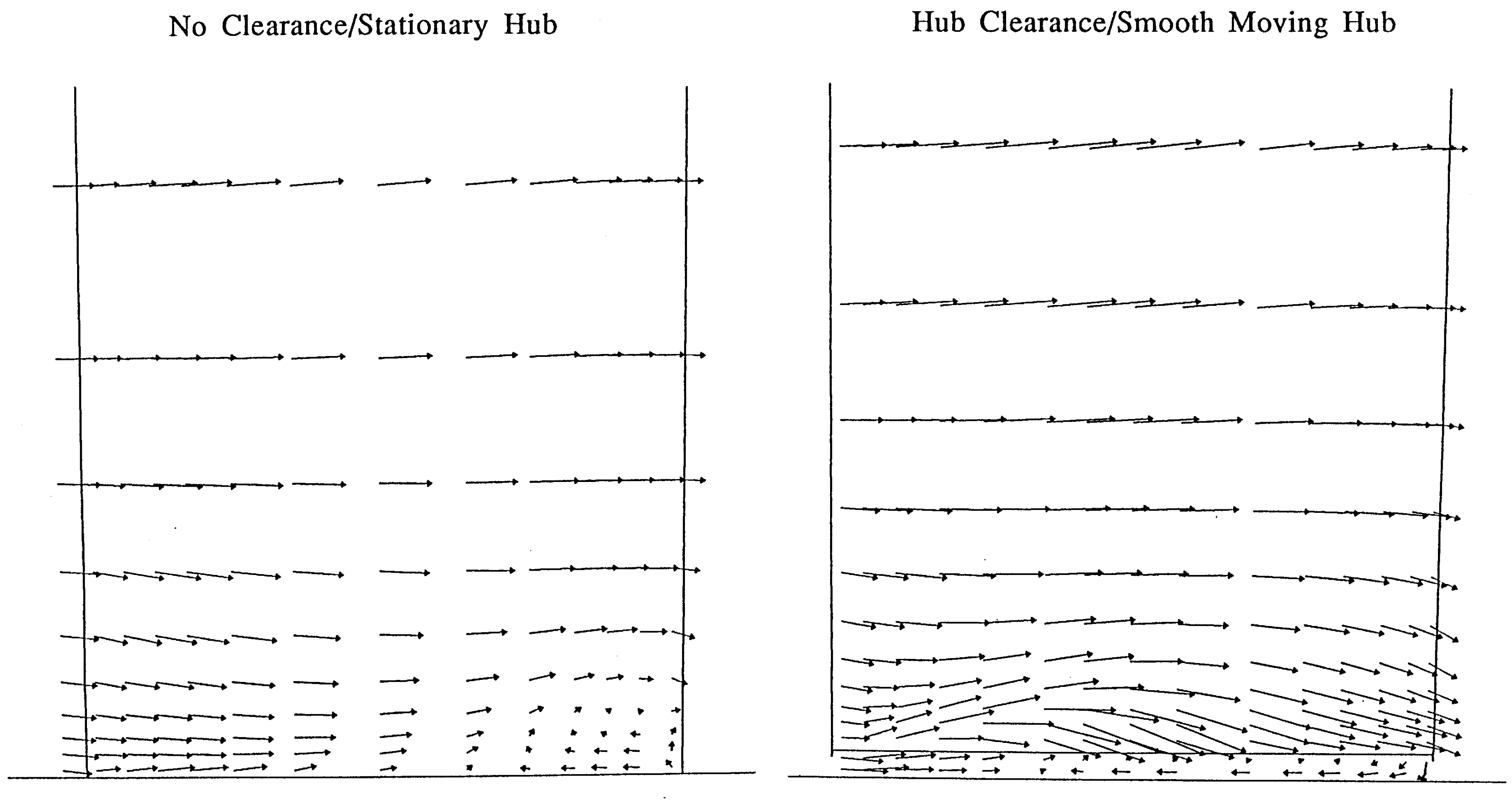

No Clearance/Stationary Hub

Hub Clearance/Smooth Moving Hub

Figure 4.12 Velocity Vectors Near Suction Surface

36% Chord

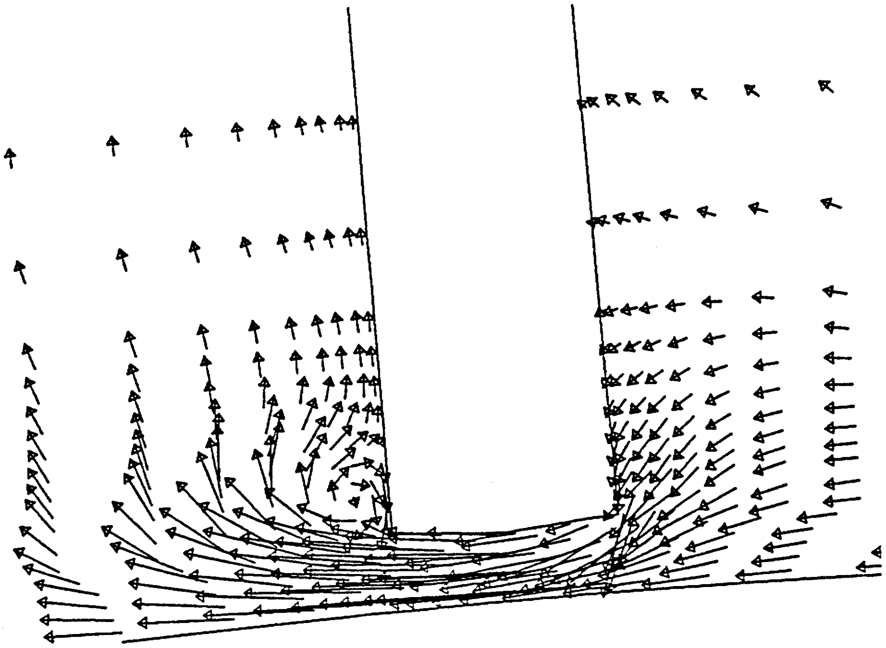

64% Chord

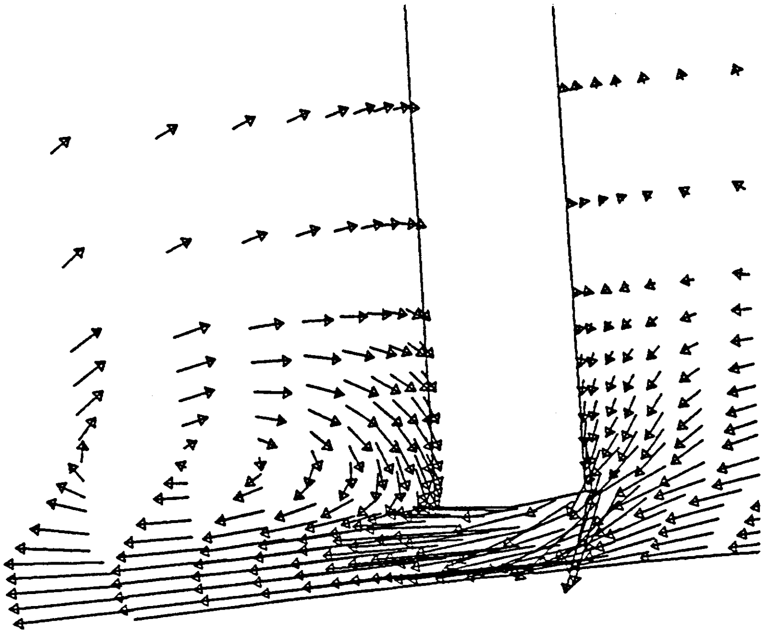

Figure 4.13 Hub Clearance: Velocity Vectors on Axial Planes

36% Chord

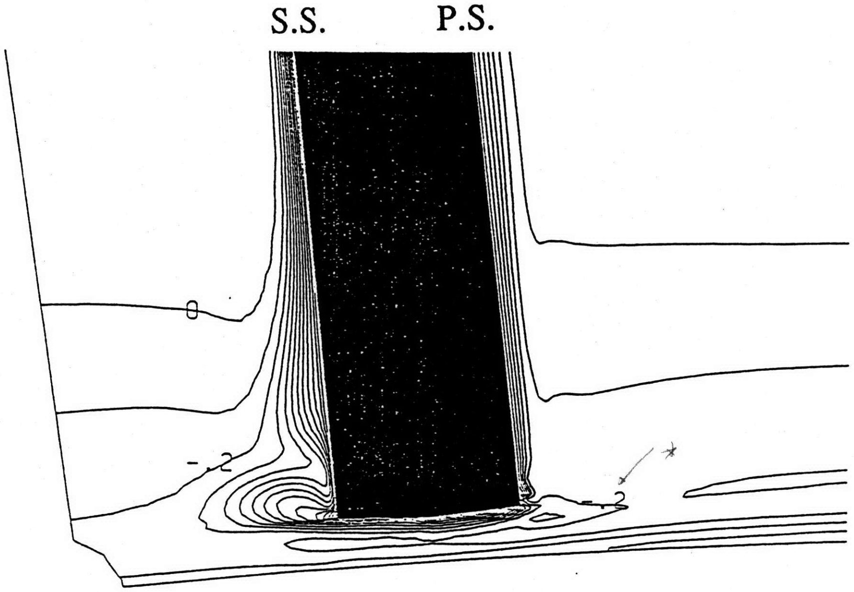

50% Chord

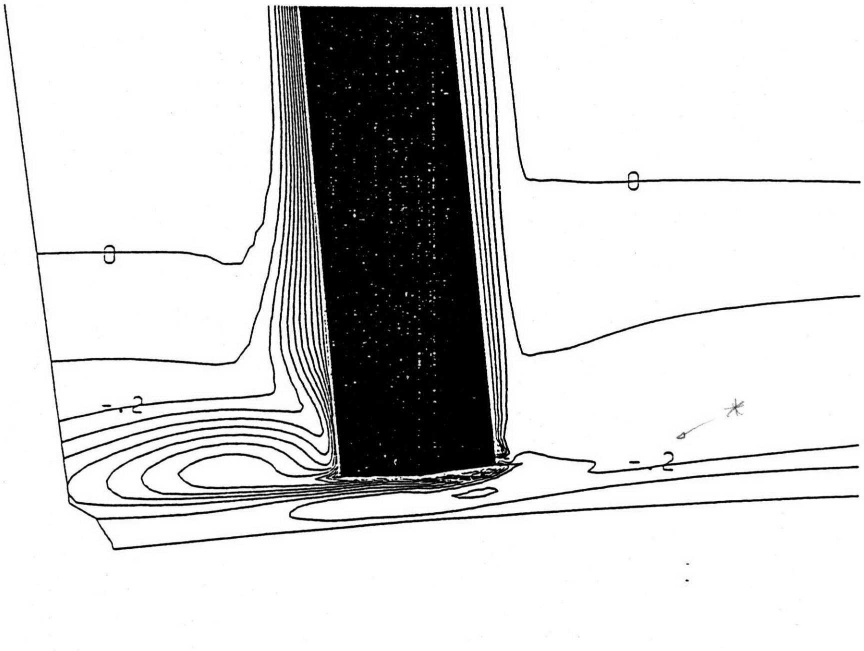

Figure 4.14 Hub Clearance: $(P_T - P_{Tin})/Q_{in}$ at Axial Planes

64% Chord

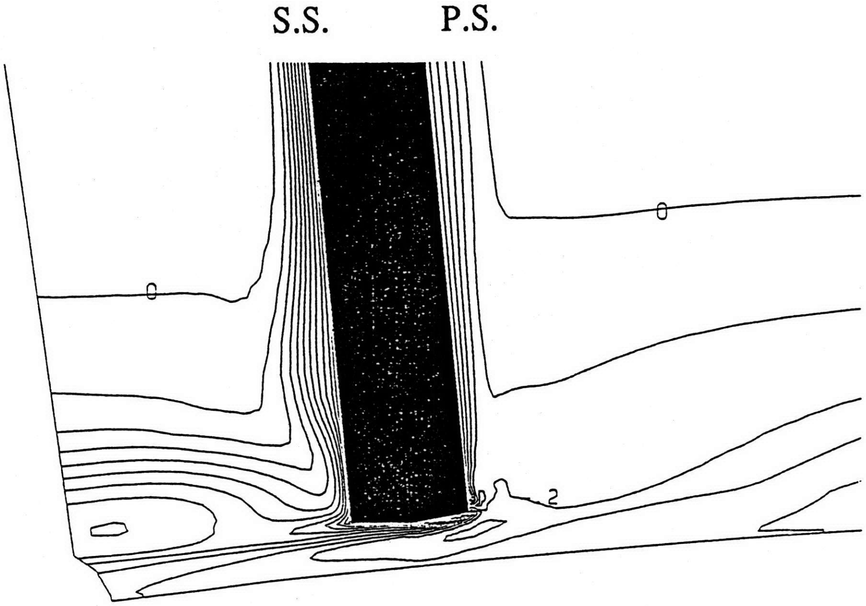

78% Chord

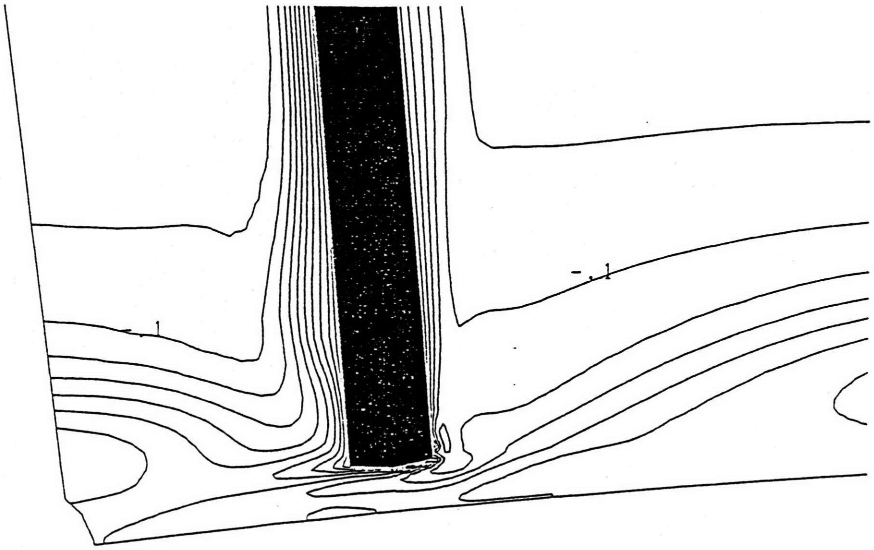

Figure 4.15 Hub Clearance: $(P_T - P_{Tin})/Q_{in}$ at Axial Planes

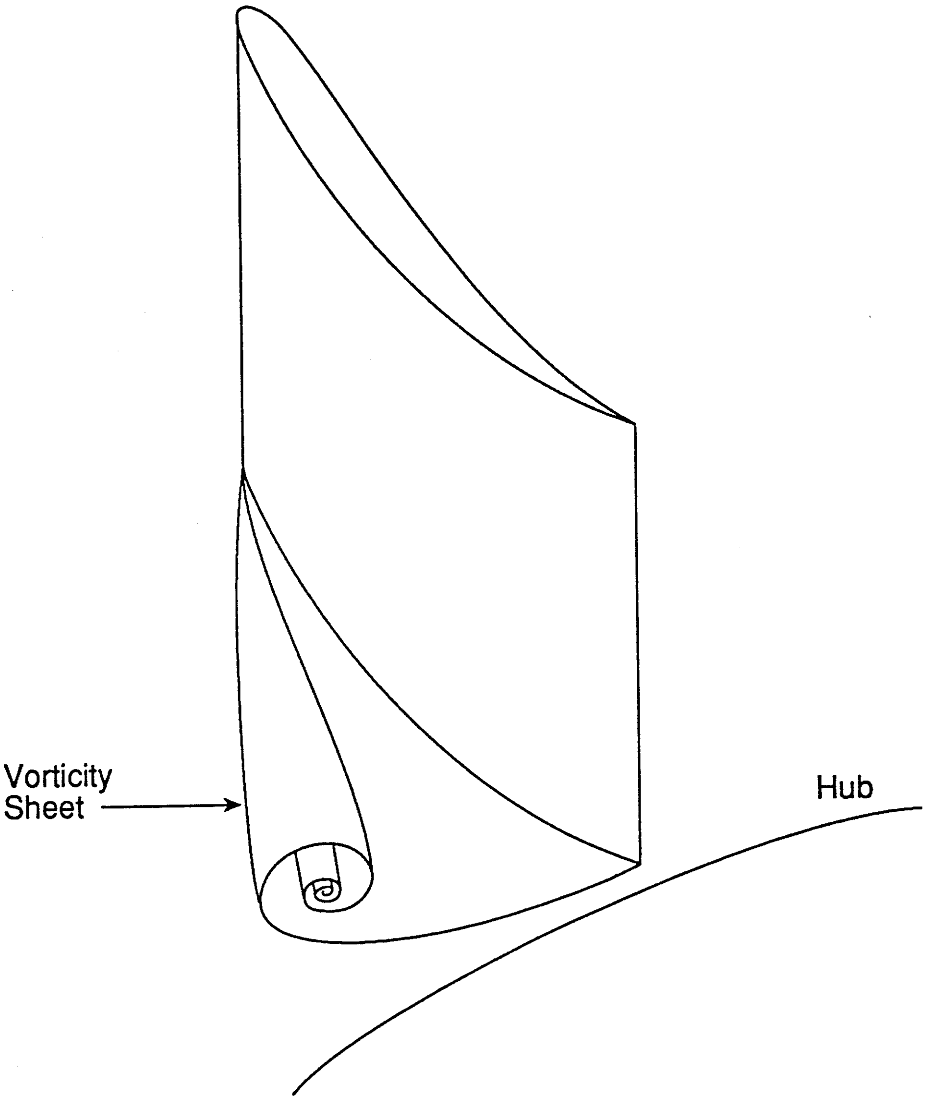

Figure 4.16 Roll Up of Vorticity Shed From Blade Tip

31 Degree View Angle

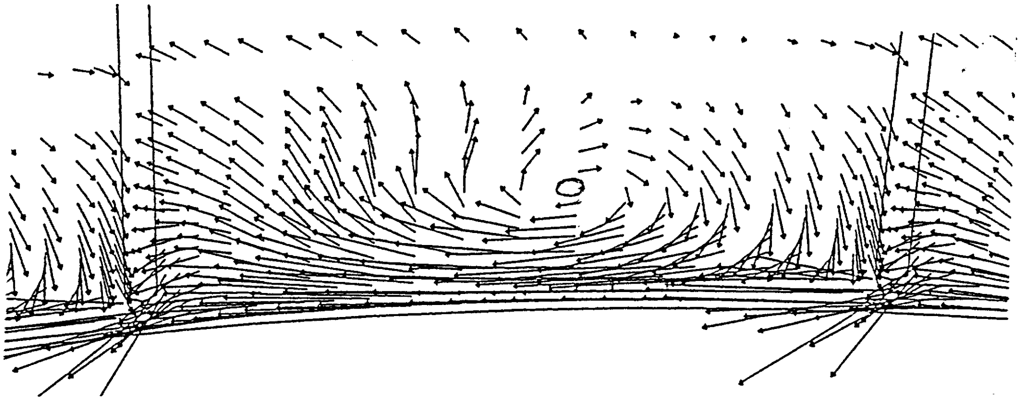

55 Degree View Angle

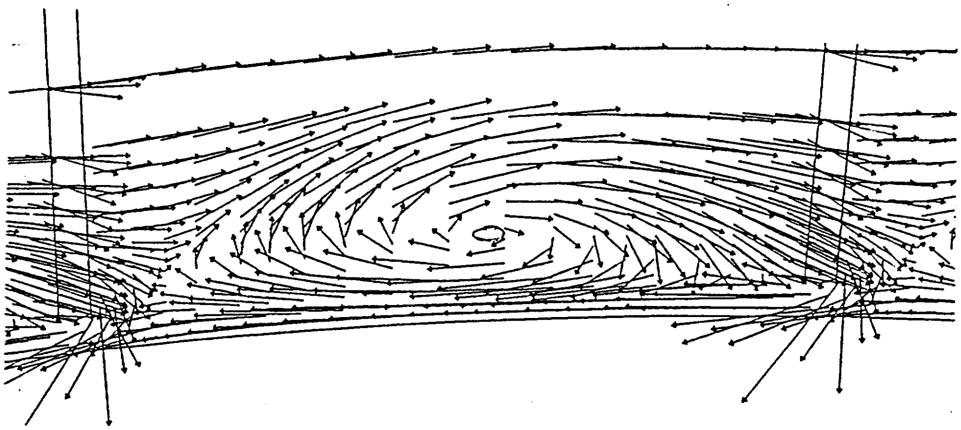

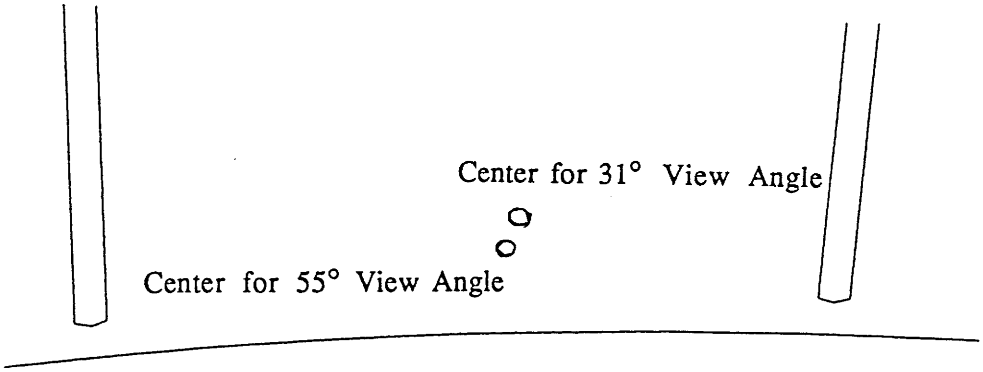

Figure 4.17 Velocity Vectors at 90% Chord

Streamwise Vorticity

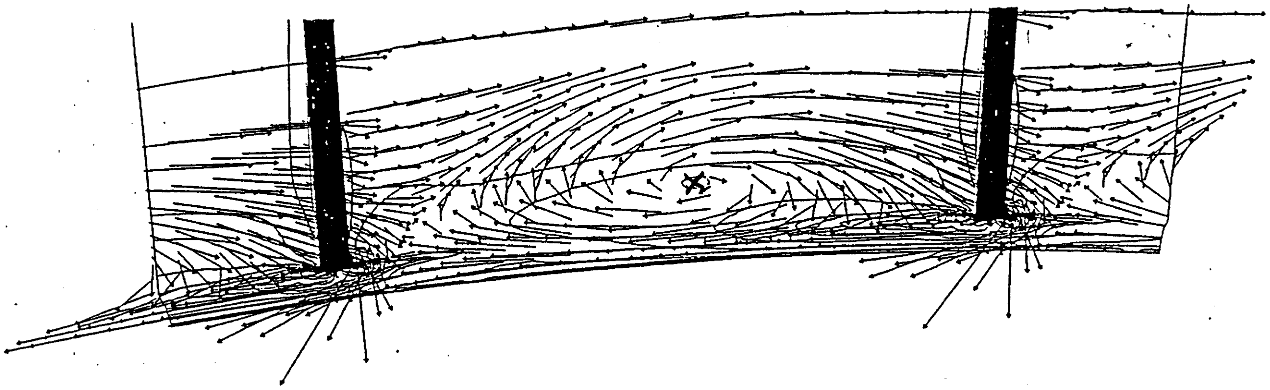

Static Pressure

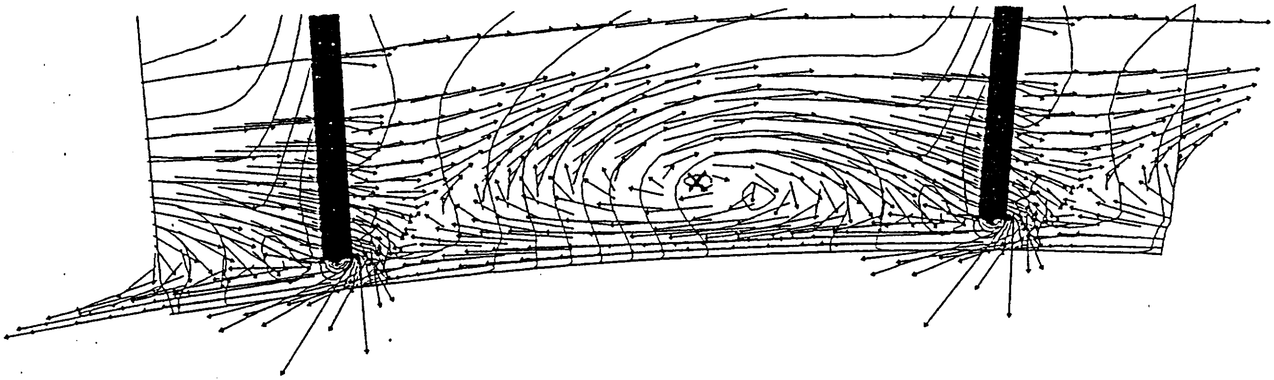

Total Pressure

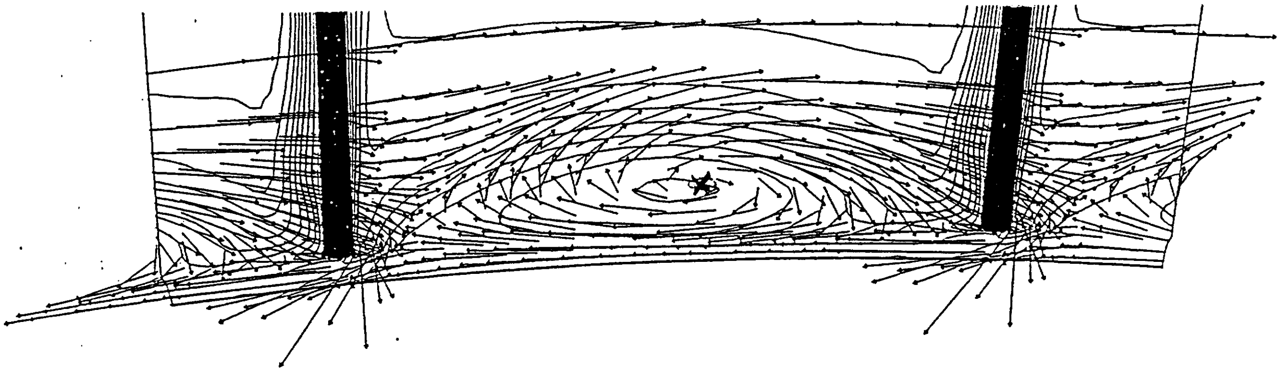

Figure 4.18 Velocity Vectors at 90% Chord upon Contour Plots
(View Angle = 55 deg)

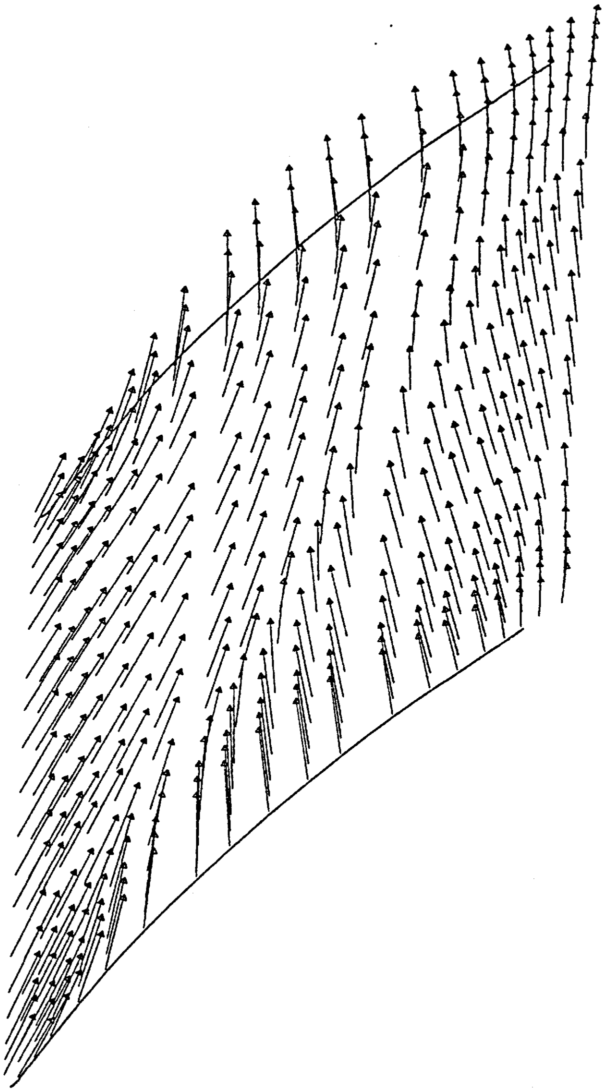

Figure 4.19 Velocity Vectors at 0.3% Span

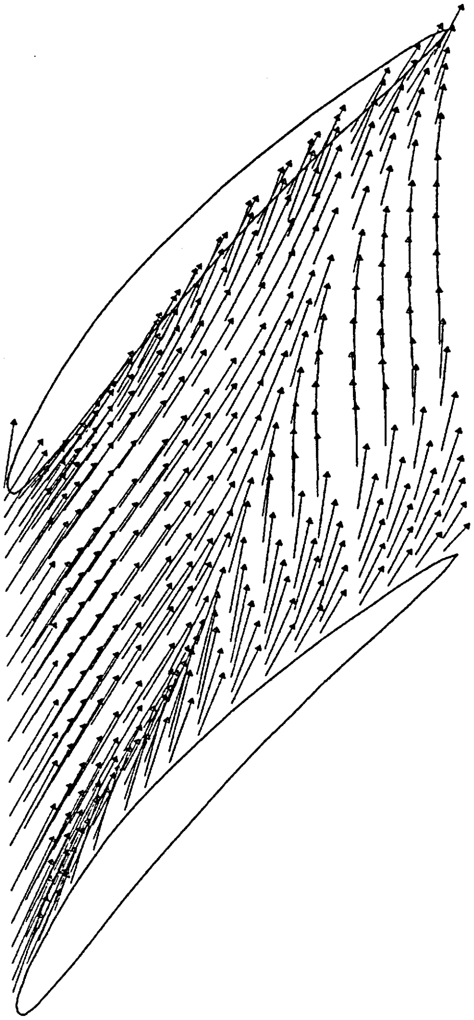

Figure 4.20 Velocity Vectors at 2.0% Span

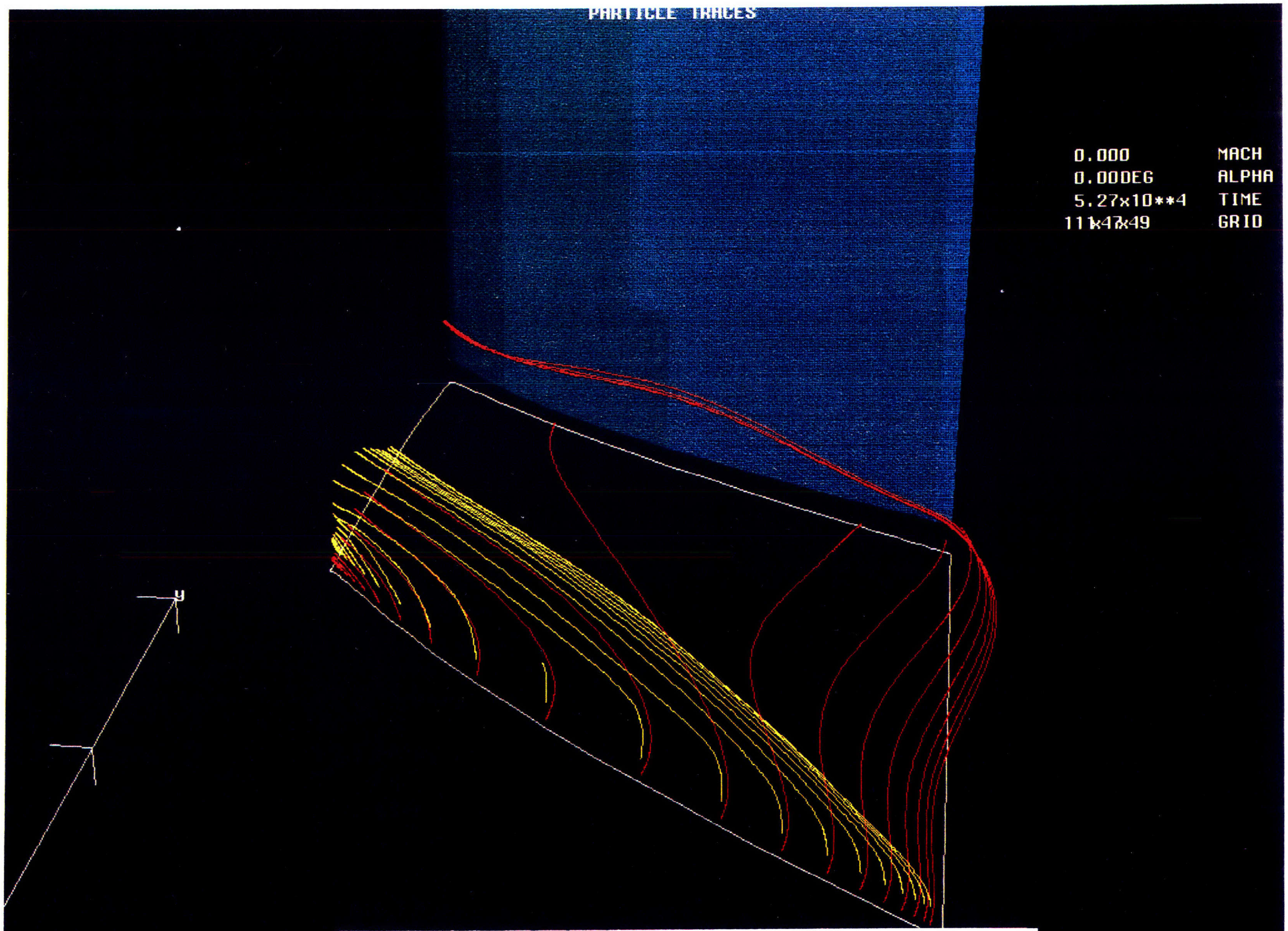

Figure 4.21 Particle Traces of Hub Clearance Flow

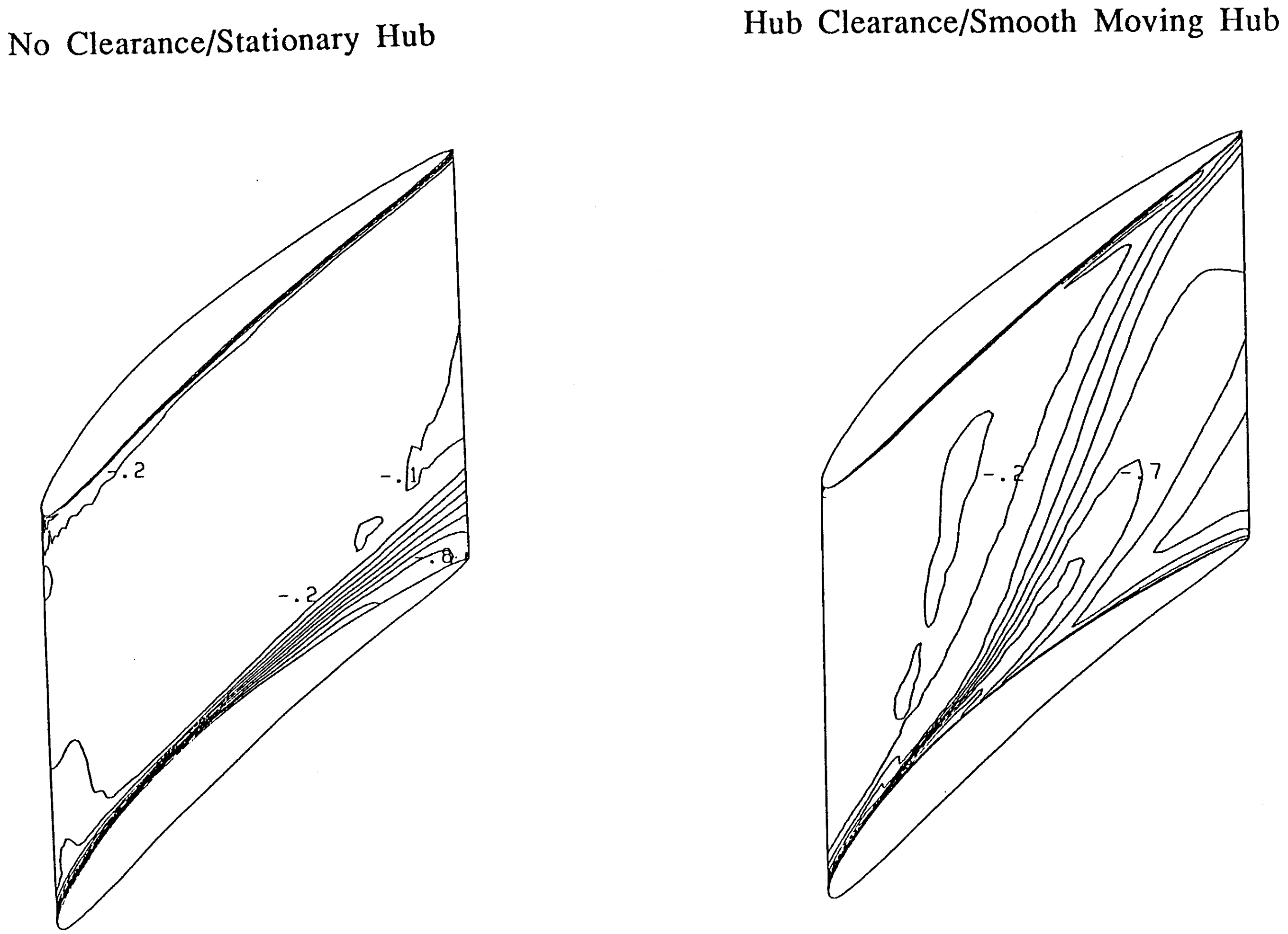

No Clearance/Stationary Hub

Hub Clearance/Smooth Moving Hub

Figure 4.22 $(P_T\text{-}P_{T\text{in}})/Q_{\text{in}}$ at 2.4% Span

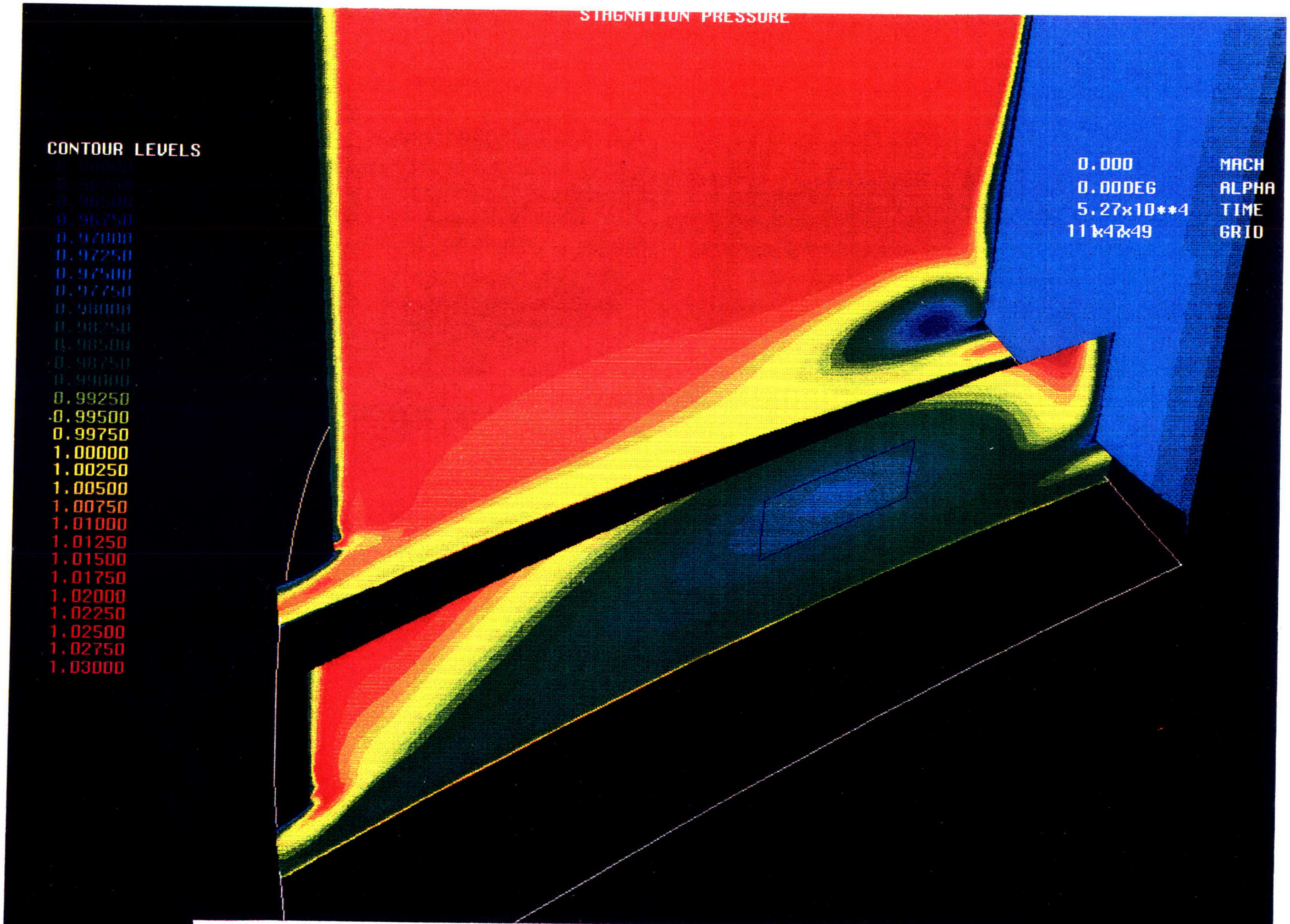

Figure 4.23 Total Pressure Contours in the 3-D Flowfield

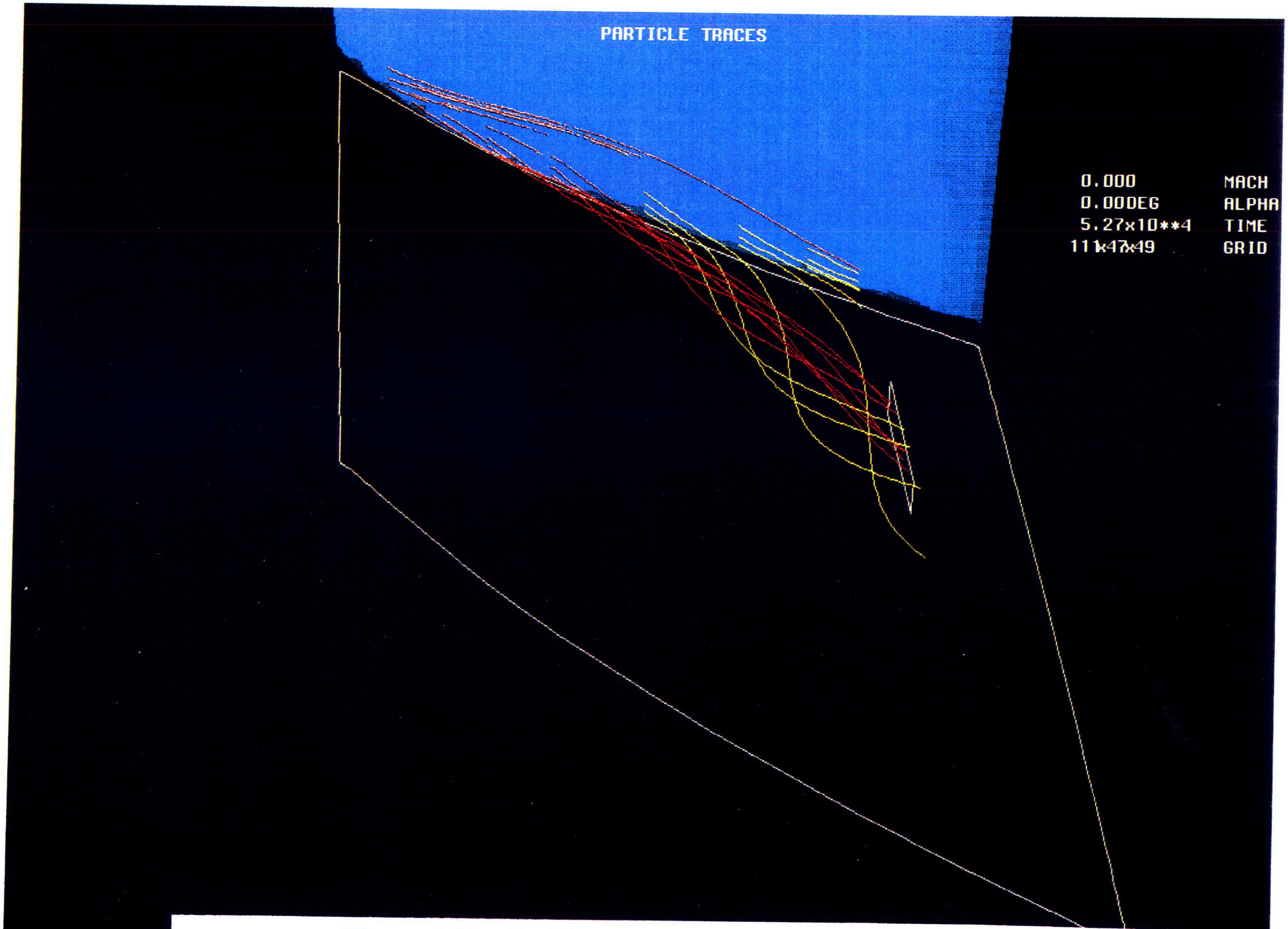

Figure 4.24 Particles Released from the Blade Surface

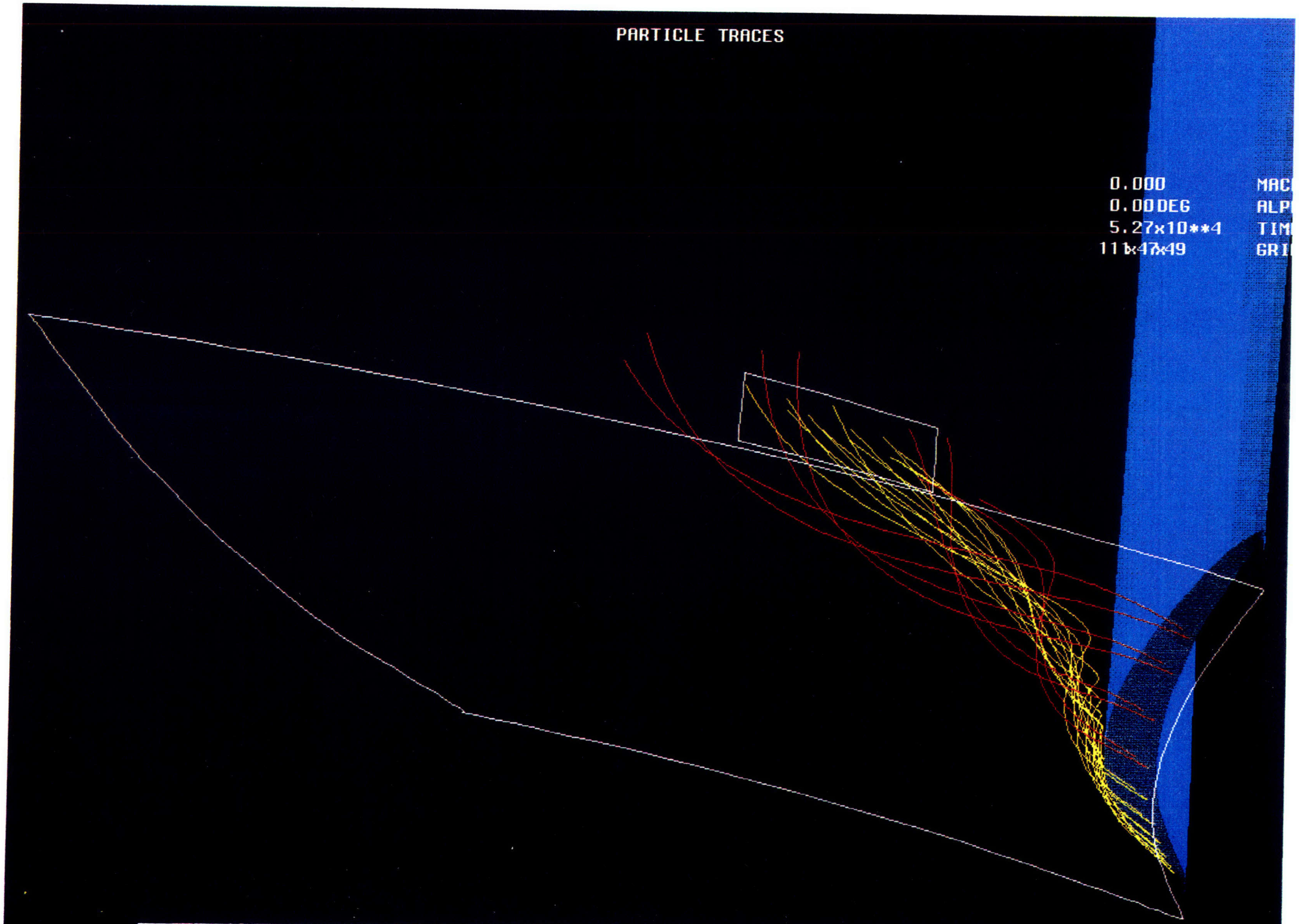

Figure 4.25 Particles Released from the Blade Tip

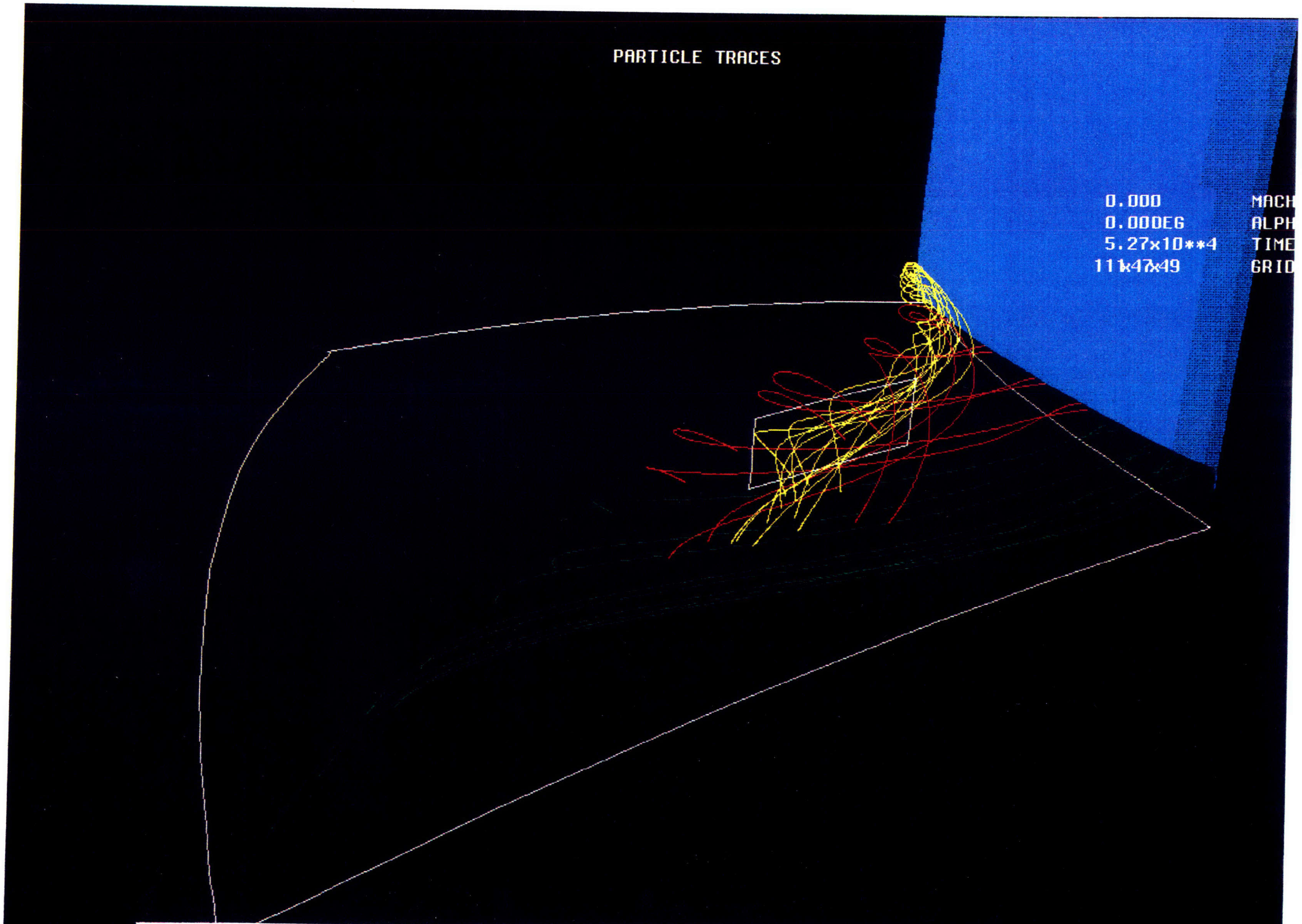

Figure 4.26 Particles Released from the Blade Tip

40% Chord

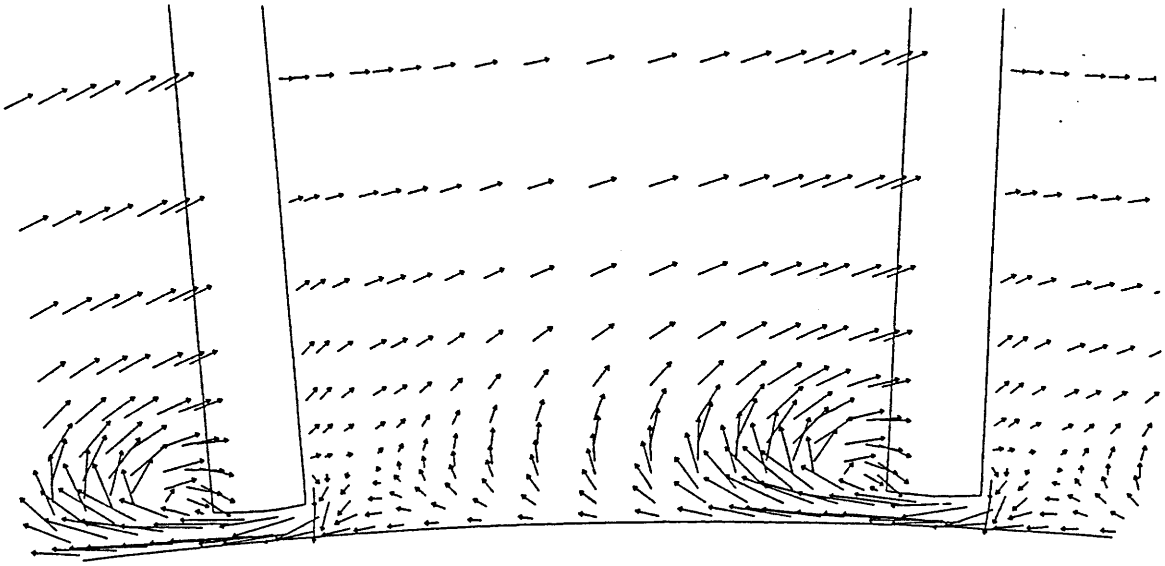

80% Chord

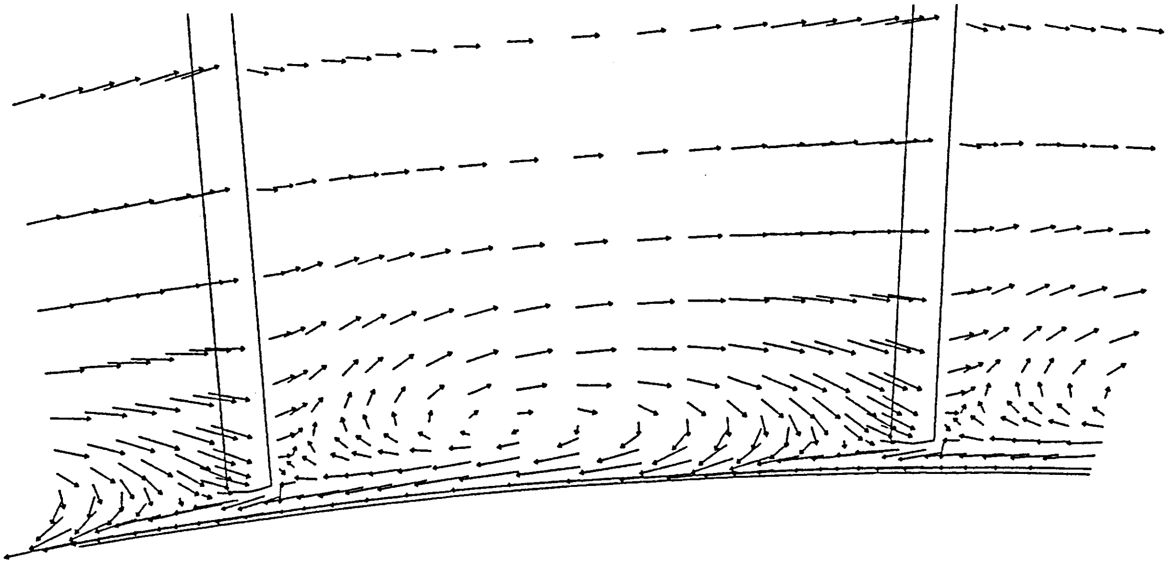

Figure 4.27 Inviscid Hub Clearance/Smooth Hub: Velocity Vectors on Axial Planes (View Angle = 55 Deg)

40% Chord

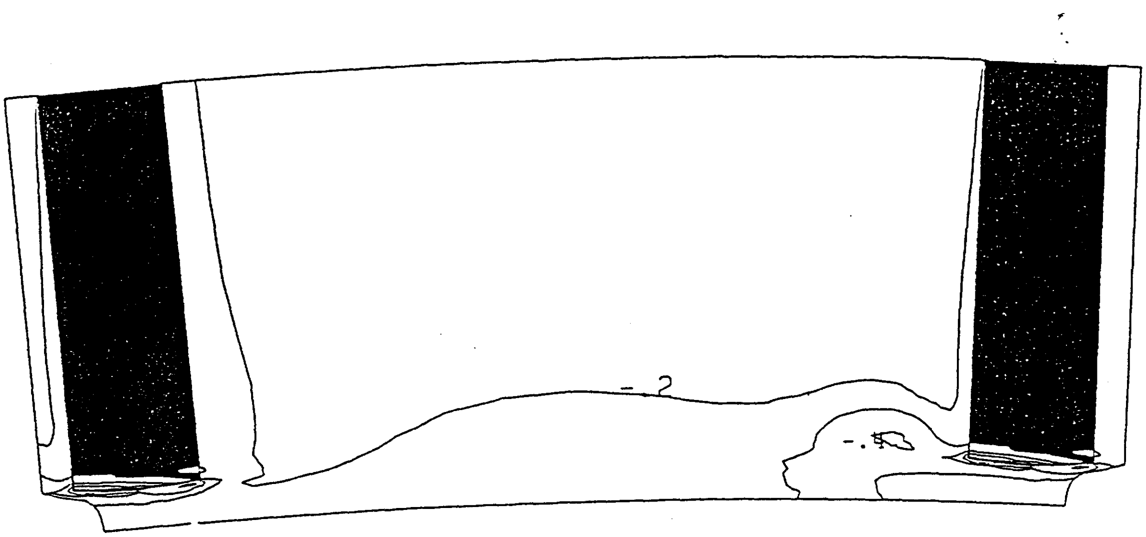

80% Chord

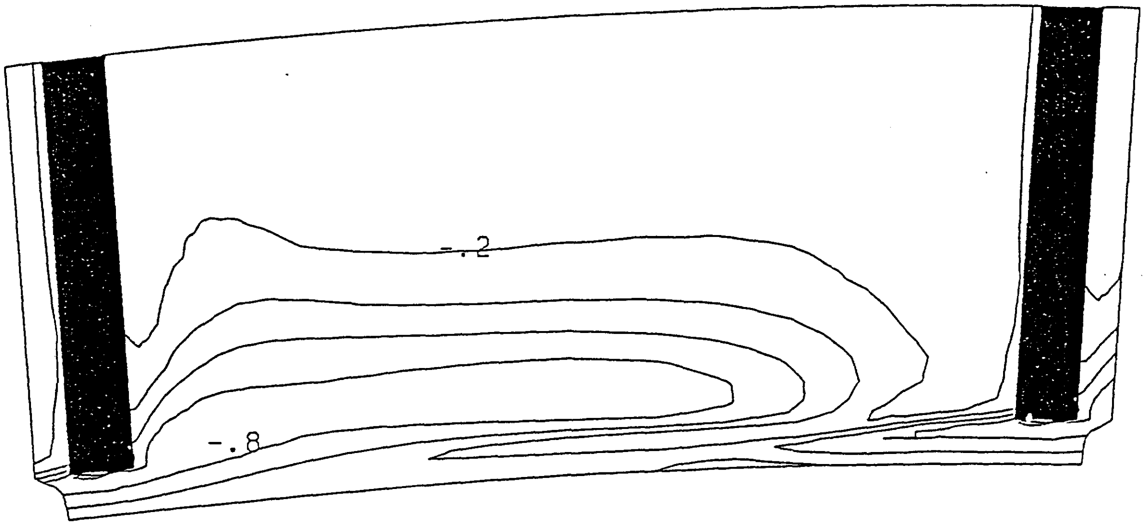

Figure 4.28 Inviscid Hub Clearance/Smooth Hub: $(P_T - P_{Tin})/Q_{in}$ at Axial Planes

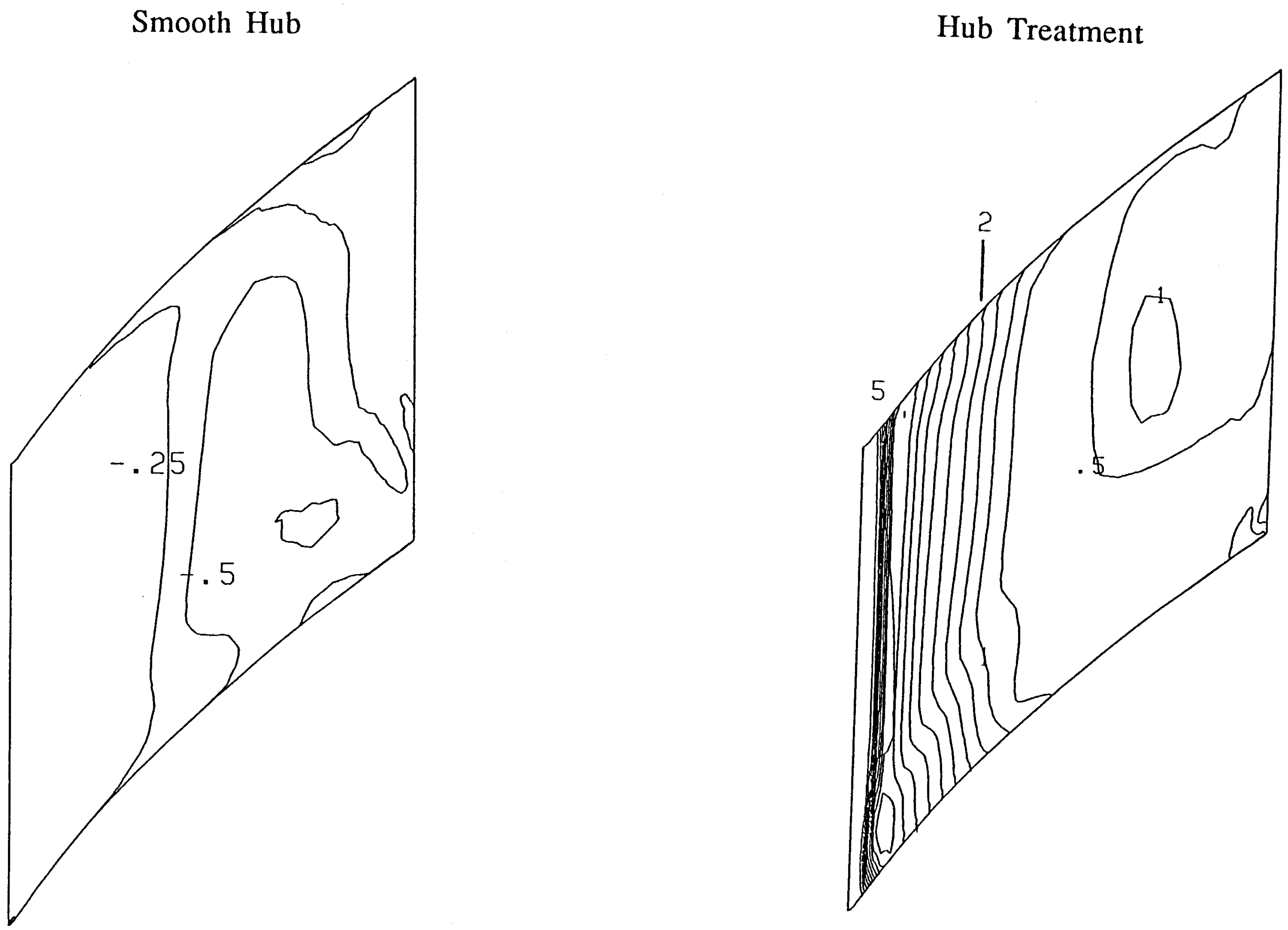

Figure 4.29 $(P_T - P_{Tin})/Q_{in}$ at 0.9% Span

10% Chord

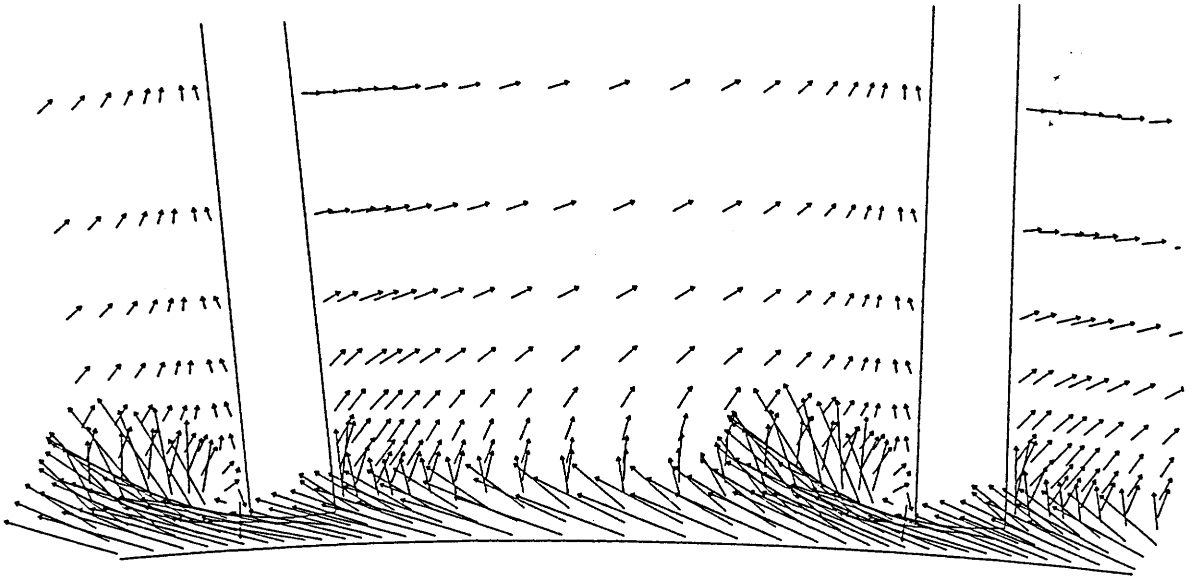

40% Chord

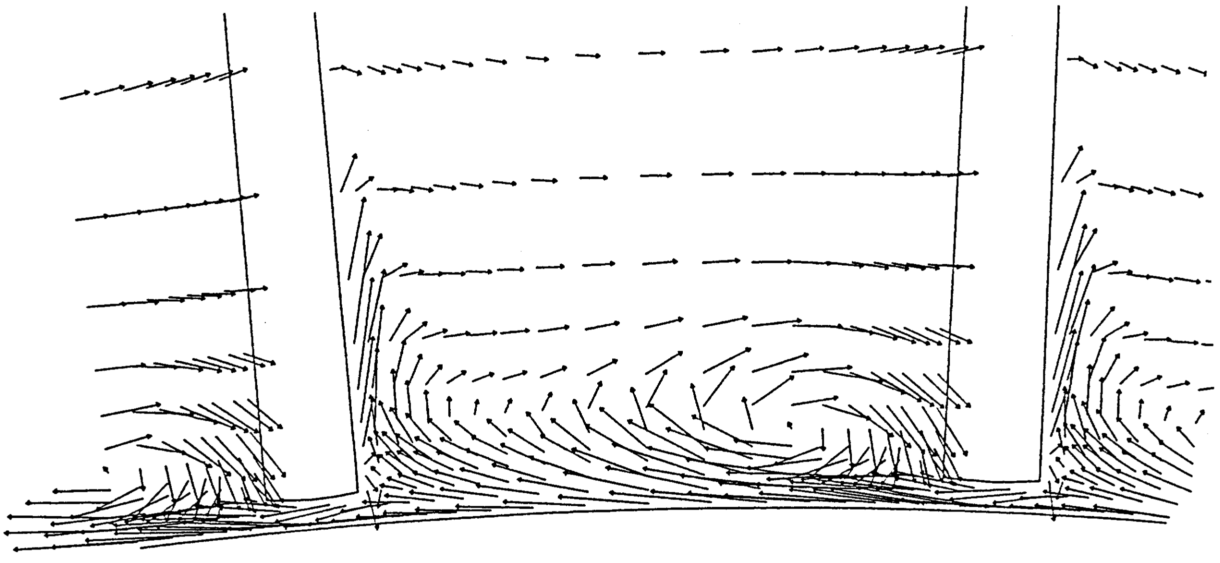

Figure 4.30 Hub Treatment: Velocity Vectors at Axial Planes (View Angle = 55 Deg)

60% Chord

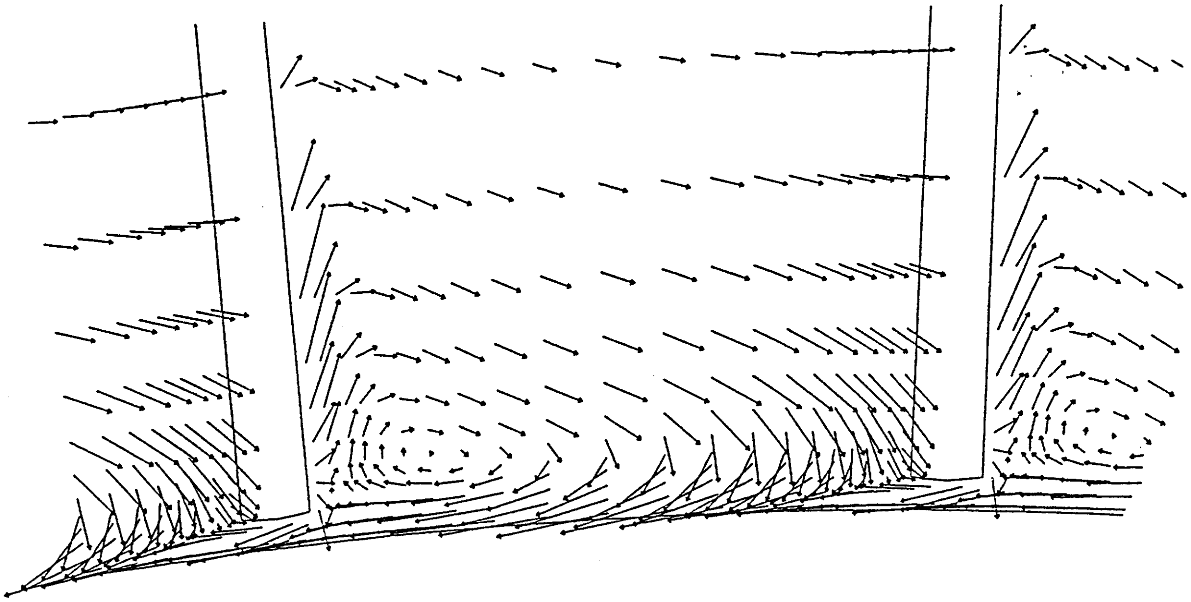

80% Chord

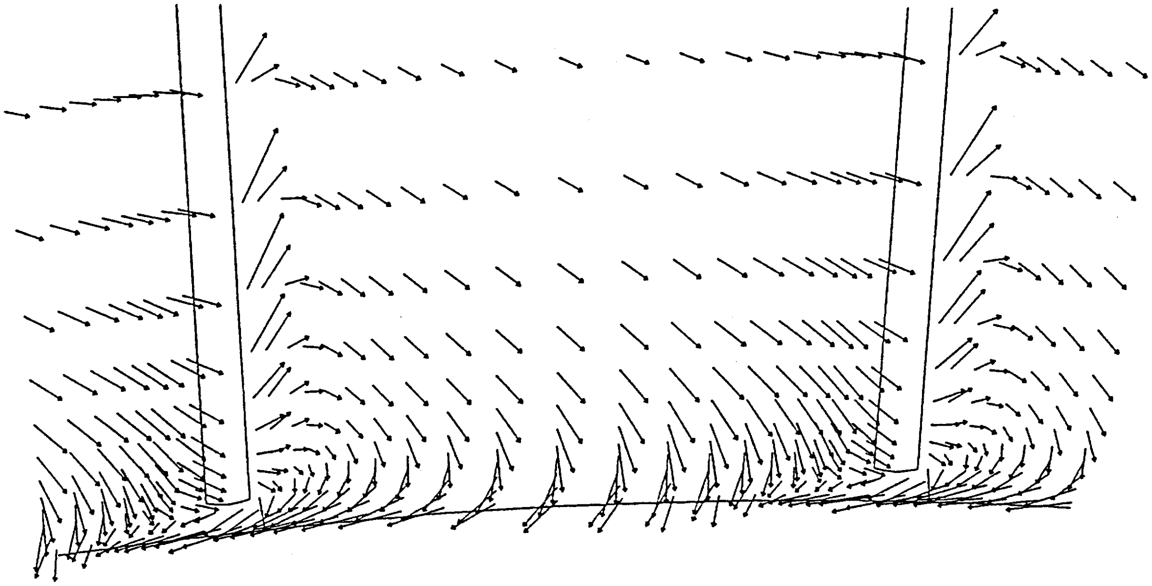

Figure 4.31 Hub Treatment: Velocity Vectors at Axial Planes (View Angle = 55 Deg)

10% Chord

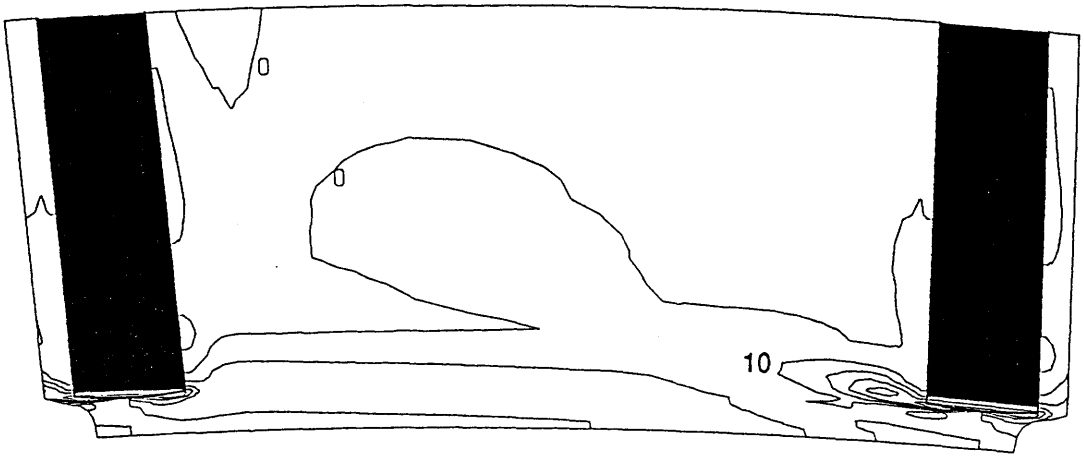

40% Chord

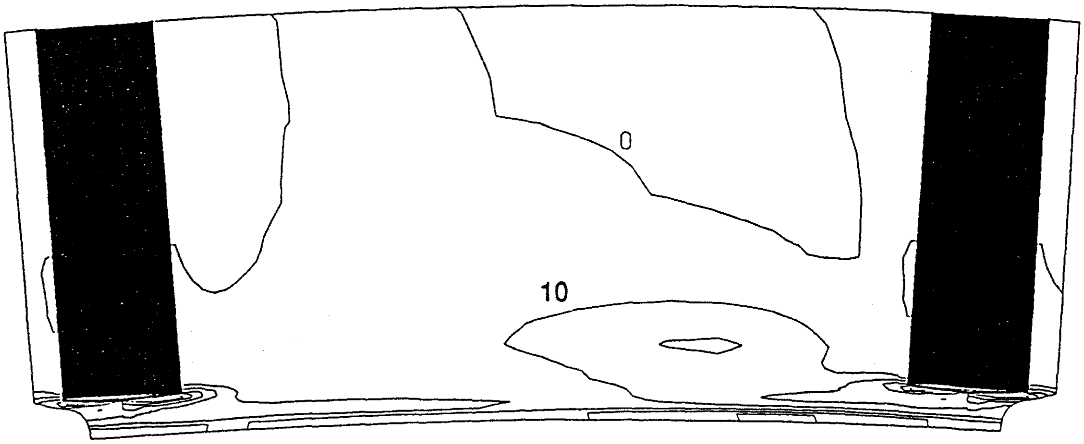

Figure 4.32 Hub Treatment: Streamwise Vorticity (ω_s C/CX) at Axial Planes

10% Chord

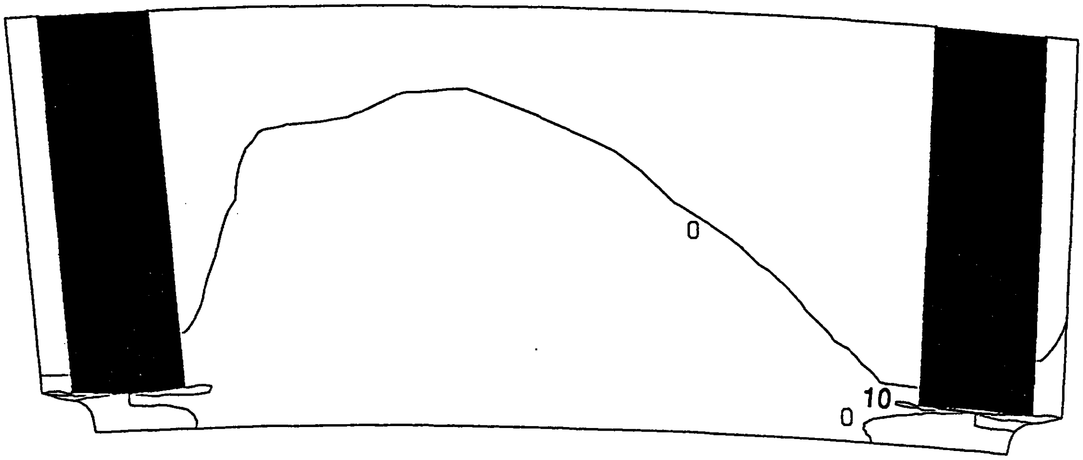

40% Chord

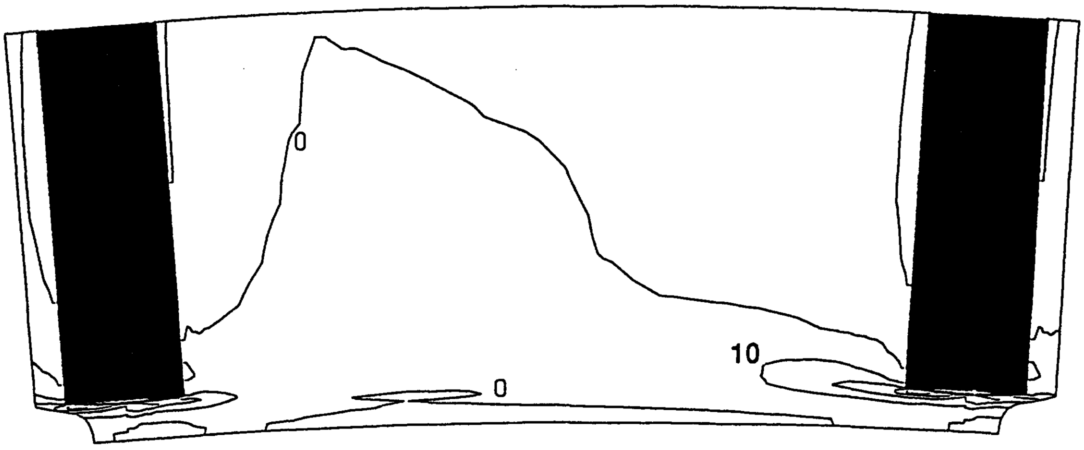

Figure 4.33 Smooth Hub: Streamwise Vorticity (ω_S C/CX) at Axial Planes

60% Chord

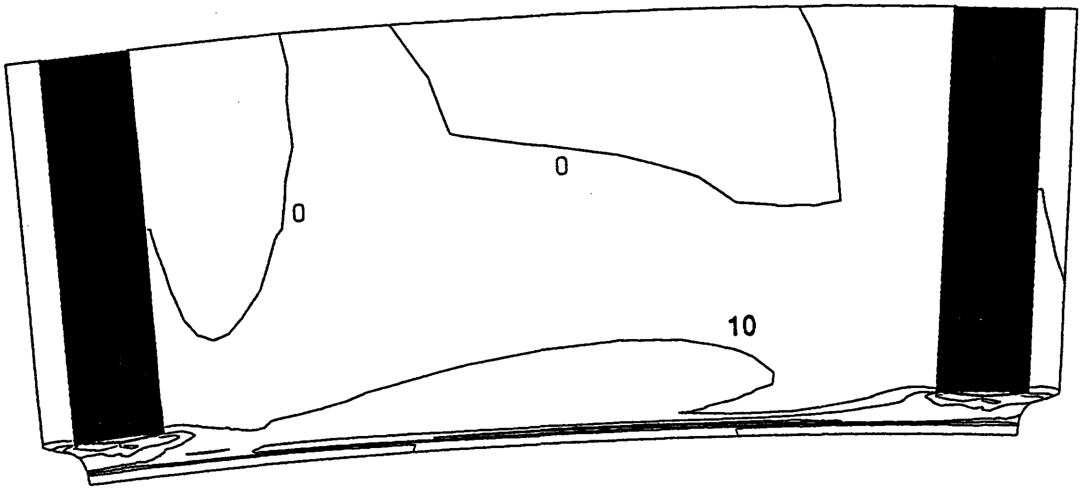

80% Chord

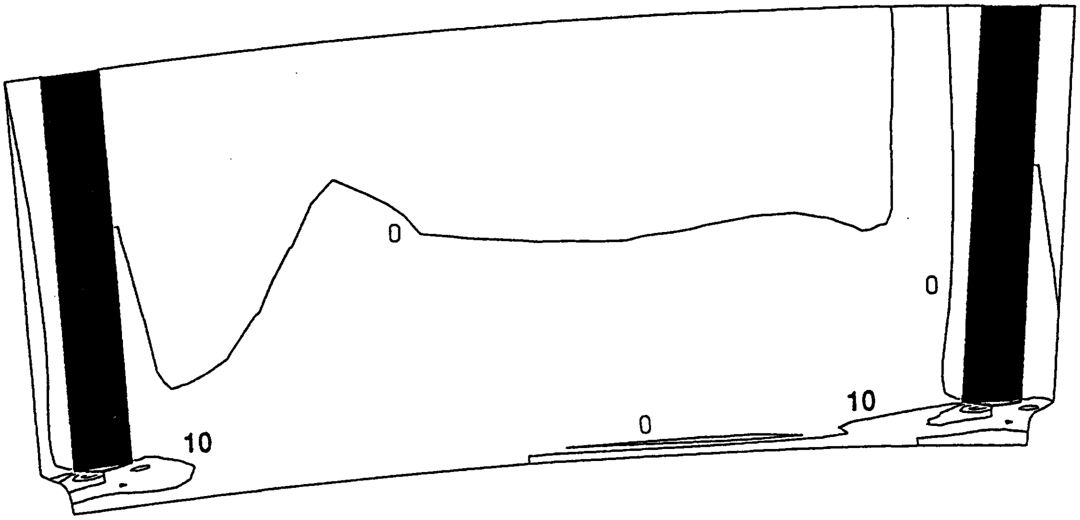

Figure 4.34 Hub Treatment: Streamwise Vorticity (ω_s C/CX) at Axial Planes

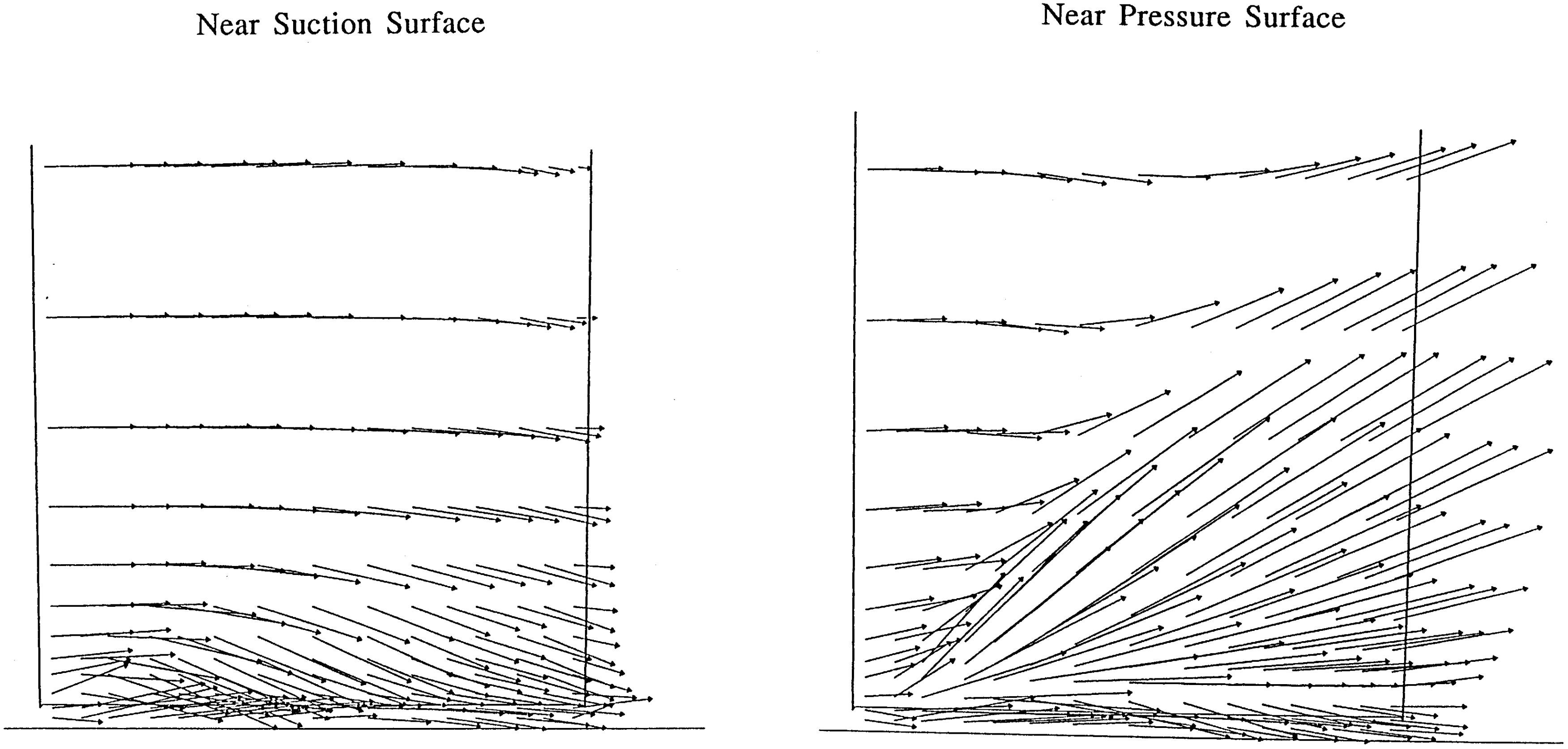

Near Suction Surface

Near Pressure Surface

Figure 4.35 Hub Treatment: Velocity Vectors Near Blade Surfaces

Hub Treatment

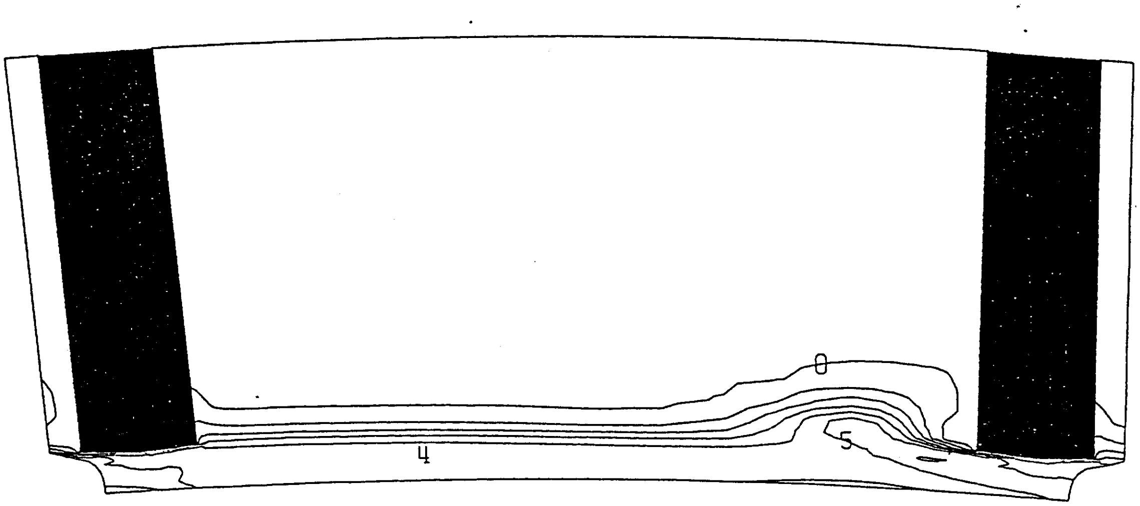

Smooth Hub

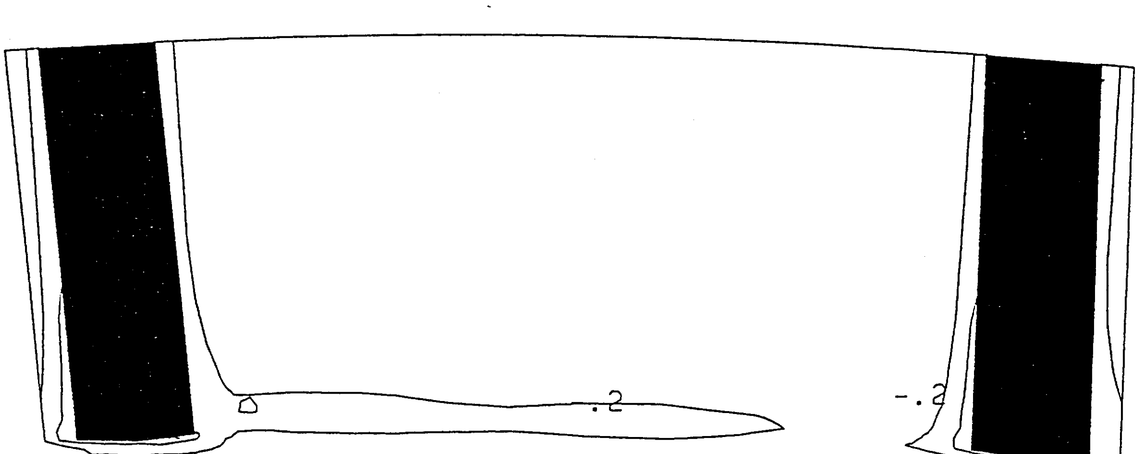

Figure 4.36 $(P_T - P_{T in})/Q_{in}$ at 10% Chord

Hub Treatment

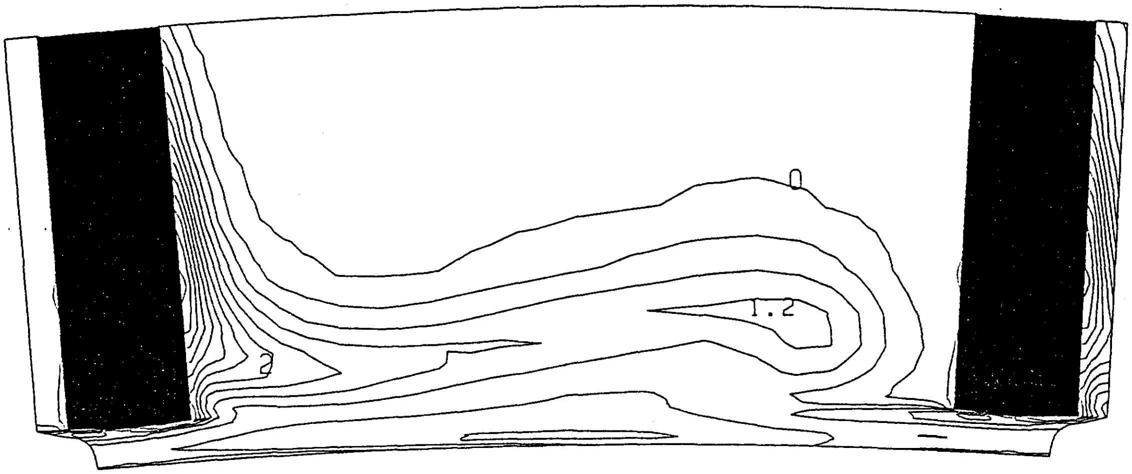

Smooth Hub

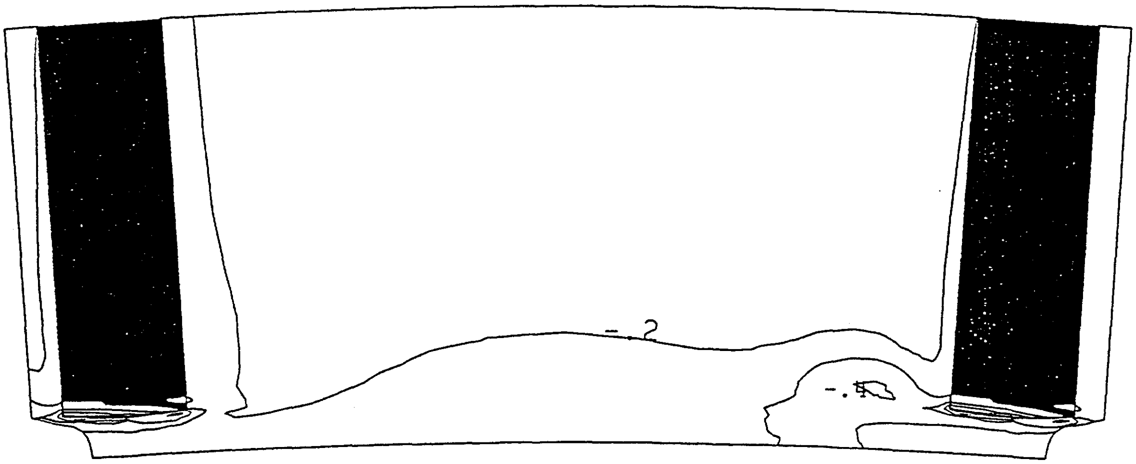

Figure 4.37 $(P_T - P_{Tin})/Q_{in}$ at 40% Chord

Hub Treatment

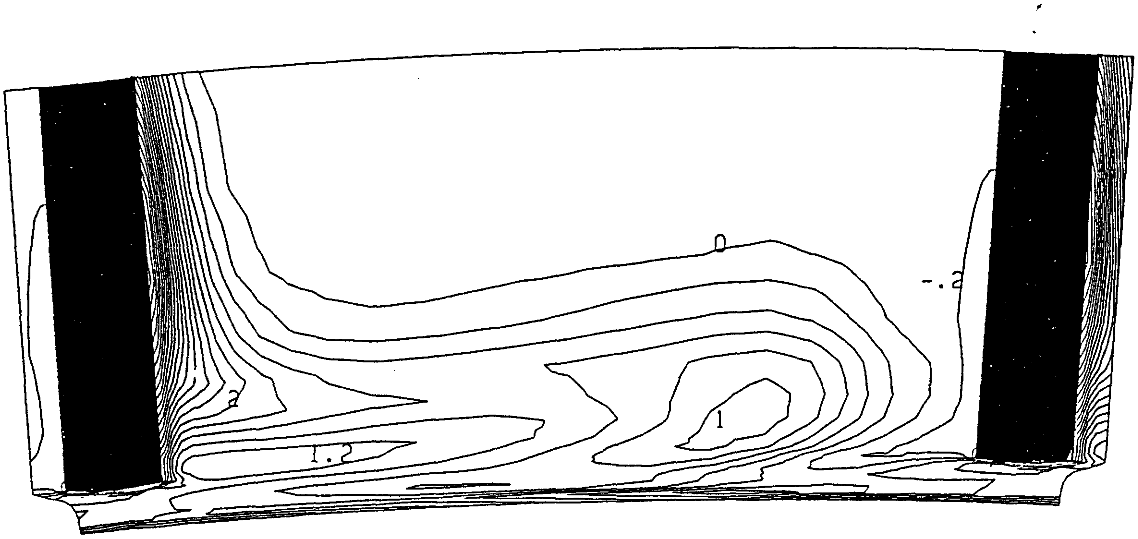

Smooth Hub

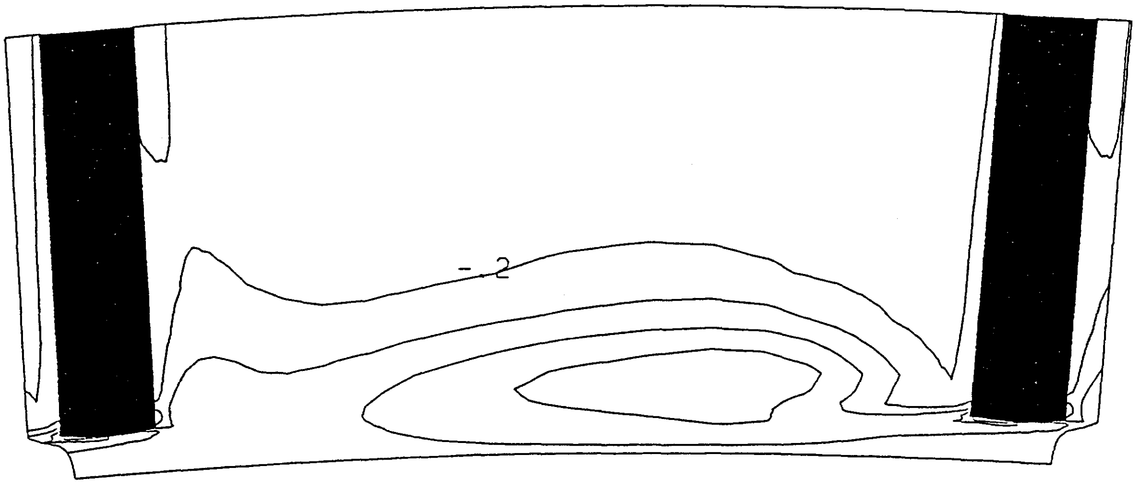

Figure 4.38 $(P_T-P_{Tin})/Q_{in}$ at 60% Chord

Hub Treatment

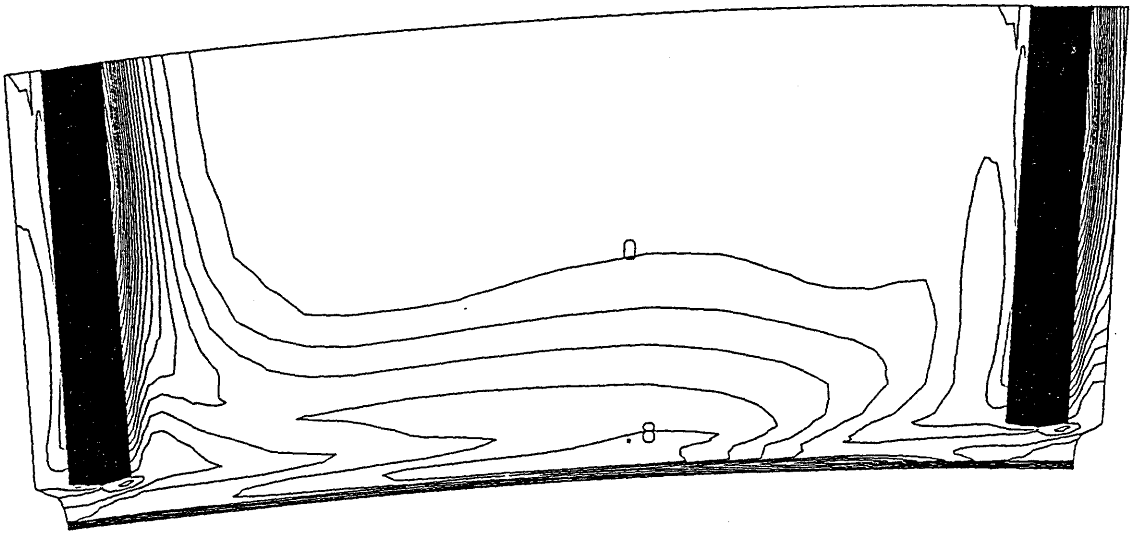

Smooth Hub

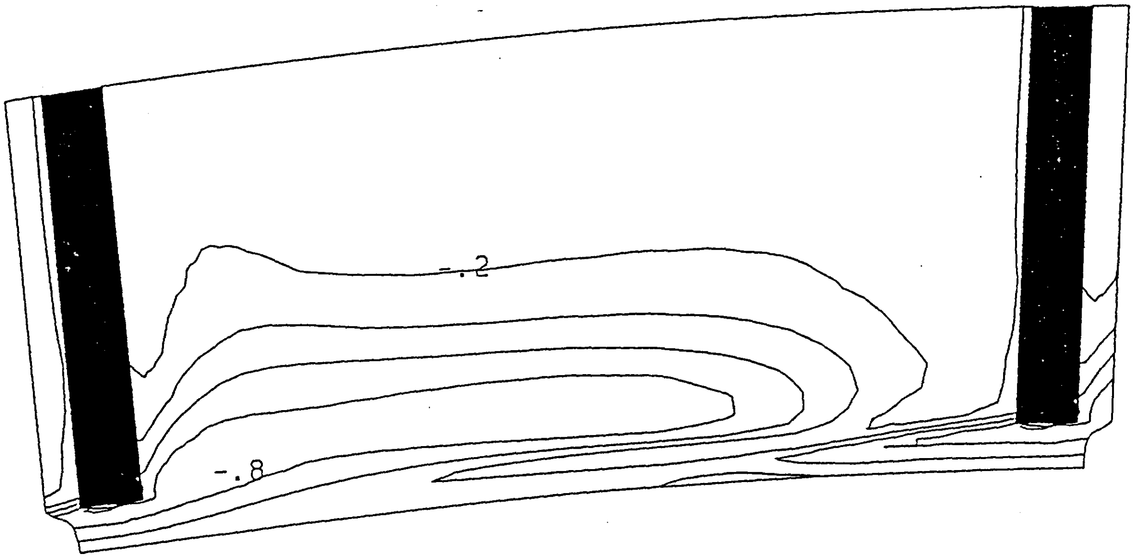

Figure 4.39 $(P_T-P_{Tin})/Q_{in}$ at 80% Chord

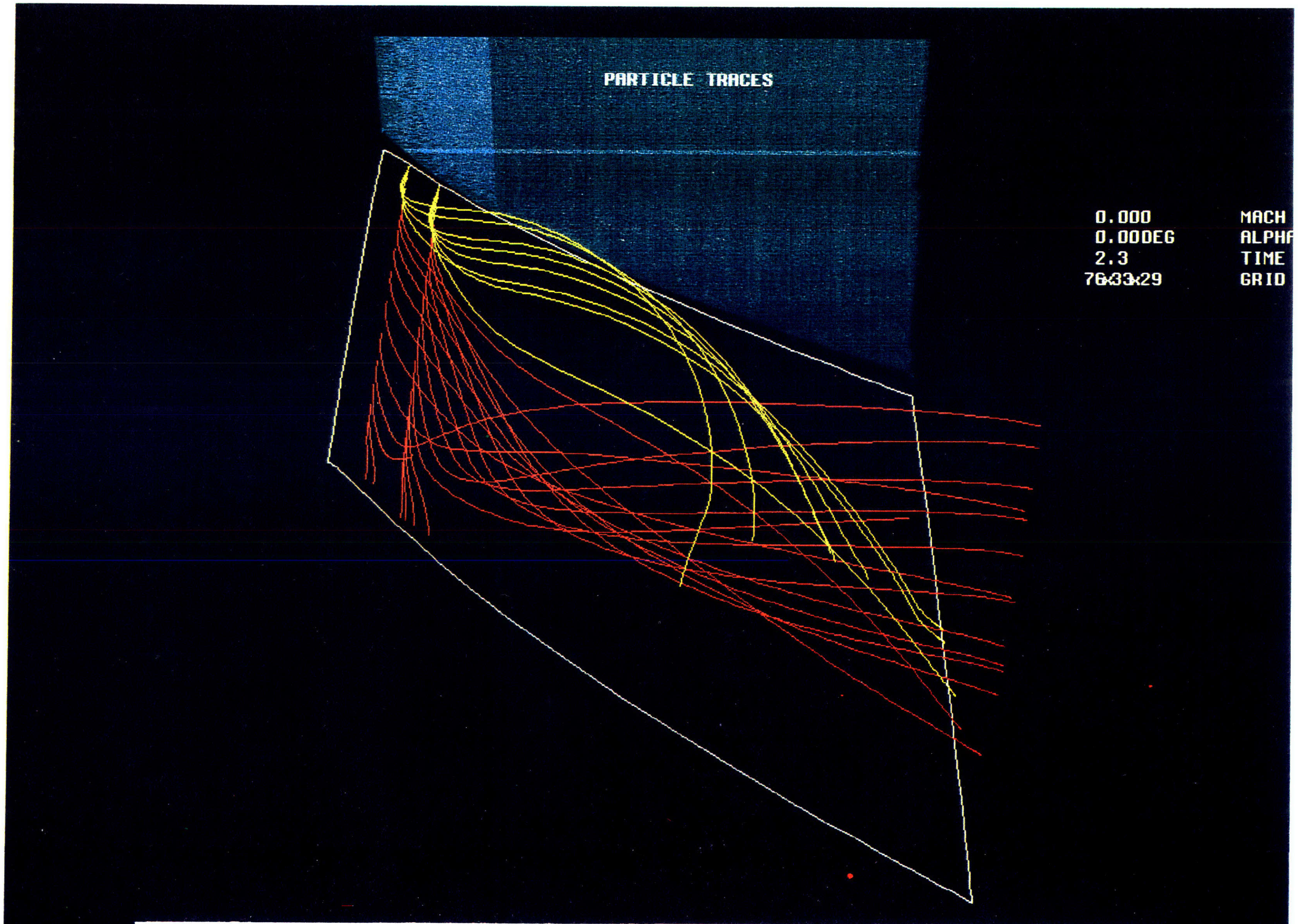

Figure 4.40 Particles Released from Hub Treatment Jet

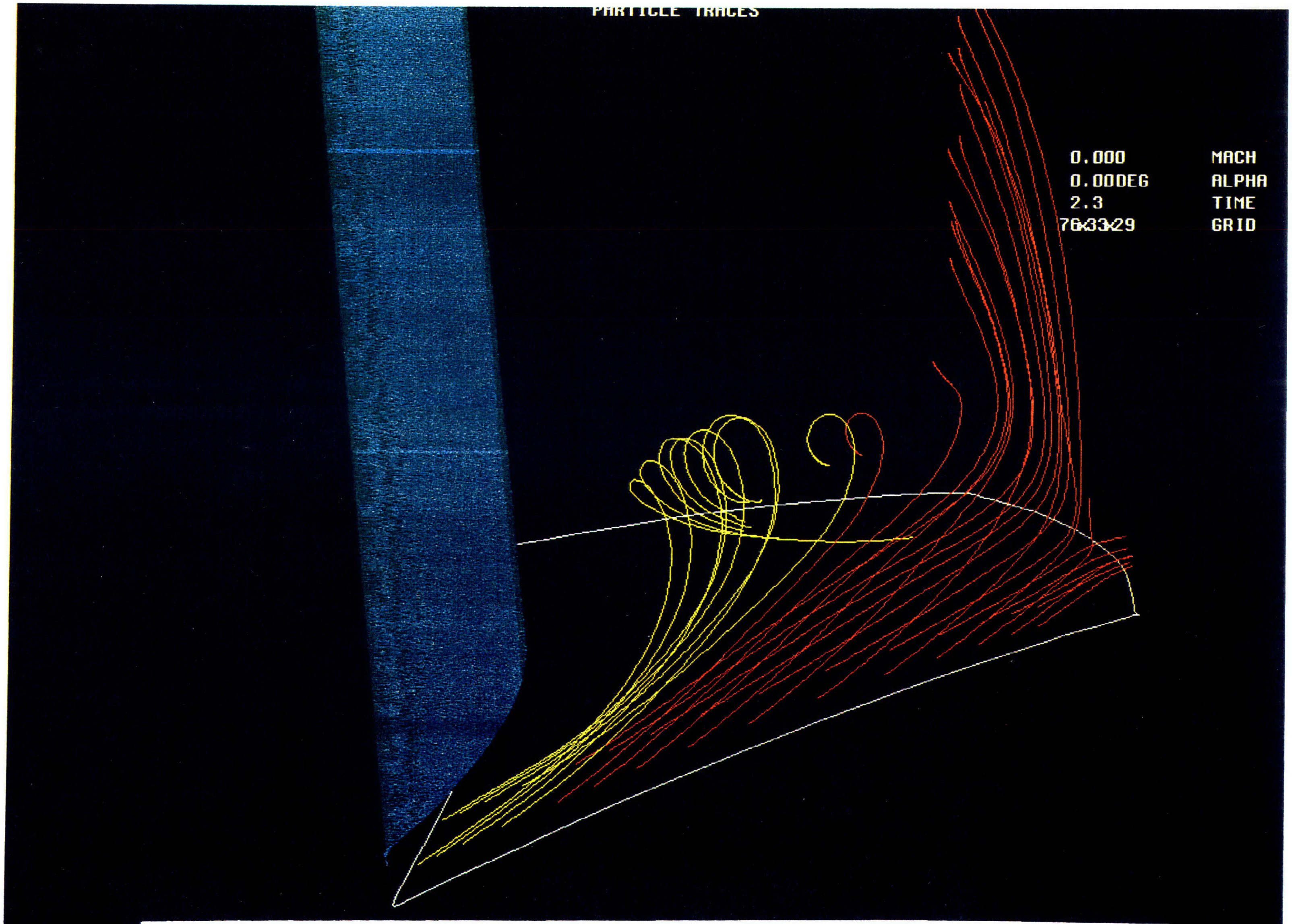

Figure 4.41 Particles Released from Hub Treatment Jet

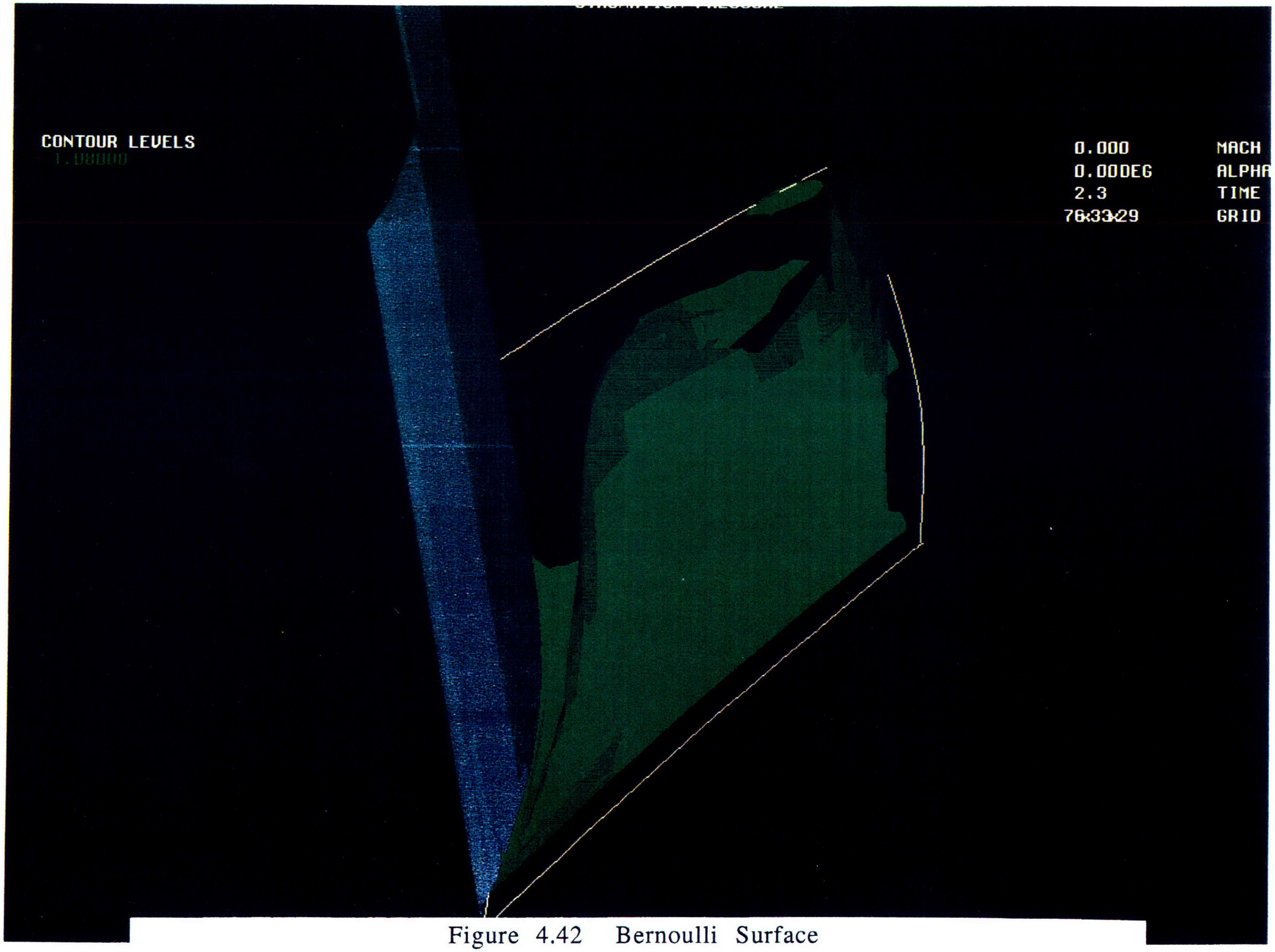

Figure 4.42 Bernoulli Surface

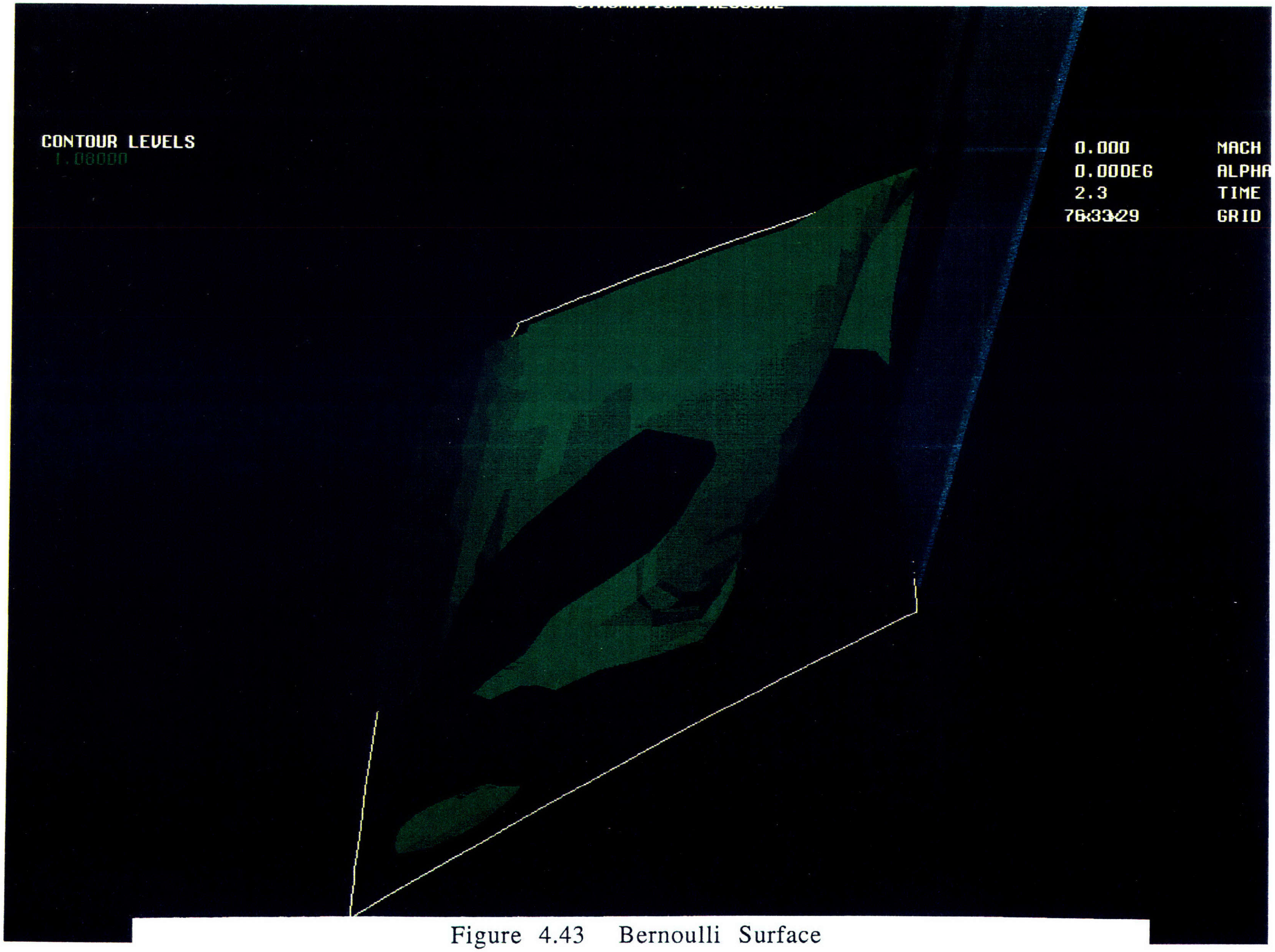

Figure 4.43 Bernoulli Surface

Appendix A
Effect of Tip Grid Shear and Artificial Dissipation on End Wall Total Pressure Loss

It was concluded from the study of the viscous flowfields that much of the low total pressure fluid near the endwall originated from the tip of the blades. This conclusion is understandable, considering the flow environment around the blade tip. The blade tip is a region where separated flow, high shear flow, and high vorticity production is occurring. All of these characteristics act to produce, or accentuate the production of total pressure loss.

While there is no shortage of physical causes for the loss production at the blade tip, there is concern about whether there is generation of loss due to numerical errors. From Figure 2.4 one can see that there is a great deal of grid shear underneath the tip of the blade. Moderate amounts of grid shear normally reduce the spatial accuracy in the region of the shear. For very high shear regions, truncation errors can become amplified, and completely spurious numerical errors can enter the solution. Therefore, in order to determine whether the loss fluid coming from the tip is heightened by numerical errors, two tests were conducted on the grid near the tip. These tests are outlined in the following sections.

Spatial resolution investigation

The first test of the grid was to determine how the spatial accuracy in the tip region effects the flow solution. If reduction of spatial accuracy from grid shear would produce numerical losses, then physically changing the spatial resolution under the blade tip should affect those numerical losses. To examine this, a grid was generated with much higher resolution in the tip region. Figure A.1 shows the original viscous solution grid and the high resolution tip grid. The lower 5% of the blade is shown on radial planes at midchord. The spatial accuracy near the blade tip for the high resolution grid is four times greater than that for the original grid.

To observe how the high tip resolution affects the flowfield, Figure A.2 is shown. The figure displays loss coefficient on axial planes at 50% chord for the two viscous solutions. The loss coefficient contours are very similar, and the magnitude of the loss seen in the core of the vortex is the same for the two cases. The loss levels at the blade tip are the same for the two solutions as well.

Figure A.3 shows total pressure loss coefficient for the two cases at the 64% chord location. Again the loss levels under the blade tip and in the vortex region are the same for the two solutions.

The conclusion drawn from the comparison of the two flowfields is that the spatial resolution has little effect on the loss production at the blade tip. Therefore, loss in spatial accuracy due to grid shear is not responsible for numerical entropy production.

Grid/blade surface orthogonality investigation

While it has been shown that a loss in spatial accuracy does not affect the tip loss generation, that is not the only possible source of numerical error due to grid shear. The effect of highly skewed cells on a three dimensional flowfield is not well understood, but a cell Jacobian near zero could produce nonphysical results regardless of the size of the cell. For this reason, a second test of the grid was devised. This test was to determine how orthogonality (or lack of it) in the grid near the tip affects the flowfield.

To examine this effect, a grid was generated in which the cells on and near the blade tip were much more orthogonal than the original case. Figure A.4 shows the grids near the blade tips for the two cases.

This investigation was carried out using inviscid flow solutions, because low total pressure fluid was found for the inviscid cases in the vortex core and near the blade tips. The total pressure losses found in the inviscid solution are numerical losses. The numerical losses can come from one of two sources. One is from spurious numerical errors and the other is from artificial dissipation. If the loss is due to grid shear, then the loss seen in the viscous solution could be due in part to spurious errors coming from a similarly sheared region. If the numerical loss seen in the inviscid solutions is due to artificial dissipation, it can be thought of as somewhat analogous to a physical effect, namely viscosity. While artificial dissipation is not a proper model for fluid viscosity, it can act in ways quite similar to physical viscosity.

Figure A.5 shows total pressure loss coefficient at midchord for the two inviscid cases. The magnitude of the loss in the vortex core in the orthogonal tip grid case is the same as that for the original inviscid case. The loss levels at the blade tip are similar as well.

The examination of the two flowfields yielded no significant differences in the amount or magnitude of loss fluid seen in the endwall region. Therefore, the conclusion drawn from the investigation is that the low total pressure fluid coming from the bottom of the blade is not caused by numerical errors associated with grid shear.

It has been determined that the loss seen in the inviscid solution is not generated by high grid shear. It is most likely generated by artificial viscosity. While this is again an accidental yet fortunate artifact of a numerical operator, the effect is not desired in the viscous calculation, where the physical effects of viscosity are explicitly modelled. However, this artificial effect is not a part of the viscous calculation. As stated in Chapter 2, the artificial dissipation operators are scaled by the meridional Mach number. By this scaling, the dissipation is reduced in viscous regions and is shut off close to solid surfaces. Since there is no artificial dissipation on the blade tip, it can not cause the loss production seen there.

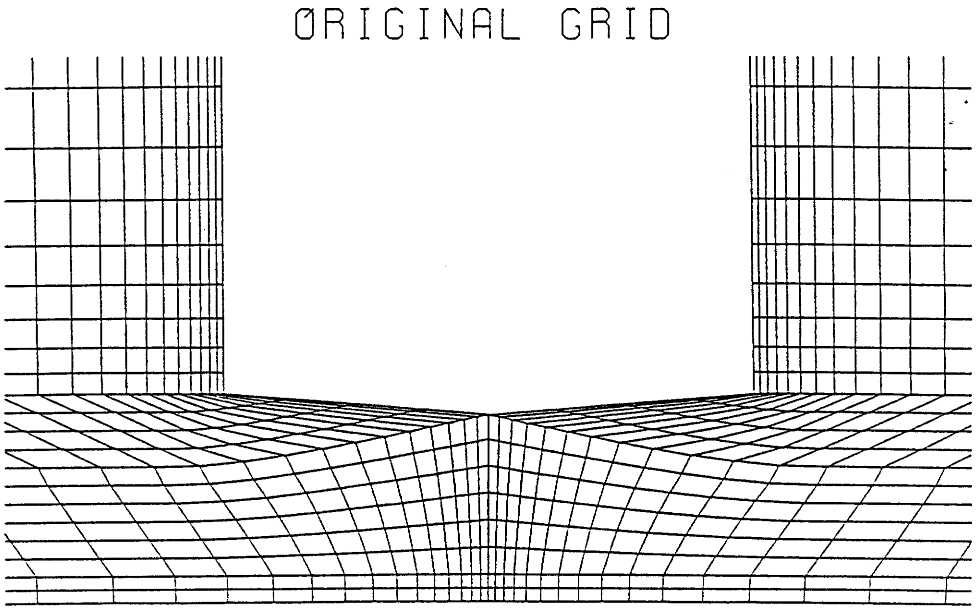

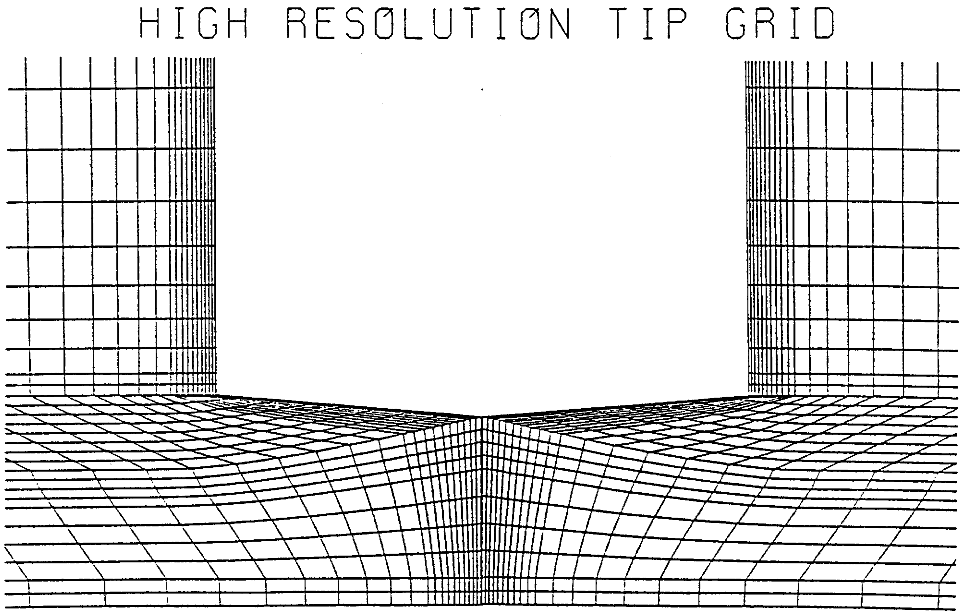

Figure A.1 Viscous Calculation Grids (r-θ Planes at 50% Chord)

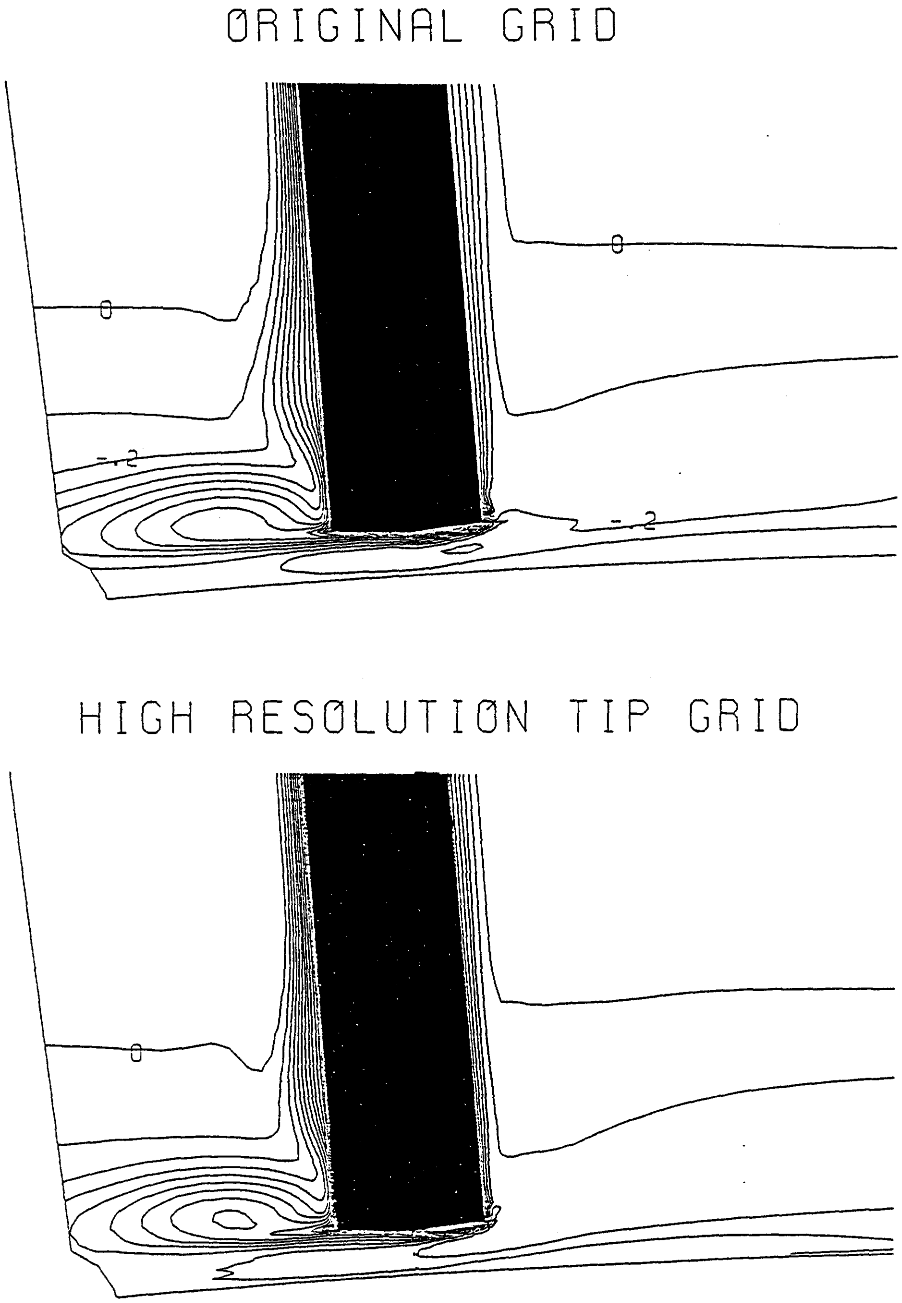

Figure A.2 Viscous Calculation: $(P_T - P_{Tin})/Q_{in}$ at 50% Chord

ORIGINAL GRID

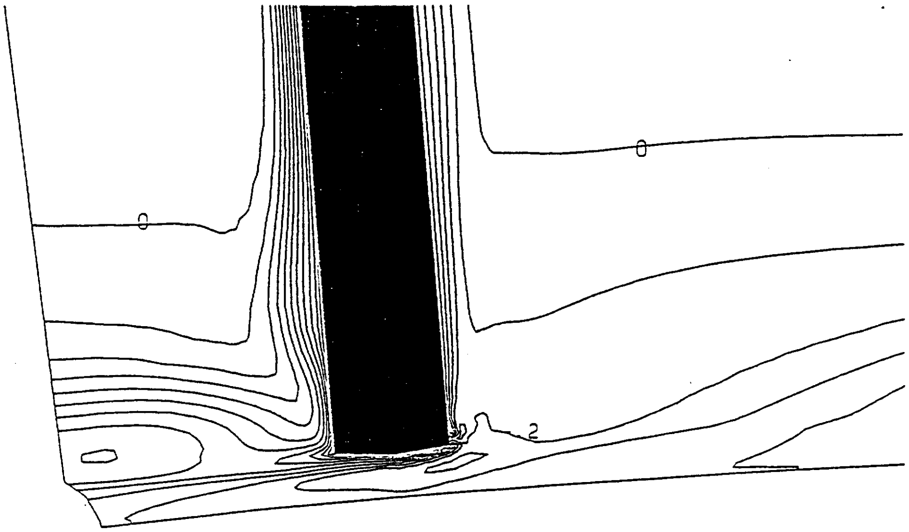

HIGH RESOLUTION TIP GRID

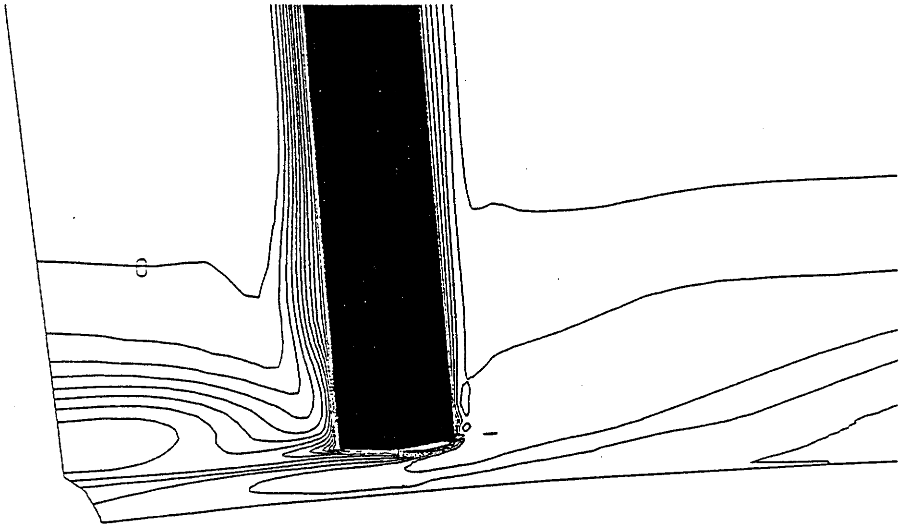

Figure A.3 Viscous Calculation: $(P_T-P_{Tin})/Q_{in}$ at 64% Chord

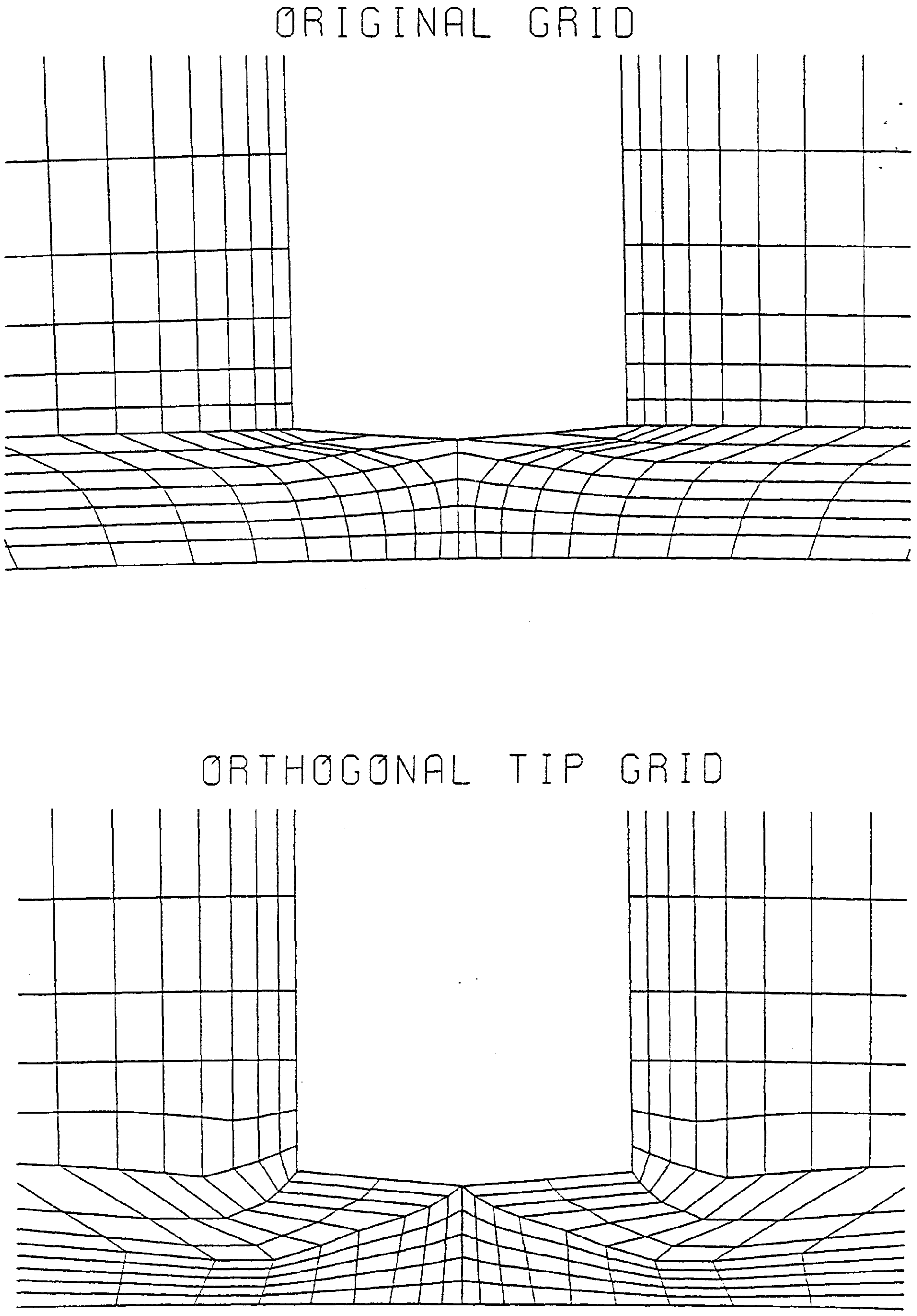

Figure A.4 Inviscid Calculation Grids (r-θ Planes at 50% Chord)

Figure A.5 Inviscid Calculation: $(P_T - P_{Tin})/Q_{in}$ at 50% Chord

Appendix B

Supplemental Equations to the Numerical Scheme

The terms in equations (3) are as follows:

$$L(U) = \int_A \left[\overline{F}\, dA_z + \overline{G}\, dA_r + \overline{H}\, dA_\theta\right] \tag{B.1}$$

$$\overline{F} = \begin{bmatrix} \rho u \\ \rho u^2 + p \\ \rho uv \\ r\rho uw \\ \rho uH \end{bmatrix} \quad \overline{G} = \begin{bmatrix} \rho v \\ \rho uv \\ \rho v^2 + p \\ r\rho vw \\ \rho vH \end{bmatrix} \quad \overline{H} = \begin{bmatrix} \rho w \\ \rho uw \\ \rho vw \\ r(\rho w^2 + p) \\ \rho wH \end{bmatrix} \tag{B.2}$$

The total enthalpy (H) is related to the total enternal energy (e) by:

$$H = e + \frac{p}{\rho} \tag{B.3}$$

The vicous operator L_V and its terms are as follows:

$$L_V(U) = \int_A \left[\overline{F_V}\, dA_z + \overline{G_V}\, dA_r + \overline{H_V}\, dA_\theta\right] \tag{B.4}$$

$$\overline{F_V} = \begin{bmatrix} 0 \\ \tau_{rr} \\ \tau_{zr} \\ \tau_{z\theta} \\ q_z \end{bmatrix} \quad \overline{G_V} = \begin{bmatrix} 0 \\ \tau_{zr} \\ \tau_{rr} \\ \tau_{r\theta} \\ q_r \end{bmatrix} \quad \overline{H_V} = \begin{bmatrix} 0 \\ \tau_{\theta z} \\ \tau_{\theta r} \\ \tau_{\theta\theta} \\ q_\theta \end{bmatrix} \tag{B.5}$$

$$\tau_{zz} = 2\mu \frac{\partial u}{\partial z} + \lambda_v \nabla.\vec{V} \qquad \text{(B.6)}$$

$$\tau_{zr} = \mu \left(\frac{1}{r} \frac{\partial u}{\partial r} + \frac{\partial v}{\partial z} \right) = \tau_{rz} \qquad \text{(B.7)}$$

$$\tau_{z\theta} = \mu \left(\frac{1}{r} \frac{\partial u}{\partial \theta} + \frac{\partial w}{\partial z} \right) = \tau_{\theta z} \qquad \text{(B.8)}$$

$$\tau_{rr} = 2\mu \frac{\partial v}{\partial r} + \lambda_v \nabla.\vec{V} \qquad \text{(B.9)}$$

$$\tau_{r\theta} = \mu \left(\frac{1}{r} \frac{\partial v}{\partial \theta} + \frac{\partial w}{\partial r} - \frac{w}{r} \right) = \tau_{\theta r} \qquad \text{(B.10)}$$

$$\tau_{\theta\theta} = 2\mu \frac{1}{r} \left(\frac{\partial w}{\partial \theta} + v \right) + \lambda_v \nabla.\vec{V} \qquad \text{(B.11)}$$

$$\lambda_v = -\frac{2}{3} \mu_l \qquad \text{(B.12)}$$